IMPACT OF INVERTER-BASED RESOURCES ON GRID DYNAMICS

A Dissertation
Submitted to the Graduate Faculty
of the
North Dakota State University
of Agriculture and Applied Science

By

Almir Ekic

In Partial Fulfillment of the Requirements
for the Degree of
DOCTOR OF PHILOSOPHY

Major Department:
Electrical and Computer Engineering

June 2022

Fargo, North Dakota

North Dakota State University
Graduate School

Title

Impact of Inverter-Based Resources on Grid Dynamics

By

Almir Ekic

The Supervisory Committee certifies that this ***disquisition*** complies with North Dakota State University's regulations and meets the accepted standards for the degree of

DOCTOR OF PHILOSOPHY

SUPERVISORY COMMITTEE:

Dr. Di Wu
Chair

Dr. Benjamin Braaten

Dr. Umamaheswara Rao Tida

Dr. Ying Huang

Approved:

July 6th, 2022 — Date

Dr. Benjamin Braaten — Department Chair

ABSTRACT

The increasing integration of renewable energy resources such as wind and solar into the electric power grid through power electronic inverters has changed grid dynamics and posed challenges to grid planning, operation, and protection. The growing penetration of renewable energy resources may drive the grid towards weak power grid conditions, under which grid stability issues may affect the operation of inverter-based renewable generators. To more accurately identify the weak grid conditions for guiding grid planning to prevent potential weak grid issues, a method for grid strength assessment is proposed by considering not only the impact the of interaction between interconnected renewable resources, but also the impact of the interactions between shunt capacitors interconnected through the power network. On this basis, we use a real-time digital simulator to explore inverter dynamics under different grid conditions including weak grid conditions. One of the major findings is that there are undesired transient events during the grid restoration process, and the undesired transient events become more significant when increasing the number of solar PV inverters or under weak grid operating conditions. This finding motivates us to study the impact of inverter dynamics on grid protection during the grid restoration period by using a real-time digital simulator. It is found that inverters can act as negative-sequence sources to inject negative-sequence currents into the grid during the grid restoration period and thus can adversely impact the performance of protection schemes based on negative sequence components and potentially cause relay maloperations during the grid restoration period, thus making system protection less secure and reliable.

ACKNOWLEDGMENTS

They do not tell you that this is the best part of writing a dissertation. It almost seems like a compilation of all the memories you have created during this adventure. I owe everything that I am now to my advisor, mentor, and friend Dr. Di Wu. Through the easy times and the tougher times, he has always been there with me with his priceless guidance. I came out of this an improved version of myself, and I must thank Dr. Wu for that.

Another special thank you to Manisha Maharjan for not only being one of the kindest people I have ever met, but also being one of the greatest teachers I have ever had. I am incredibly grateful I got to meet her, and if it wasn't for her depth of knowledge, I would not have learned as much as I did through this journey.

I also must include one of my best friends Henry Wolf. Whether it was late nights playing Destiny 2, or chit-chatting in his office, it was always a good time with him. I learned a lot about electromagnetics through him, which actually helped my research immensely.

To my committee, I appreciate every single one of them as well. I'd like to thank Dr. Braaten and Dr. Tida for constantly asking about my research. Every single time that happened, it pushed me to continue the research. I have worked with both of them at least in some capacity throughout my time at NDSU, and I would not trade the knowledge I have gained from them for anything in the world. I'd also like to thank Dr. Huang for helping me with my research as well, especially this last semester since she provided invaluable information on gas systems that I would have never found otherwise. Her kindness pushes me to become a better person, and her knowledge is unmatched.

For their technical expertise, I'd like to thank the RTDS support group (Sumek, Heather, and Udeesha), the SEL support group (John, Justin, Matt, and Mike), and the Department of Energy.

I express deep gratitude for my team at Ulteig for constantly pushing me to finish, as well as providing me with industry knowledge that directly affected my research. Outside of my team, I'd specifically like to thank Jacob Lien, Matthew Boese, Mari Beedle, Adam Diemert, Mark Scheid, the Transient Analysis Focus Group (Tracker Goree, Tahnee Miller, Stacey Page, Manisha Ghorai, Kurt Hall, Justin Marusak, and Brandon Goltz), and anyone else that I may have missed. One special shoutout goes to Ben Strombeck, for not only helping me gain the relay settings knowledge I have today, but also for being a great partner in crime. He without a doubt taught me vital information, while also being a great friend. I would not have finished if it weren't for him.

To my Bosnian boys (and honorary Bosnians, looking at you Chris and Daren), thanks guys. I don't think I can express enough gratitude for you all. The amount of fun I have every time I hang out with you guys is incredible, and I love each and every one of you. Throughout the years, we have roasted each other so many times, gotten into a lot of arguments, and just plain got angry sometimes. But we never split apart because we all love each other, and I couldn't have done this without your name calling and roasts. Pogini to you all.

And finally, to my family. It goes without saying that you played the most important part in me growing up. You pushed me so much to be the best version of myself inside and outside of school. I am forever in debt to you. My parents in particular never gave up on me, even when I was at my lowest. My mom for believing in me from the start to the end, for the days when I struggled, and for the days I was shining. My dad for being the man I want to become, for being so proud of me that he tells his coworkers and friends every day that I'm doing my PhD, and for

offering to help with some of the math even though he didn't know what a derivative was. My sister too, for making me feel like I'm on top of the world always. She let me rant about anything and everything to blow off some steam, and she was always interested in what I had to say. She will always be someone I look up to. My brother-in-law who welcomed me with open arms, and for being the most mature person I've ever known, something I still need to work on (impossible with Henry around). And to my nephew, whose smile makes all the struggles go away. His happiness and curiosity make me forget about life for a while, and I can't wait to see him grow up to be the most amazing person. Dajdza loves you so much.

DEDICATION

To my parents, my sister, and my wonderful nephew.

TABLE OF CONTENTS

LIST OF TABLES

LIST OF FIGURES

LIST OF APPENDIX TABLES

1. INTRODUCTION

Renewable energy resources are paving the way for the future of global infrastructures. With the source of energy being mainly to harness the wind and harness the sun, the earth provides us with these infinite resources to use to provide power to the ever-changing landscape since other sources of energy not only are in finite supply but pollute the environment as well. Photovoltaics in particular have been around for at least 70 years but did not start becoming prominent in a power grid until the 21st century [1]. Starting in 2021, solar energy has been cheaper than fossil fuels when it comes to providing power to the world, and thus making it one of the most prominent energy resources available today [2]. The problem with integrating a large amount of renewable energy sources into the power grid is that the grid becomes less stable, which causes problems with the operation of the power grid. This dissertation provides a complete definition on how operators can better define how unstable a grid is with the high penetration of renewable energy sources, as well as provide some insights into what issues arise when a large number of solar farms start to interact with the components in a power grid.

1.1. Background

1.1.1. Estimating Grid Strength Considering High Penetration of Renewable Energy Resources

In today's world where renewable energy is being penetrated into the grid in larger amounts than ever before, grid strength has been an ongoing research topic since the reduction of synchronous generators and the increase in inverter-based resources, like wind and solar, reduce the grid strength due to the grid having an overall low inertia. One of the major reasons for the research is to improve the grid strength assessment metrics to account for the change from a synchronous generator dominated grid to an inverter-based resource dominated grid [3].

Fundamentally, inverter-based resources are modeled differently than synchronous generators and thus a change in the calculation of grid strength is imperative. Namely, inverter-based resources are modeled as loads when incorporating them into the power grid [4].

Grid strength assessment involves reviewing the static voltage stability analysis to determine whether a grid is "strong" or "weak". A weaker grid will be more susceptible to collapse when a disturbance occurs somewhere in the network, so it can be classified as less stable. A stronger grid will be less susceptible to collapse when a disturbance occurs somewhere in the network, so it can be classified as more stable. Typically, grid strength assessment metrics involve using the voltage and its angle at a specific bus, along with other parameters such as impedance and power injected, to determine the strength at that point, which is the fundamental concept of static voltage stability analysis. AC power flow is most commonly used to perform the static voltage stability analysis. To perform it, the power injection or load demand at a bus is increased, and subsequently the power flow is iteratively solved at each increase to determine how much power that bus can handle and still be considered a "strong" point in the network [5]. The efficiency of this method is attractive for grid operators and planners since they are able to view how stable a bus in a power grid is by using only a few details of the power network at that bus.

In addition, when compared to synchronous generators, inverter-based resources separate the power sources from the grid, so when the grid becomes weak, the controls of the inverter will have a difficult time adjusting to the dynamics of the grid, which is challenging for grid planners. Knowing where potential weak grid issues exist can help engineers to try and mitigate them, and improving grid strength assessment metrics to account for renewable energy resources can assist in that.

1.1.2. Inverter Dynamics

In the power grid with high penetration of IB-RERs, the inverter plays an important role in interfacing the power grid and the renewable energy resource. Along with generating an AC supply for the grid, the inverter must ensure that the supply is synchronized with the grid in terms of frequency and voltage. To do this, each inverter has a set of controls that help to synchronize the voltage and current coming from the solar panels with the voltage and current coming from the power grid [6]. The controls are regulated by the North American Electric Reliability Corporation (NERC) to help standardize all inverters being used in North America [7]. The controls are often sophisticated enough to account for the varying energy that renewable energy resources provide, but the controls struggle to maintain a stable voltage reference when a disturbance happens, which is the fundamental concept of understanding inverter dynamics.

Overall, dynamic stability involves viewing not only the basics of a power grid shown in the static voltage stability analysis, but also the transients and dynamics within a network. Dynamic stability in a power system includes reviewing three-phase voltage and current waveforms following a larger disturbance, such as three-phase faults or a drop in the generator voltage [8]. In the context of inverter dynamic stability, it becomes more complicated due to the inverter controls struggling to adjust to the major disturbance.

In a renewable energy dominated grid, which inherently has low inertia due to the renewable energy resources having inverters instead of synchronous generators, dynamic stability revolves around reviewing the ability of the controls of the inverters to be able to handle the fault or voltage drop. The response of the controls of the inverter is different from the response of a synchronous generator when it comes to disturbances in the grid, which has caused grid planners problems in effectively designing their networks [9]. The difference revolves around the fact that

the controls of an inverter use information from the grid to be able to stabilize the renewable energy resource, since the resources the earth provides is variable, like wind and sunlight. Subsequently, when a disturbance happens in the grid, the controls not only have to stabilize the inverter and the renewable energy resource, but also have to handle the varying voltage and current from the disturbance in the grid since it uses that information.

Another important investigation specifically in inverter dynamics is voltage management and output fluctuations. The controls of the inverter use a reference voltage from the grid to be able to generate voltages at the output of the inverter, and with this comes variability in voltage. This directly leads into output fluctuations as well. To help with this, reactive power compensation devices are installed, usually capacitor banks, which stabilize the voltage and help with the output power fluctuations [10].

With these additional components needed for the stabilization of an inverter-based resource, they interact with the power grid in a way that causes both positive outcomes and negative outcomes to how the grid operates, and understanding these operations and interactions is crucial.

1.1.2.1. Protection Related to Inverter Dynamics

Inverter-based resources have been challenging relay protection schemes since their integration into the power grid began. Inherently, an inverter will provide a different faulted response than a synchronous generator due to the inverter acting as a current-controlled source instead of a conventional source. This has made relay protection in the vicinity of inverter-based resources challenging [11].

In particular, inverter-based resources differ in fault response by having an unusual negative sequence current and zero sequence current injection during a fault in response to a

voltage drop in the power grid. The injection is quite different than a synchronous generator, which naturally can provide a suitable amount of negative sequence current and zero sequence current, and this causes the relay protection design to be much more challenging in inverter-based resources [12].

To provide some background, relay protection schemes use information gathered by the relay to perform protection functions. Some of the information required include three-phase voltages and currents, negative sequence currents and voltages, zero sequence currents and voltages, angular relationships between different buses, and so on [13]. These are all available in a synchronous generator dominated network but are difficult to come by in an inverter-based resource dominated network.

Relay protection schemes become even more complicated in an inverter-based resource dominated grid when we consider the response of the inverter-based resources after a fault has been cleared. This phase of a power system is commonly referred to as the "grid restoration period". With the controls of the inverter struggling to maintain a stable voltage reference during a large disturbance such as a fault, a similar conclusion can be made that when the power grid clears the fault and the voltages and currents begin to adjust back to nominal operation, the controls will have to similarly adjust, which could cause relay protection schemes to malfunction.

1.2. Contributions of this Dissertation

The main contributions of this dissertation are summarized as follows.

1. A more accurate grid strength assessment metric is proposed. The effective site-dependent short-circuit ratio (ESDSCR) not only includes the interactions between different IBRs, but also between different shunt capacitor banks present in the power system network. Present short-circuit ratio metrics typically will overestimate grid strength since they do not include

the interactions described above. With the ESDSCR, not only does it include the above interactions, but it also is the general form of the ESCR, which is commonly used in the industry. If there is only one inverter-based resource and one shunt capacitor bank, the ESDSCR is equal to the ESCR for assessing grid strength.

2. It can be shown that momentary cessation, which is the response of a solar inverter to a large disturbance, can negatively affect the dynamics in a solar PV grid-connected system by inducing overvoltages and overcurrents in a network. In addition, with the detailed switching model being used in the simulation testbench, various other factors that interact with the momentary cessation function in inverters are also explored such as increasing the number of solar inverters in the system and decreasing grid strength, which both affect the dynamics of the grid negatively. A solution is presented where the inverter controls design engineers can vary the re-injection time of the inverters so that each inverter re-injects current at a different time to help offset the overvoltages and overcurrents in the system.
3. Investigate the negative-sequence current characteristics of solar inverters during the grid restoration period and analyze their negative impact on the performance of typical protection schemes using a hardware-in-loop simulation based on the RTDS. It was shown that high negative-sequence currents are observed during the grid restoration period following the clearing of a fault, which tripped the relays connected in the network indicating that overcurrent elements in relays will not operate correctly. It was also shown that directional elements in relays will not operate correctly due to the negative-sequence current and voltage magnitudes and angles.

1.3. Organization of this Dissertation

The rest of this dissertation is organized into three main chapters, followed by a conclusion chapter. The contents of the chapters as well as the titles will be described as follows.

Chapter 2 describes the testbench being used throughout the dissertation. This chapter also verifies that the equipment and the software are working properly by testing the relay equipment, RTDS machine, and the RSCAD software.

Chapter 3 briefly explores the derivation of the effective short-circuit ratio, since the derivation is non-existent in the literature, as it relates to static voltage stability. The derivation is then expanded to include multiple reactive compensation devices instead of one, which then produces the proposed effective site-dependent short-circuit ratio (ESDSCR). The ESDSCR is then employed in the IEEE 39-bus test system to capture its capabilities.

Chapter 4 creates a model using a real-time simulation test bench with the RTDS to investigate the impact of momentary cessation on sub-cycle dynamics in solar PV grid-connected systems. Different scenarios will be presented, such as increasing the number of solar inverters as well as the impact of grid strength, which was defined in the last chapter. A solution will also be presented that can potentially solve the issues demonstrated above.

Chapter 5 further expands the previous chapter by creating a more detailed transmission network to study the effects of momentary cessation on transmission line relay protection schemes, specifically looking at the negative sequence current injection following the clearing of a fault during the grid restoration period. The relay protection schemes will include looking at the negative-sequence overcurrent element, which compares the negative-sequence current present at the relay with the threshold set in the relay, and the negative-sequence directional element, which compares the angular difference between the negative-sequence current and voltage.

Chapter 6 summarizes the entire dissertation and provides insights as to where this research could go following the findings presented.

2. RTDS TESTBENCH BUILDOUT AND VERIFICATION

Here, the real-time simulation testbench will be explained in detail, which is used for the simulation part of the dissertation. Verification of the testbench will also be performed.

2.1. RTDS-based Testbench Buildout

The hardware-in-loop simulation platform is illustrated in Fig. 1, where the RTDS is linked to a physical relay from the Schweitzer Engineering Laboratories (SEL). The relay can use built-in metering functions to analyze event reports for rapid commissioning, testing, and post-fault diagnostics. The simulation model of a solar PV power system is created on a guest computer using the RSCAD software. Then, this software compiles and loads this model into the RTDS for real-time simulations. The digital output signals of the current and voltage simulated by the RTDS are converted into analog signals by the Giga-Transceiver Analog Output (GTAO) card and are then fed into the relay. The relay has a low-level interface, which allows them to directly receive the converted analog signals without the need for the voltage/current amplifier. The dry contacts of the relay are connected to the low-voltage panel of the RTDS to send the digital tripping signals from the relays to the RTDS via the input channels on its front lower voltage panel. As soon as the relay trips, it is detected by the digital input of the RTDS, which opens the breaker in the model being simulated in real time and sends the updated signals to the RTDS for real-time simulation. The updated simulation results can be monitored by RSCAD software.

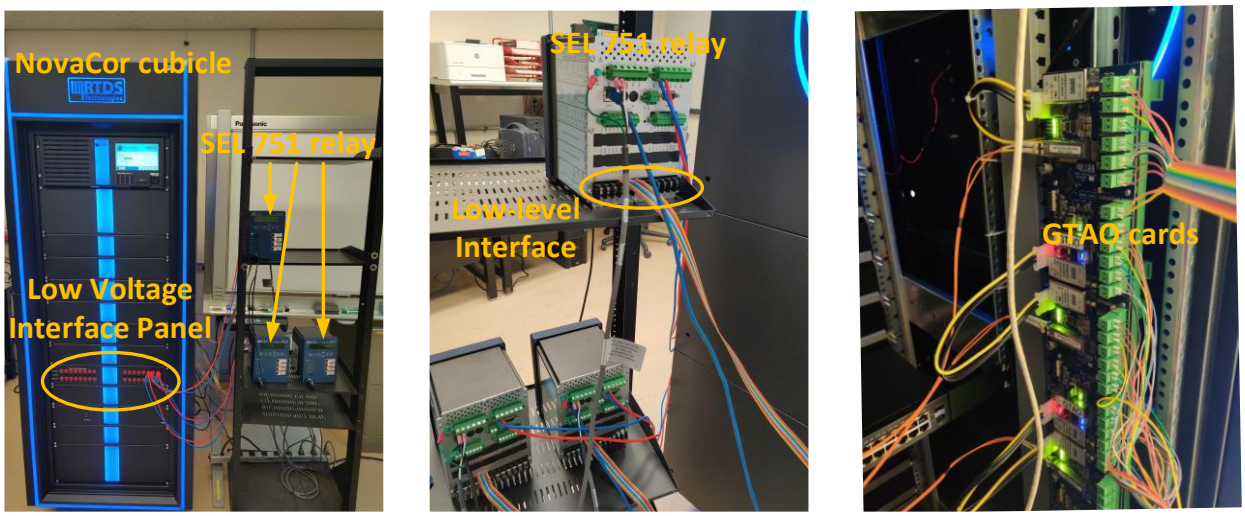

Figure 1. The developed physical protection system linked to the RTDS: the interface between the relays and the low-voltage panel of the RTDS; the back of the relays; and the interface between the relays and GTAO card in the RTDS

2.2. Verification of the RTDS-based Testbench

To verify the function of the protection relay system, the system is tested using the simulated power systems on the RTDS. Individual relays are tested on a simulated power system under various fault scenarios.

2.2.1. Description of the Individual Relay Verification Simulation

Before the testing of the protection relay system, the individual relays have been tested on a 3-bus power system simulated on the RTDS under various fault scenarios. As shown in Fig. 2, the simulated power system includes the following elements, which are modeled by the RSCAD software: a 34.5kV AC source, a distribution line, a 50MW load, a circuit breaker, a current transformer, and a potential transformer. In the system, the distribution line connects the source and load. The distribution line has a breaker CB1 controlled by the physical SEL 751 relay. The CT and PT are modeled by the RSCAD software in detail to reflect real system characteristics.

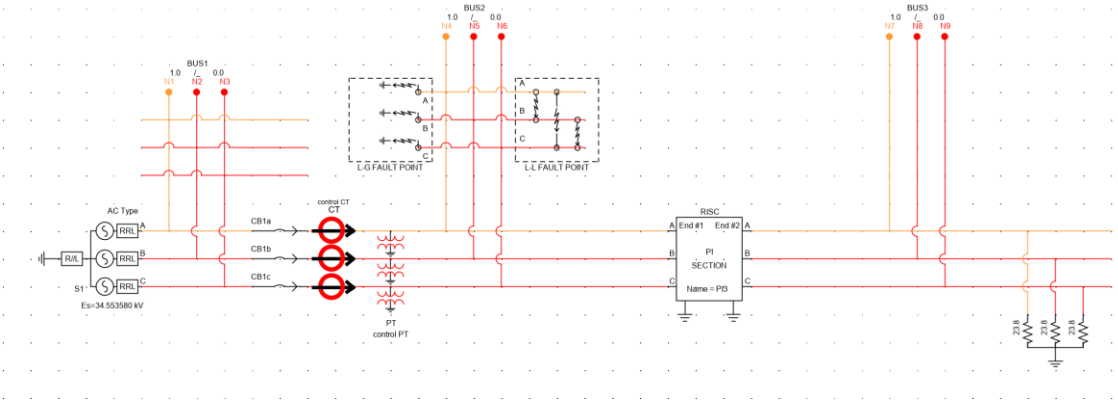

Figure 2. 3-bus power system simulated on the RTDS.

The SEL 751 is a feeder protection relay, which can provide standard feeder protection features, including phase, negative-sequence, residual, and neutral overcurrent elements and other protection schemes. Each element type has different levels of instantaneous protection. The relays can use built-in metering functions to analyze event reports for rapid commissioning, testing, and post-fault diagnostics. The setting for the SEL-751 relay can be set based on power system characteristics using the ACSELERATOR software as shown in Fig. 3.

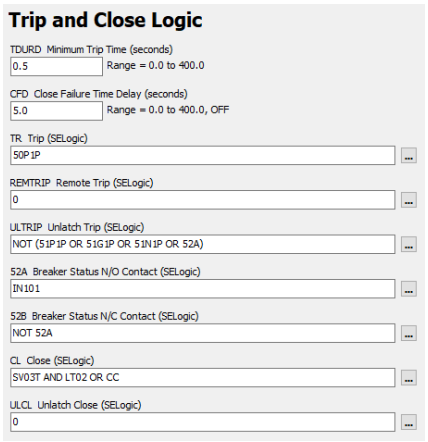

Figure 3. ACSELERATOR settings for the SEL-751 relay.

The relay senses the voltages and currents from the RTDS system, and in case of any fault, it sends out the trip and reclose signals to the simulated circuit breakers in the power system. Specifically, Fig. 4 shows the setting for the GTAO card in the RSCAD software to convert the

simulated voltage and current signals into analog signals, which are connected to the SEL 751 relay's low-level interface. Trip signals from the relay are interfaced to the RTDS via digital input ports. Fig. 5 shows how the digital input signals are interfaced in the simulation.

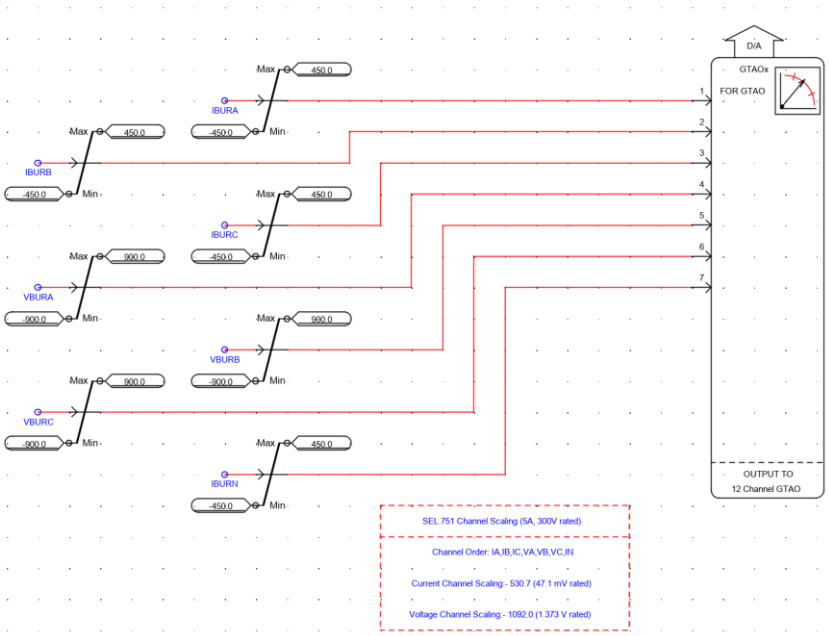

Figure 4. Analog output from the simulated power system to the SEL-751 relay.

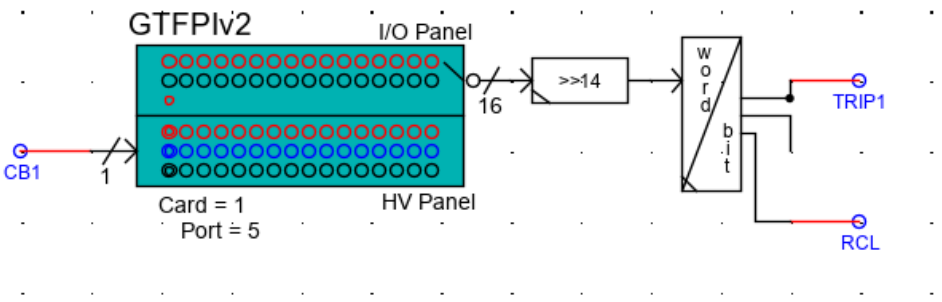

Figure 5. Digital signal from the SEL-751 relay to the simulated power system.

Fig. 6 shows the control logic in the RSCAD software to operate the simulated breaker based on the signals from the physical SEL 751 relay. Fig. 7 shows fault control logic to simulate

the different types of faults. For a fault, the breaker should open once the fault occurs automatically for each phase.

The fault control logic is built in the RSCAD software. The fault logic is built to create different types of faults on the distribution line. The fault logic consists of two parts. The first part of the fault control logic is used to control the point on the wave called as fault inception point. The fault button when pressed produces a 20-millisecond pulse, which is longer than the one cycle at 60 Hz. A pulse is produced by the AND gate and then combined with the zero crossing and the fault button. The pulse derives the point on wave logic, which is comprised of a silder, a gain block, and a pluse duration timer to detect the rising edge. The second part of the control logic circuit is used to control the fault type and location. Fault switches for the phase to group fault types are combined to create the necessary value. This value is multiplied by the pulse from the first part of the logic, thereby creating a pulse width with an integer value that can control the fault branches.

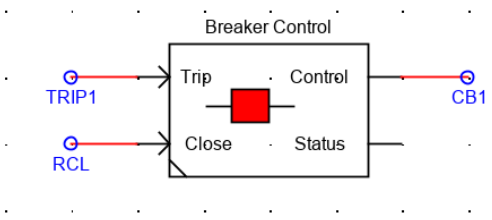

Figure 6. Breaker control logic.

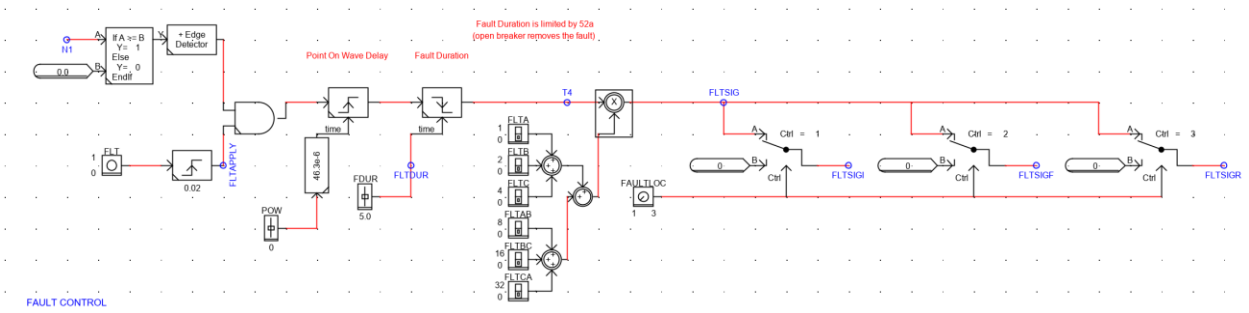

Figure 7. Fault control logic for the simulated 3-bus power system.

2.2.1.1. Testing Results of the Individual Relay Verification Simulation

Single phase line to ground, two-phase line to ground, and three-phase fault are simulated on the line in the 3-bus power system as shown in Fig. 2. Each individual SEL 751 relay has been tested on the system. Fig. 8-Fig. 18 demonstrate the testing results for a single SEL 751 relay in the system under three types of faults. Fig. 8 and Fig. 9 shows the voltage and current waveforms as well as simulated fault and trip signals without any fault. Fig. 10 and Fig. 11 shows the voltage and current waveforms as well as simulated fault and trip signals for a single-phase fault on 'phase A.' Fig. 12 shows the voltage and current waveforms recorded by the relay for the same single-phase fault. Fig. 13 and Fig. 14 show the voltage and current waveforms as well as simulated fault and trip signals for a two-phase line to ground fault on 'phase A' and 'phase B.' Fig. 15 shows the voltage and current waveforms recorded by the relay for the same two-phase line to ground. Fig. 16 and Fig. 17 show the voltage and current waveforms as well as simulated fault and trip signals for a three-phase fault. Fig. 18 shows the voltage and current waveforms recorded by the relay for the same three-phase fault.

The current flowing into the circuit breaker 1 which is sensed by SEL 751 relay is 998 Amps for considered test case and the CT ratio of a current transformer is 100. So the current flowing out of the current transformer is 9.98 A (998/100). This RMS current of 9.98 Amps can

be viewed and verified in the plot of currents coming out of the current transformer i.e., IburA, IburB, and IburC.

For the 3-bus power system, the nominal RMS voltage and RMS current during the normal operation of the system is 27.35 kV and 12.54 Amps in CT1. Now, if the fault is applied say single line to ground fault at the generator, then the voltages in the distribution line shoot up to 32 kV approximately and current shoot up to 123.38 A in CT. Now, in the SEL 751 settings we specified that the current across the breaker should not be greater than 1.5 times of the nominal current. So the threshold current at which the breakers stay closed is 1.5*12.54 = 18.81 Amps or RMS current (burden current Ibur) coming out of the CT should not be more than 18.81 Amps.

The results in Fig. 10-Fig. 12 verify the proper function of the tested relay for a single-phase fault. Before the fault, Fig. 10 shows that there are no faulted voltages and overcurrent, and Fig. 11 shows that fault and trip signals are low, which mean no fault and no trip at this time. When the single-phase fault is initiated on phase A, Fig. 10 shows that the current on 'phase A' (and the voltage on phase B and phase C) becomes high and then becomes zero when the relay operates and the breaker opens. In this case, Fig. 11 shows that the values of the fault and trip signals are high (shaded box). The breaker would open about 1.7 cycles after the fault. As shown in Fig. 10 and Fig. 12, the faulted voltage and current waveforms simulated by the RTDS are consistent with those recorded by the relay, which verifies the proper function of the SEL-relay integrated in the 3-bus test power system.

The results in Fig. 13-Fig. 15 verify the proper function of the tested relay for a two-phase line to ground fault on 'phase A' and 'phase B.' It can be seen from Fig. 13 that when the two-phase line to ground fault is initiated, the currents on 'phase A' and 'phase B' (the voltage on 'phase' C) become high and then becomes zero when the relay signal opens the breaker. In this

case, Fig. 14 shows that the values of the fault and trip signals are high (shaded box). The breaker would open about 1.7 cycles after the fault. As shown in Fig. 13 and Fig. 15, the voltage and current waveforms simulated by the RTDS match with those recorded by the relay, which verifies the proper performance of the SEL-relay integrated in the 3-bus test power system.

The results in Fig. 16-Fig. 18 verify the proper function of the tested relay for a three-phase fault on ‘phase A’ and ‘phase B.’ It can be seen from Fig. 16 that when the three-phase fault is initiated, the currents become high and then becomes zero when the relay signal opens the breaker. In this case, Fig. 17 shows that the values of the fault and trip signals are high (shaded box). The breaker would open about 1.7 cycles after the fault. As shown in Fig. 16 and Fig. 18, the voltage and current waveforms simulated by the RTDS match with those recorded by the relay, which verifies the proper performance of the SEL-relay integrated in the 3-bus test power system.

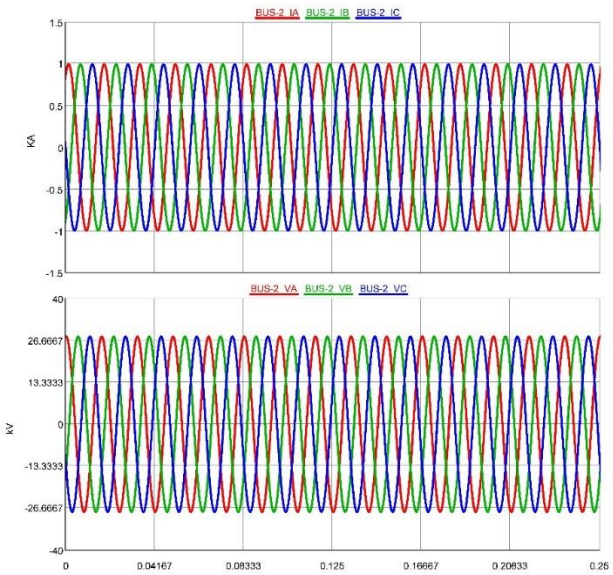

Figure 8. Voltage and current waveforms without any fault in the 3-bus power system.

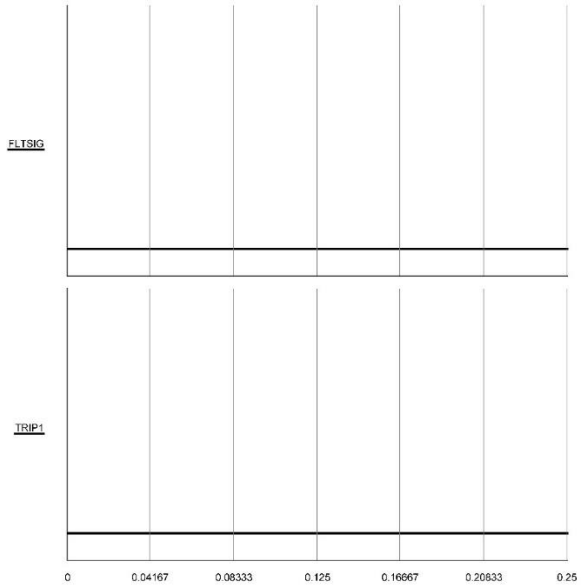

Figure 9. Simulated fault and trip signals without any fault in the 3-bus power system.

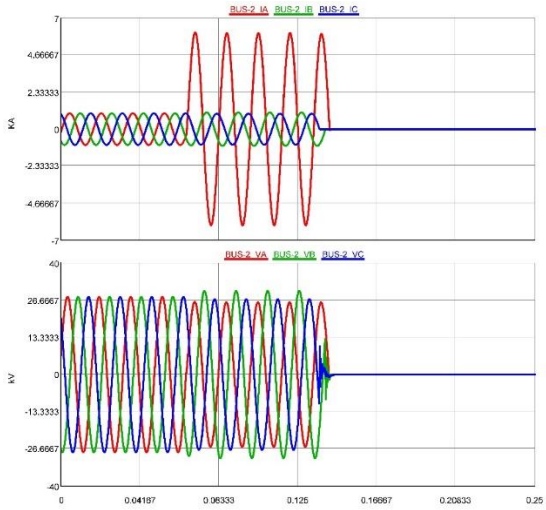

Figure 10. Voltage and current waveforms with a single line-to-ground fault in the 3-bus power system.

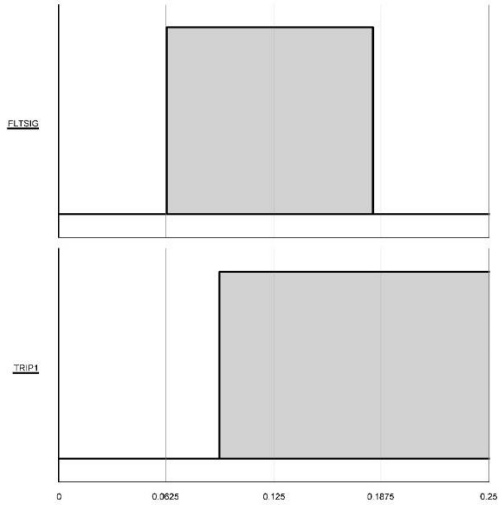

Figure 11. Simulated fault and trip signals with a single line-to-ground fault in the 3-bus power system.

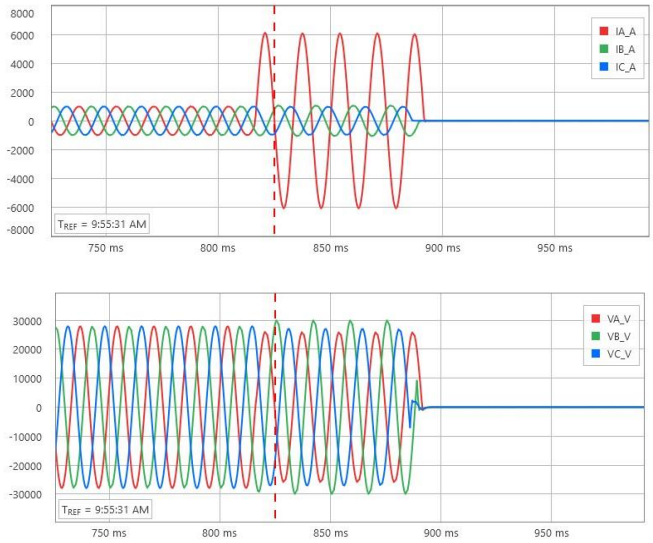

Figure 12. Voltage and current waveforms with a single line-to-ground fault in the 3-bus power system recorded by the relay.

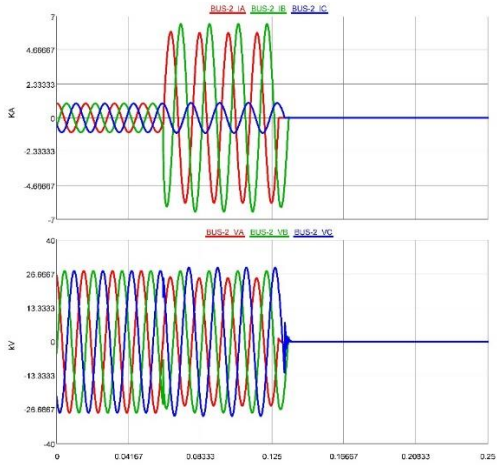

Figure 13. Voltage and current waveforms with a double line-to-ground fault in the 3-bus power system.

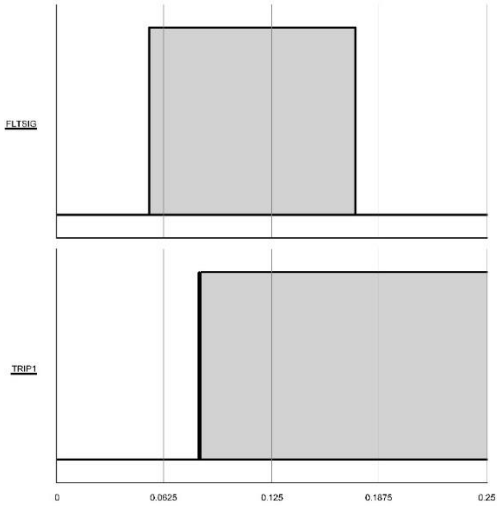

Figure 14. Simulated fault and trip signals with a double line-to-ground fault in the 3-bus power system.

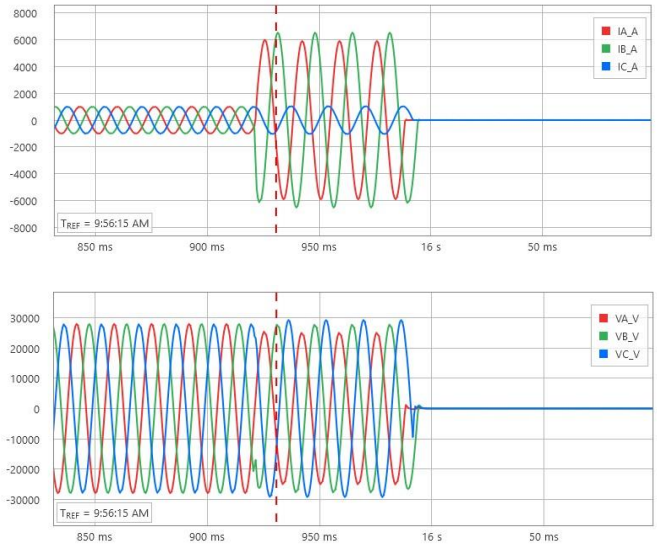

Figure 15. Voltage and current waveforms with a double line-to-ground fault in the 3-bus power system recorded by the relay.

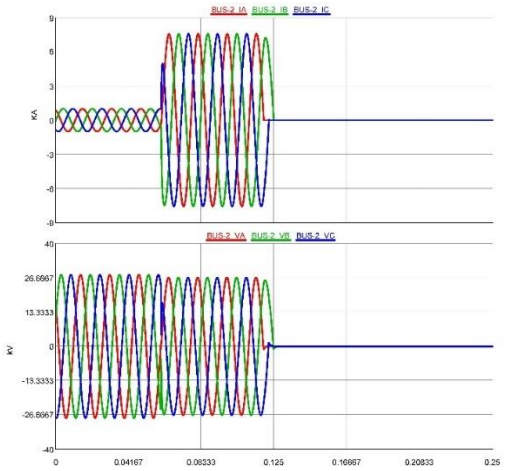

Figure 16. Voltage and current waveforms with a three phase fault in the 3-bus power system.

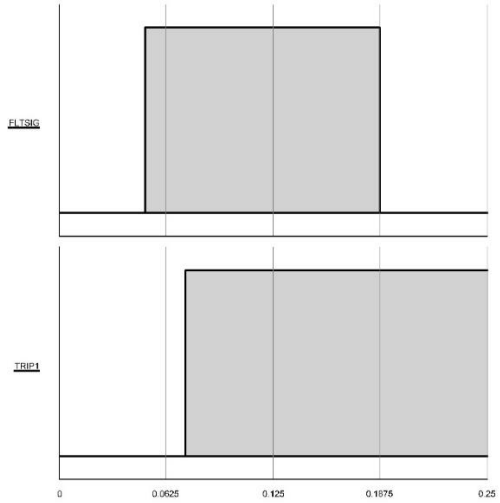

Figure 17. Simulated fault and trip signals with a three-phase fault in the 3-bus power system.

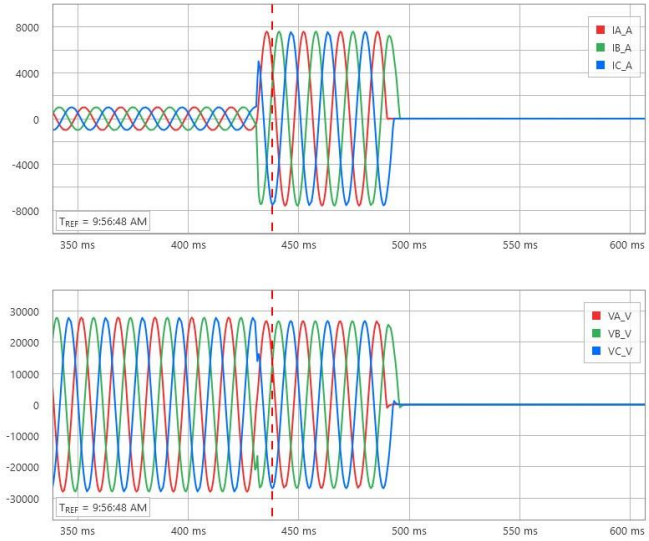

Figure 18. Voltage and current waveforms with a three-phase fault in the 3-bus power system recorded by the relay.

2.2.2. Description of the Full Relay Protection Scheme Verification Simulation

The protection relay system consisting of three SEL 751 relays linked to the RTDS have been tested on a 7-bus power system simulated on the RTDS under various fault scenarios. As shown in Fig. 19, the simulated power system includes the following elements, which are modeled by the RSCAD software: a 34.5kV AC source, a distribution line, two feeder lines connecting to

two 50 MW loads, three circuit breakers, CTs, and PTs. In the test system, the distribution lines connect the source and two loads. The breakers CB1, CB2, and CB3 controlled by the physical SEL 751 relays. The CTs and PTs are modeled by the RSCAD software in detail to reflect real system characteristics.

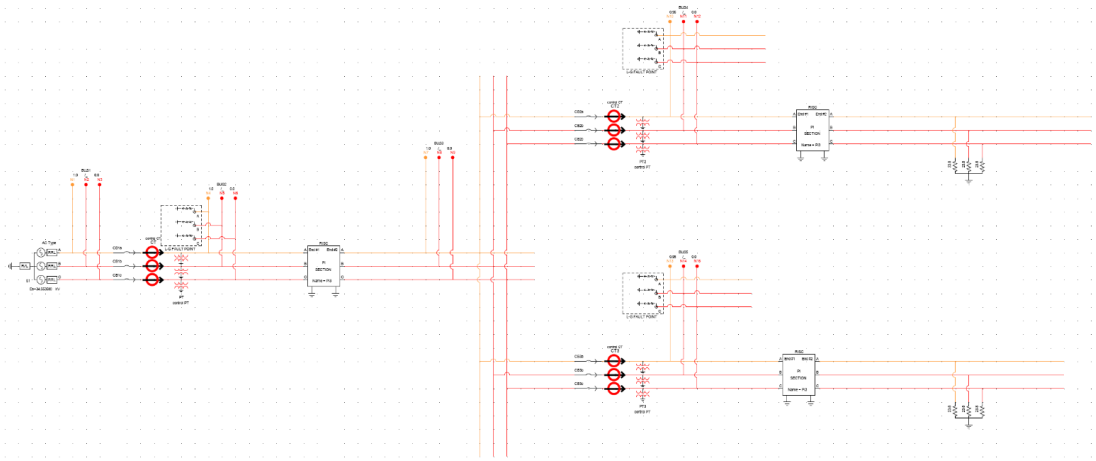

Figure 19. 7-bus power system as simulated on the RTDS in RSCAD.

As illustrated in Fig. 1, each tested relay senses the voltages and currents from the RTDS system, and in case of any fault, it sends out the trip and reclose signals to the simulated circuit breakers in the power system. Specifically, Fig. 20 shows the setting for the GTAO cards to convert the simulated voltage and current signals into analog signals, which are connected to the relay's low-level interface. Trip signals from the relay are interfaced to the RTDS via digital input ports. Fig. 21 shows how the digital input signals are interfaced in the simulation.

Fig. 22 shows the control logic to operate the simulated breaker based on the signals from the physical relay. Fig. 23 shows fault control logic to simulate the different types of faults. For a single-phase line to ground fault, the breaker should open once the fault occurs automatically for each phase. In the case of a two-phase line to ground fault, all 3 phases of the breaker should open. Fig. 24 shows the relay settings used for relays 2 and 3 in the system. Relay 2 and relay 3 utilized

the time-overcurrent trip element, while relay 1 utilized the instantaneous overcurrent trip element. For the time-overcurrent trip element, a short-time inverse TCC was selected since it best represented the trip characteristics desired for the system, according to the fault analysis. Fig. 25 shows the TCC.

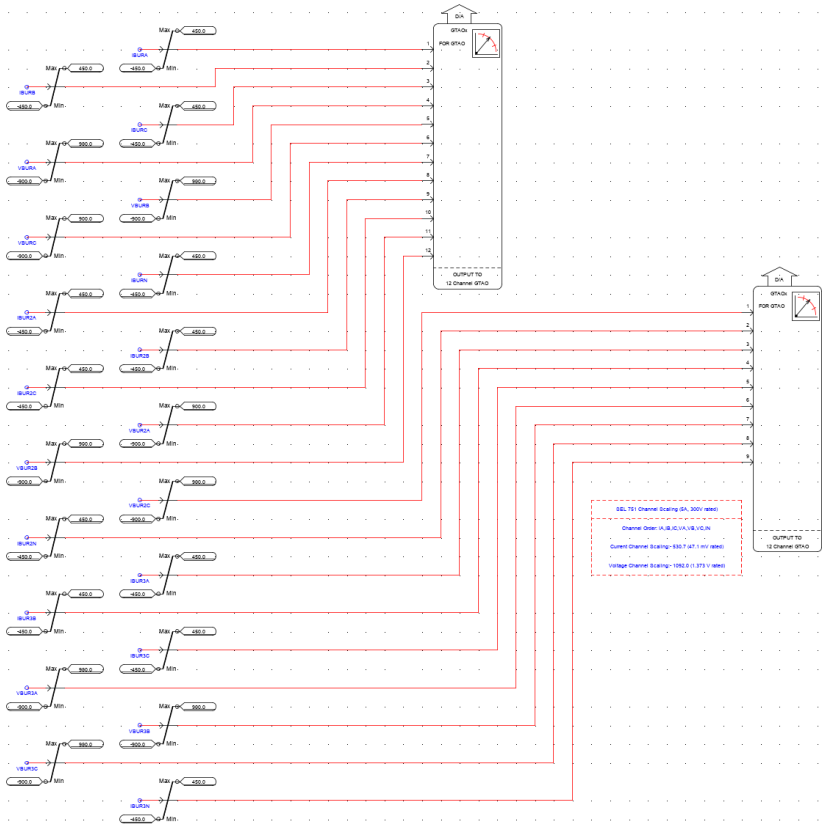

Figure 20. Analog output from the 7-bus power system to the relays.

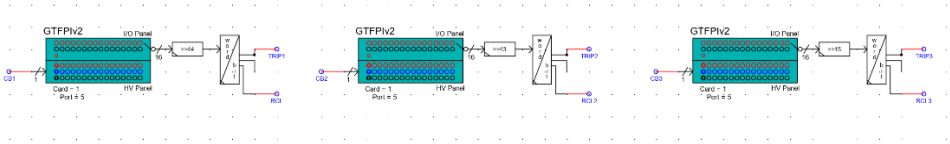

Figure 21. Digital signal from the relays to the 7-bus power system.

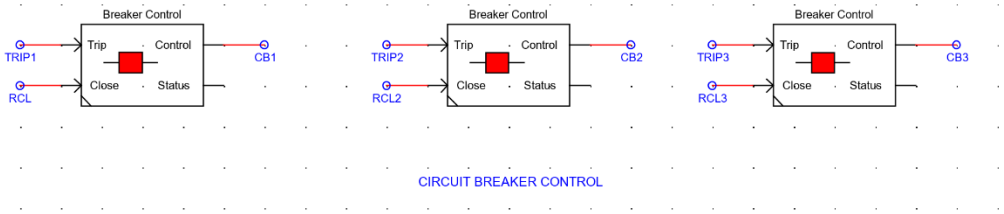

Figure 22. Breaker control logic.

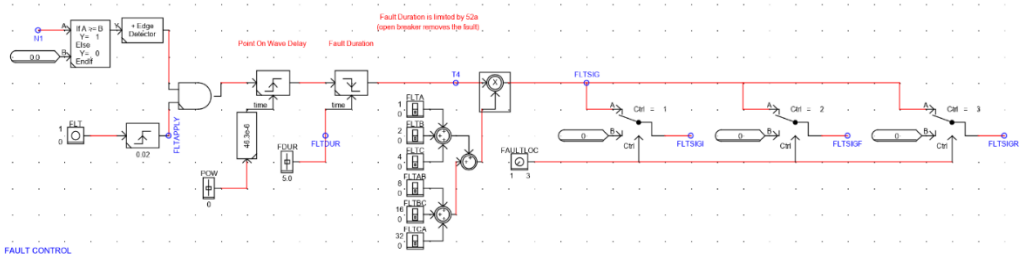

Figure 23. Fault control logic for 7-bus power system.

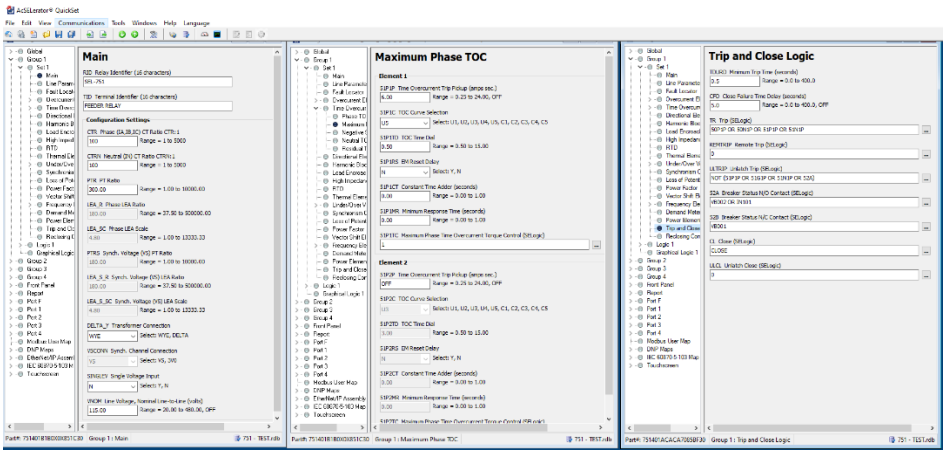

Figure 24. Relay settings for relays 2 and 3 for 7-bus power system.

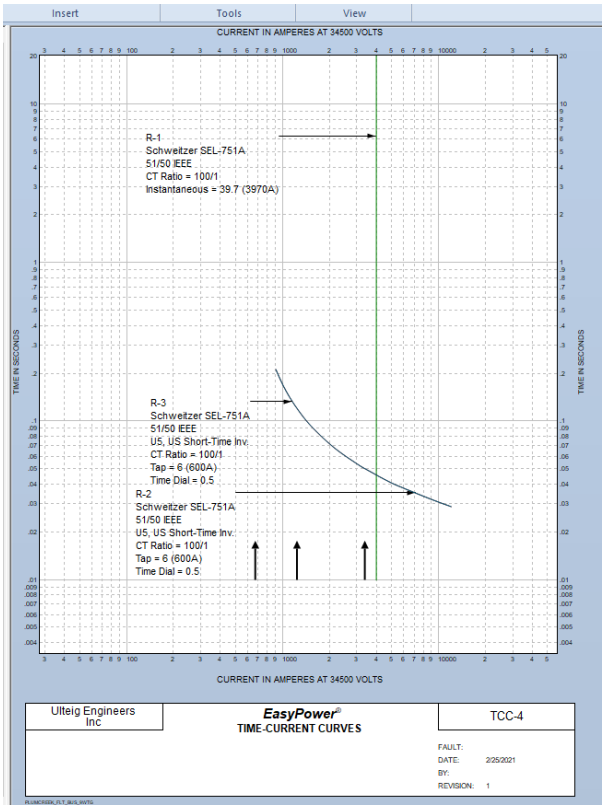

Figure 25. TCC for relays 2 and 3 for 7-bus power system.

2.2.2.1. Testing Results of the Full Relay Protection Scheme Verification Simulation

To verify the proper function of the protection relay system linked to the RTDS, different types of faults at various buses have been considered in the 7-bus power system shown in Fig. 19, including single-phase line to ground, two-phase line to ground, and three phase fault. Fig. 26 – Fig. 50 demonstrate the testing results for the protection relay system under these faults. Fig. 26 - Fig. 29 shows the voltage and current waveforms as well as simulated fault and trip signals at different buses without any fault. Fig. 30 – Fig. 36 shows the voltage and current waveforms simulated by the RTDS, the voltage and current waveforms recorded by the relays, and the simulated fault and trip signals for a single-phase fault on ‘phase A’ on bus 2. Fig. 37 – Fig. 43 show the voltage and current waveforms simulated by the RTDS, the voltage and current waveforms recorded by the relays, and the simulated fault and trip signals for a two-phase fault on

‘phase A’ and ‘phase B’ on bus 4. Fig. 44 – Fig. 50 show the voltage and current waveforms simulated by the RTDS, the voltage and current waveforms recorded by the relays, and the simulated fault and trip signals for a three-phase fault on bus 5.

The results in Fig. 30 - Fig. 36 verify the proper function of the protection relay system for a single-phase fault. It can be seen from Fig. 26 – Fig. 28 that before the fault, there are no faulted voltages and overcurrent, and Fig. 29 shows that ‘FAULT’ signal is low, which means no fault at this time and the trip signal is low. When the single-phase fault is applied to phase A, Fig. 30 shows that the current on ‘phase A’ becomes high when the fault is initiated at bus 2 and becomes zero when the relay operates and the breaker opens. In this case, Fig. 36 shows that the value of the “FAULT” signal is high (shaded box). The breaker would open about 1.7 cycles after the fault. As shown in Fig. 30 and Fig. 31, the voltage and current waveforms simulated at bus 2 by the RTDS are consistent with those recorded at bus 2 by the relay when the fault is occurred at bus 2. Also, Fig. 32-Fig. 35 show that when the fault is occurred at bus 2, the voltage and current waveforms simulated at buses 4 and 5 by the RTDS are consistent with those recorded at buses 4 and 5 by the relays. These results verify the proper function of the protection relay system integrated in the 7-bus test power system under a single-phase fault.

The results in Fig. 37 – Fig. 43 verify the proper function of the protection relay system for a two-phase line to ground fault. It can be seen from Fig. 39 that when the two-phase line to ground fault is initiated at bus 4, the currents on ‘phase A’ and ‘phase B’ become high and then becomes zero when the relay signal opens the breaker. In this case, Fig. 43 shows that the value of the “FAULT” signal is high (shaded box). The breaker would open about 1.7 cycles after the fault. As shown in Fig. 39 and Fig. 40, the voltage and current waveforms simulated at bus 4 by the RTDS match with those recorded at bus 4 by the relay. Also, Fig. 37, Fig. 38, Fig. 41, and Fig. 42 show

that when the fault is occurred at bus 4, the voltage and current waveforms simulated at buses 2 and 5 by the RTDS are consistent with those recorded at buses 2 and 5 by the relays. These results verify the proper function of the protection relay system integrated in the 7-bus test power system under a two-phase line to ground fault.

The results in Fig. 44 – Fig. 50 verify the proper function of the protection relay system for a three-phase line to ground fault. It can be seen from Fig. 48 that when the three-phase line to ground fault is initiated at bus 5, the currents on 'phase A', 'phase B', and 'phase C' at bus 5 become high and then become zero when the relay signal opens the breaker. In this case, Fig. 50 shows that the value of the "FAULT" signal is high (shaded box). The breaker would open about 1.7 cycles after the fault. As shown in Fig. 48 and Fig. 49 the voltage and current waveforms simulated at bus 5 by the RTDS match with those recorded at bus 5 by the relay. Also, Fig. 44-Fig. 47 show that when the fault is occurred at bus 4, the voltage and current waveforms simulated at buses 2 and 4 by the RTDS are consistent with those recorded at buses 2 and 4 by the relays. These results verify the proper function of the protection relay system integrated in the 7-bus test power system under a three-phase line to ground fault.

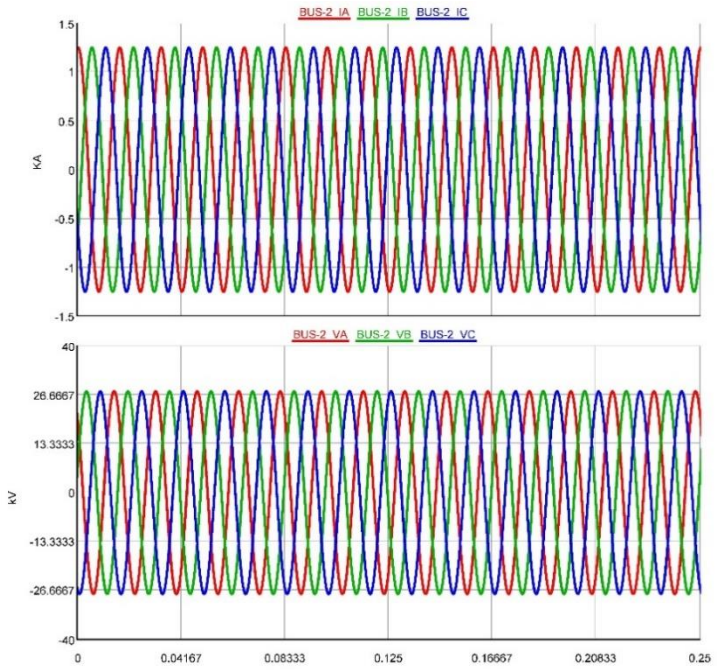

Figure 26. Bus 2 voltage and current waveforms without any fault in the 7-bus power system.

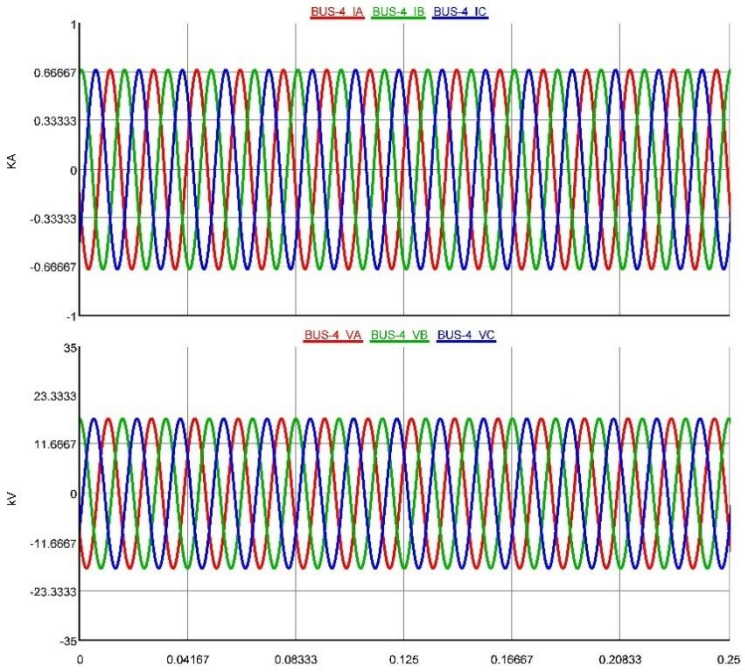

Figure 27. Bus 4 voltage and current waveforms without any fault in the 7-bus power system.

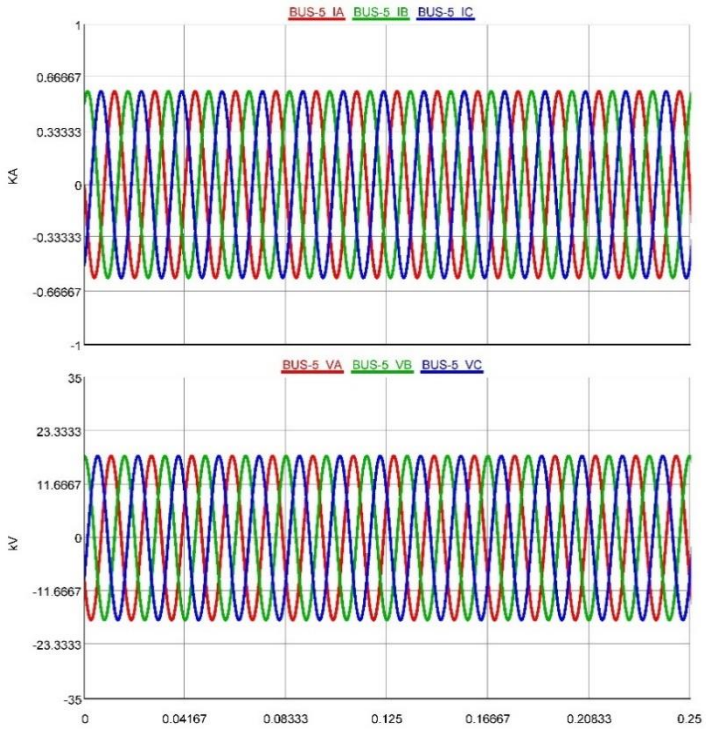

Figure 28. Bus 5 voltage and current waveforms without any fault in the 7-bus power system.

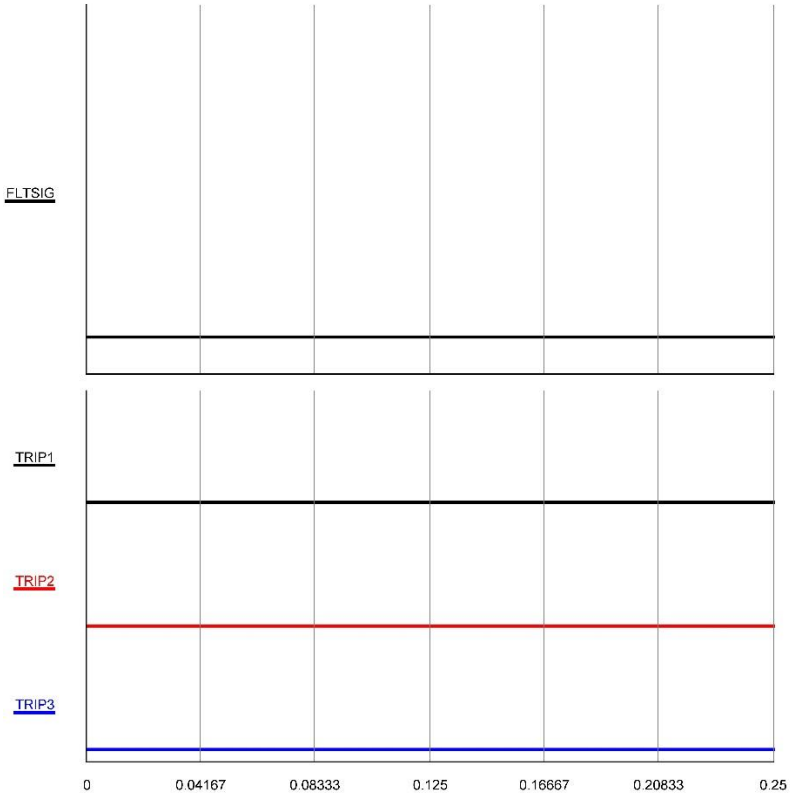

Figure 29. Fault and trip signals without any fault in the 7-bus power system.

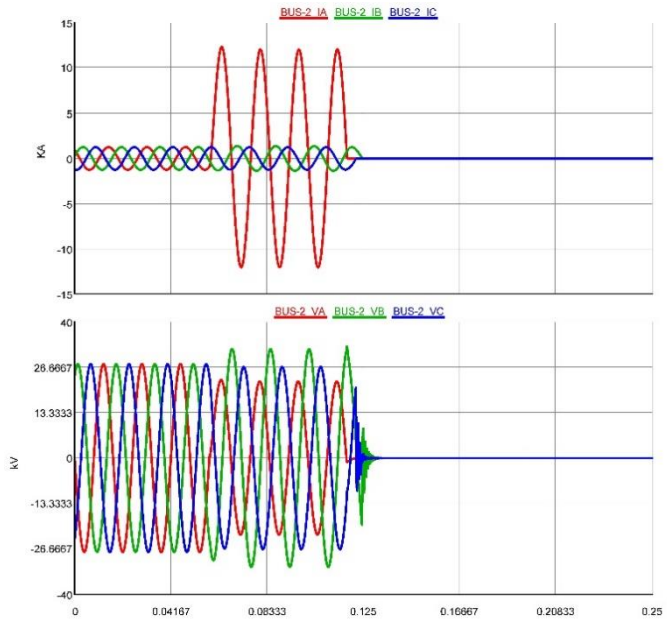

Figure 30. Bus 2 voltage and current waveforms for a single-phase line to ground fault on ‘phase A’ on bus 2 in the 7-bus power system.

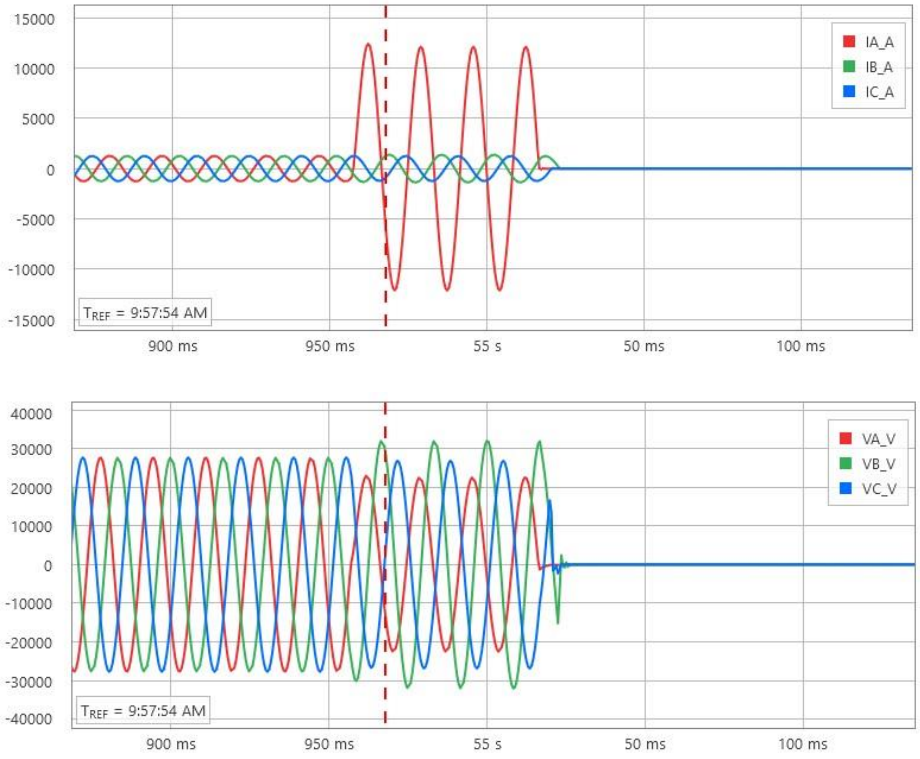

Figure 31. Bus 2 voltage and current waveforms recorded by the relay for a single-phase line to ground fault on ‘phase A’ on bus 2 in the 7-bus power system.

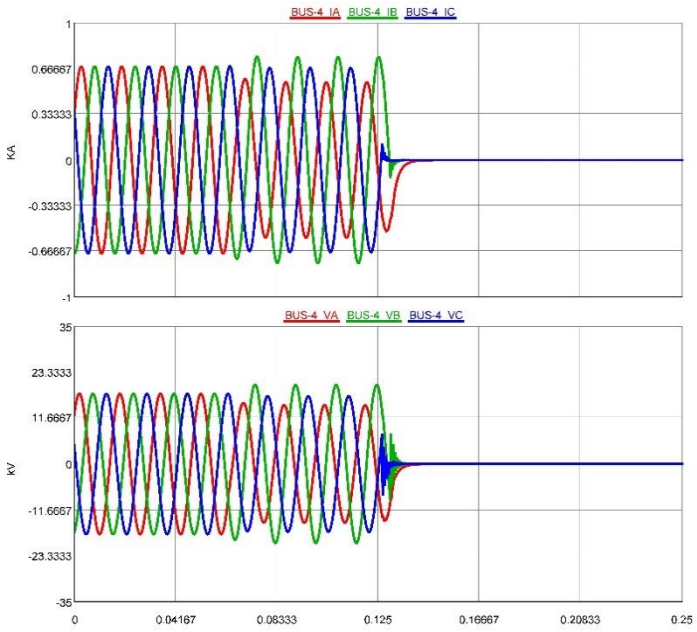

Figure 32. Bus 4 voltage and current waveforms for a single-phase line to ground fault on ‘phase A’ on bus 2 in the 7-bus power system.

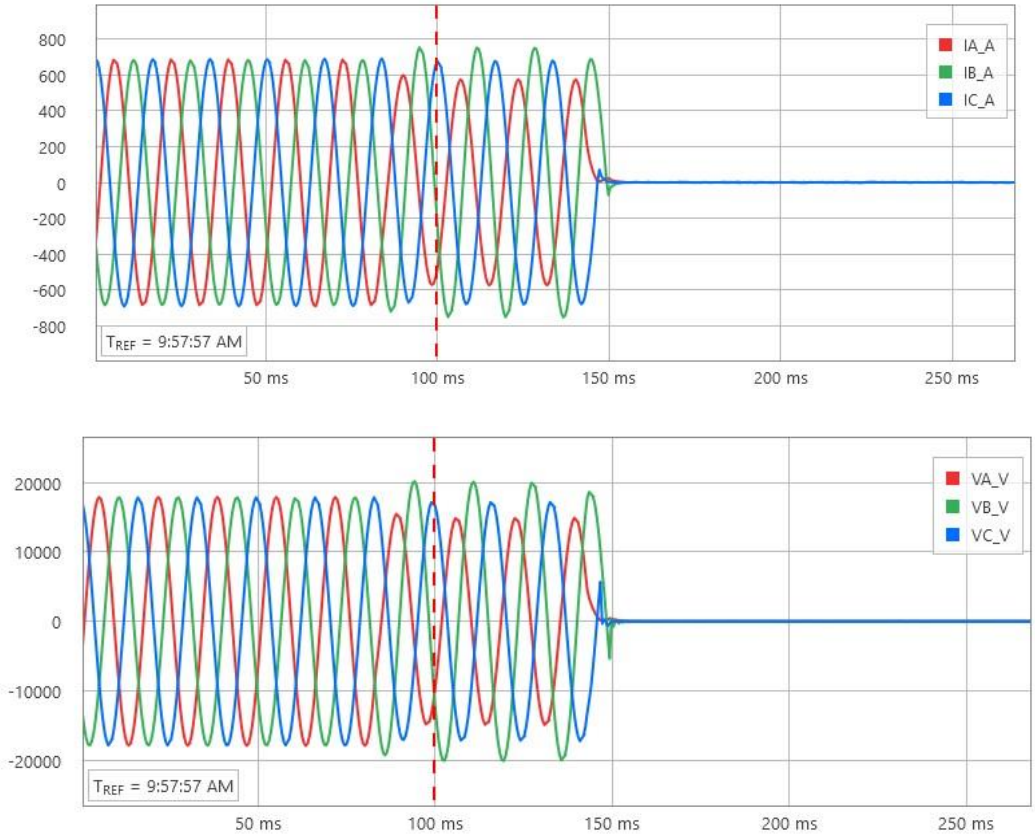

Figure 33. Bus 4 voltage and current waveforms recorded by the relay for a single-phase line to ground fault on ‘phase A’ on bus 2 in the 7-bus power system.

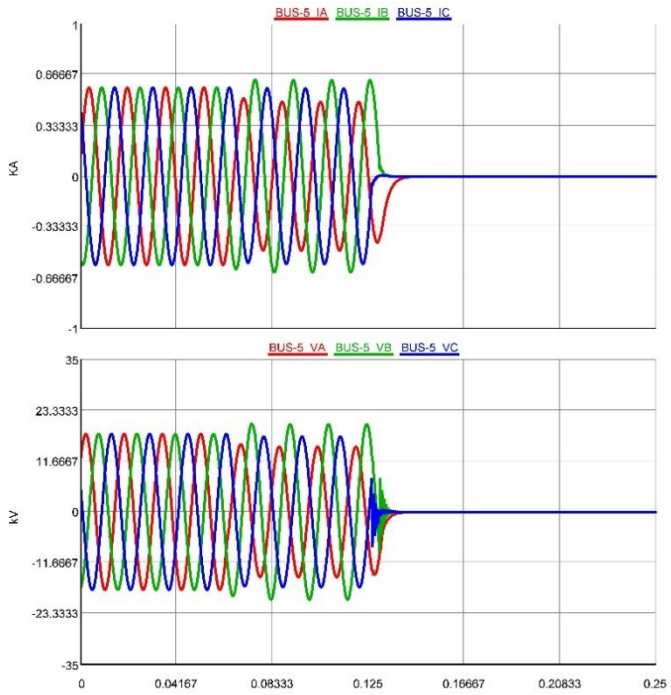

Figure 34. Bus 5 voltage and current waveforms for a single-phase line to ground fault on ‘phase A’ on bus 2 in the 7-bus power system.

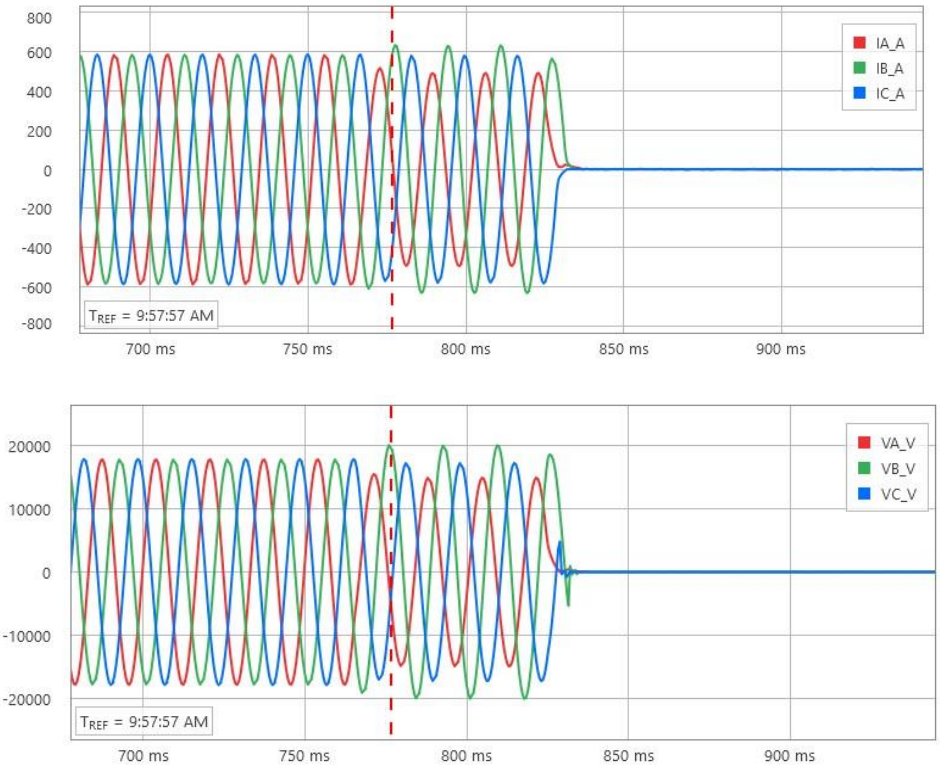

Figure 35. Bus 5 voltage and current waveforms recorded by the relay for a single-phase line to ground fault on ‘phase A’ on bus 2 in the 7-bus power system.

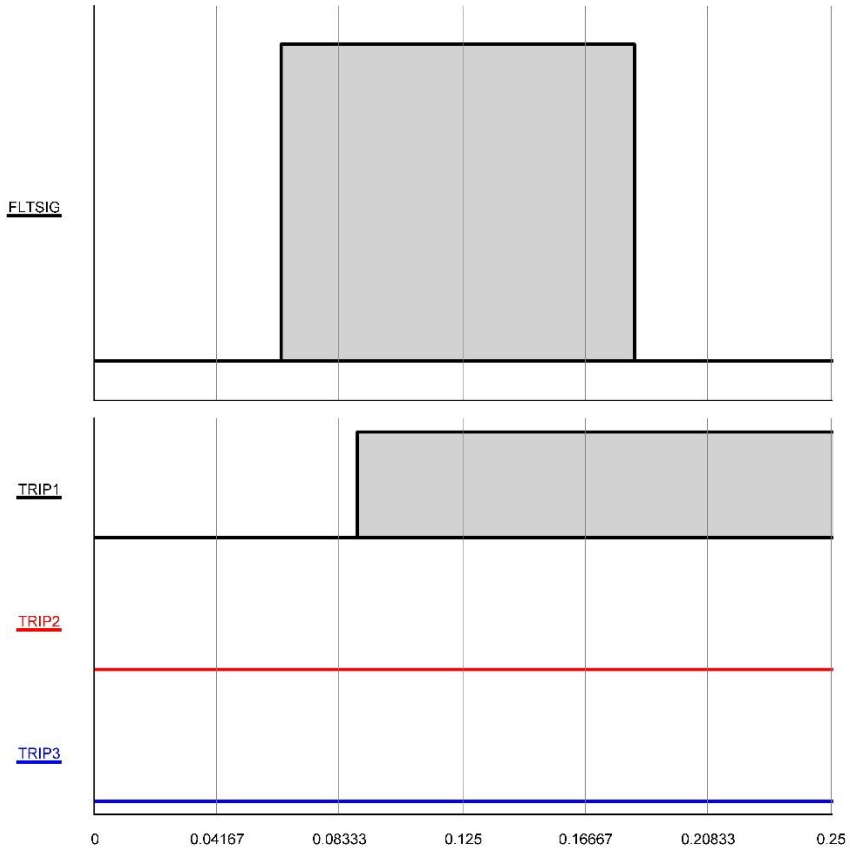

Figure 36. Fault and trip signals for a single-phase line to ground fault on ‘phase A’ on bus 2 in the 7-bus power system.

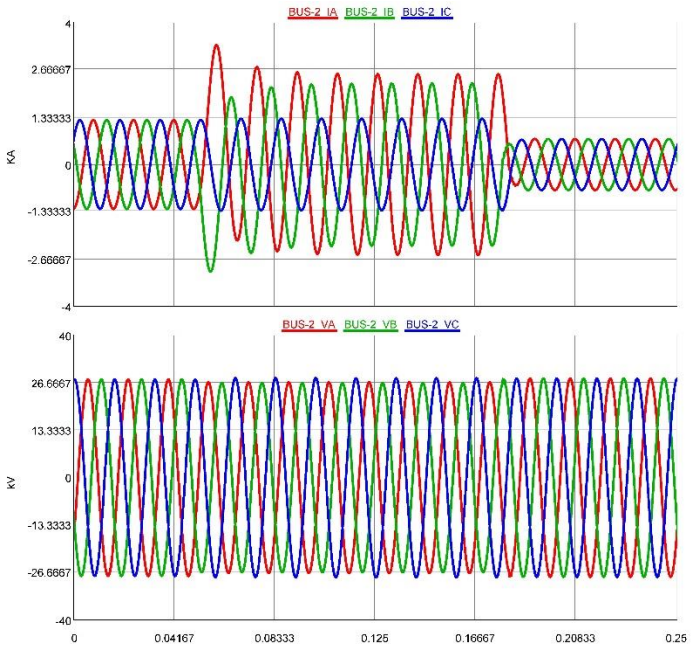

Figure 37. Bus 2 voltage and current waveforms for a two-phase line to ground fault on ‘phase A’ and ‘phase B’ on bus 4 in the 7-bus power system.

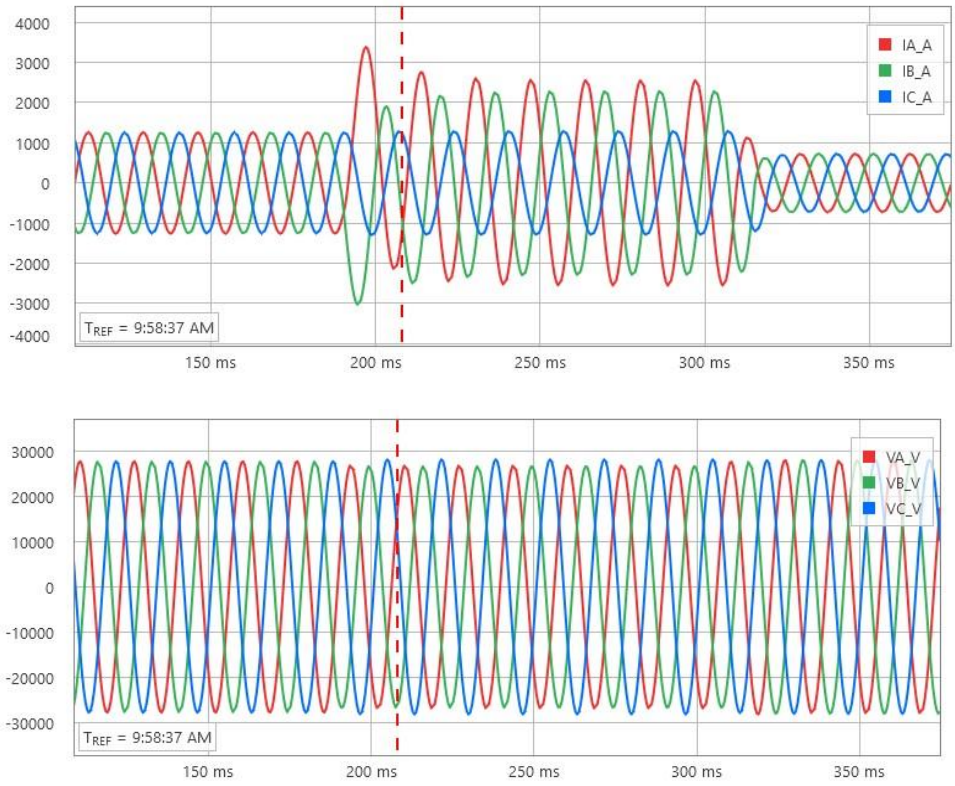

Figure 38. Bus 2 voltage and current waveforms recorded by the relay for a two-phase line to ground fault on ‘phase A’ and ‘phase B’ on bus 4 in the 7-bus power system.

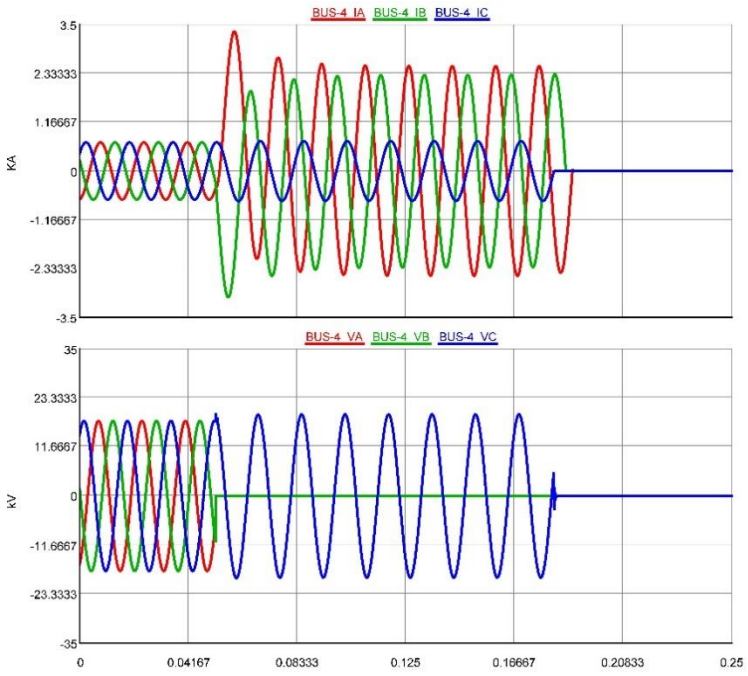

Figure 39. Bus 4 voltage and current waveforms for a two-phase line to ground fault on ‘phase A’ and ‘phase B’ on bus 4 in the 7-bus power system.

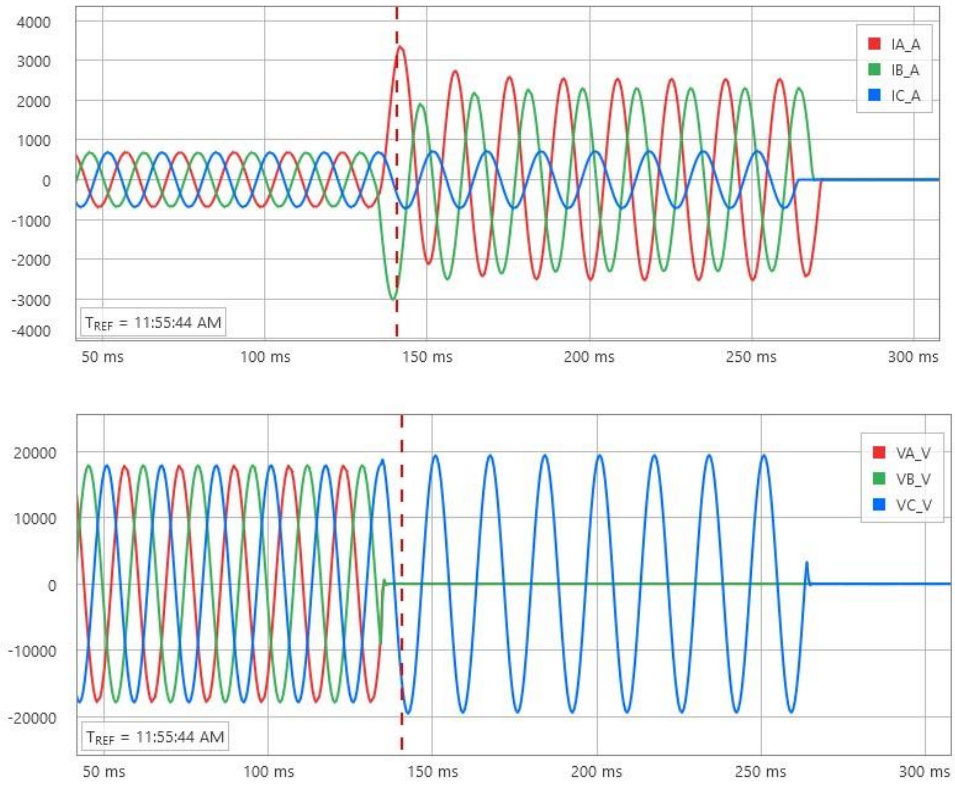

Figure 40. Bus 4 voltage and current waveforms recorded by the relay for a two-phase line to ground fault on ‘phase A’ and ‘phase B’ on bus 4 in the 7-bus power system.

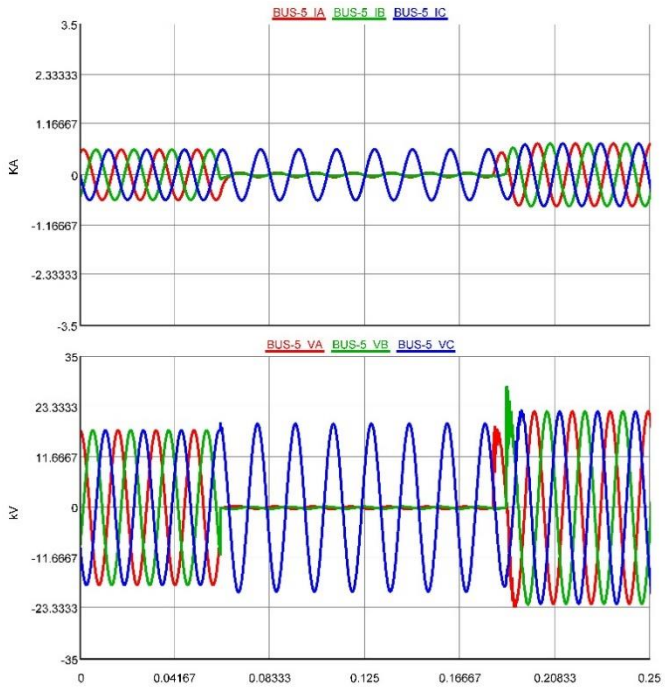

Figure 41. Bus 5 voltage and current waveforms for a two-phase line to ground fault on ‘phase A’ and ‘phase B’ on bus 4 in the 7-bus power system.

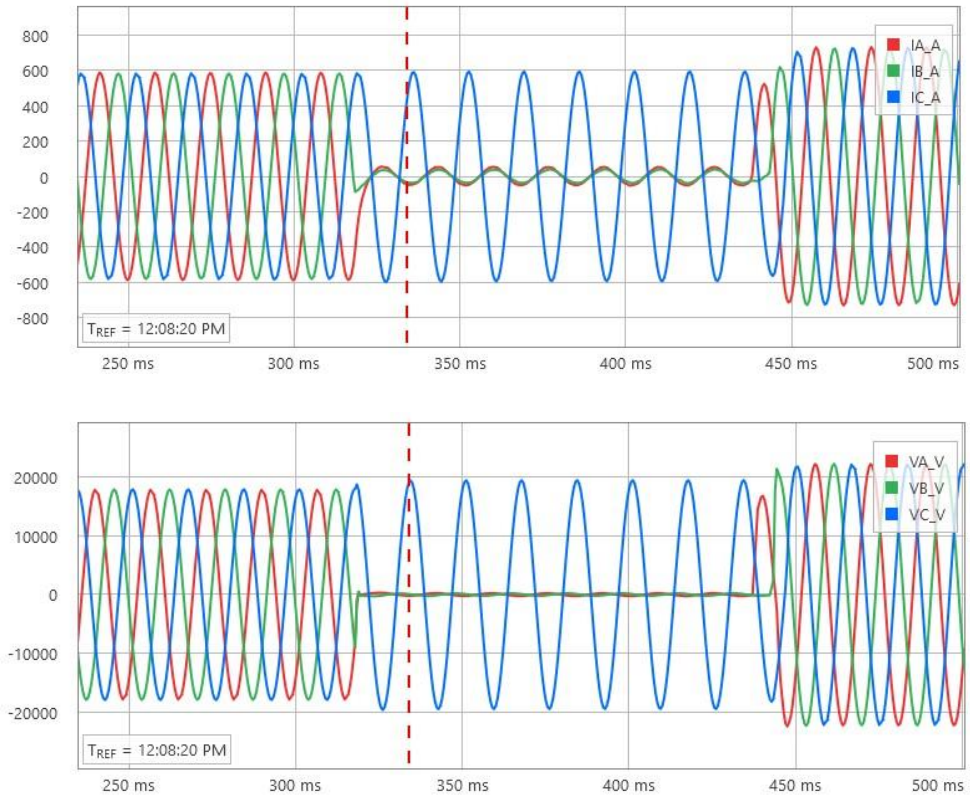

Figure 42. Bus 5 voltage and current waveforms recorded by the relay for a two-phase line to ground fault on ‘phase A’ and ‘phase B’ on bus 4 in the 7-bus power system.

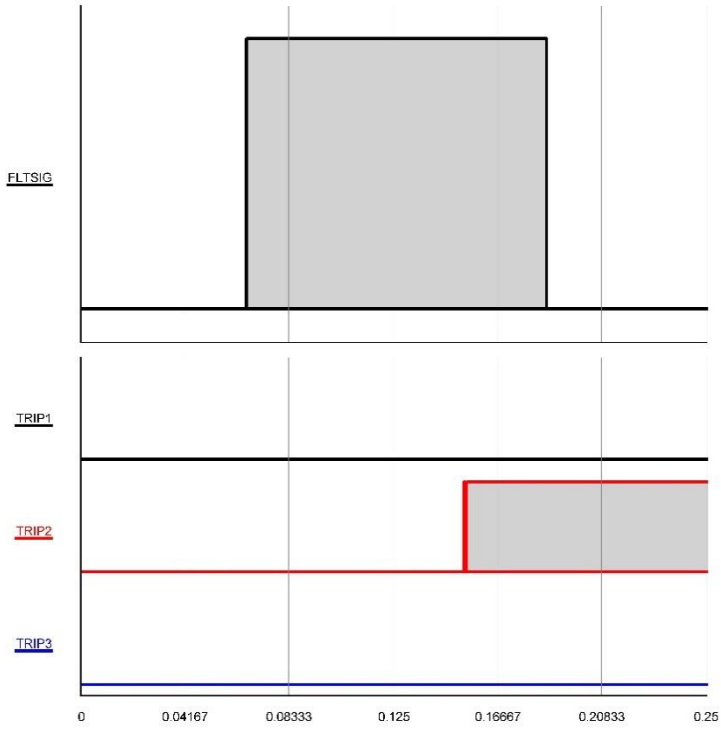

Figure 43. Fault and trip signals for a two-phase line to ground fault on ‘phase A’ and ‘phase B’ on bus 4 in the 7-bus power system.

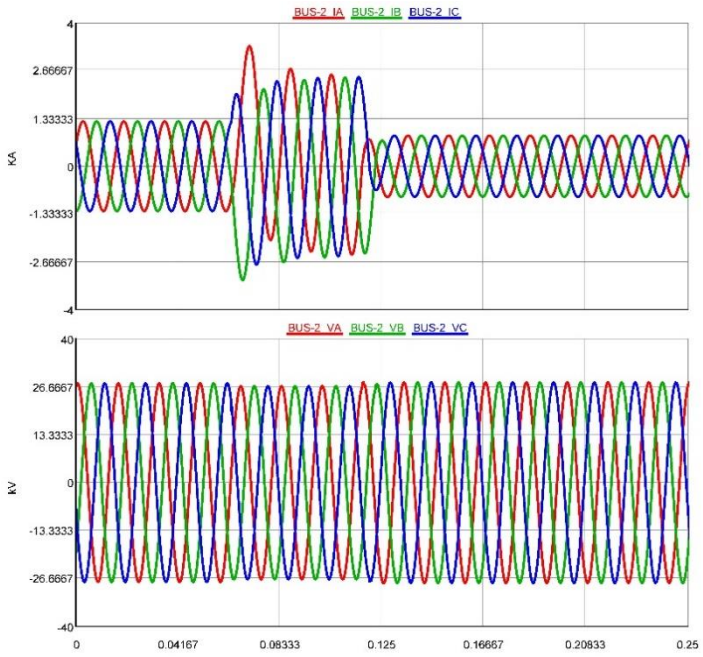

Figure 44. Bus 2 voltage and current waveforms for a three-phase fault on bus 5 in the 7-bus power system.

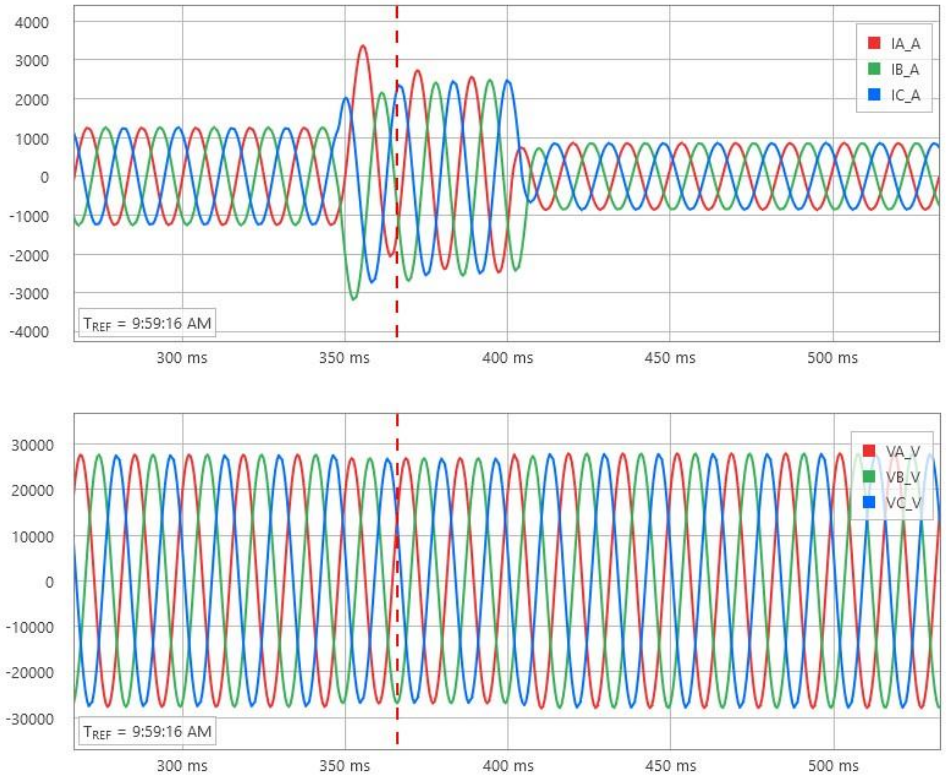

Figure 45. Bus 2 voltage and current waveforms recorded by the relay for a three-phase fault on bus 5 in the 7-bus power system.

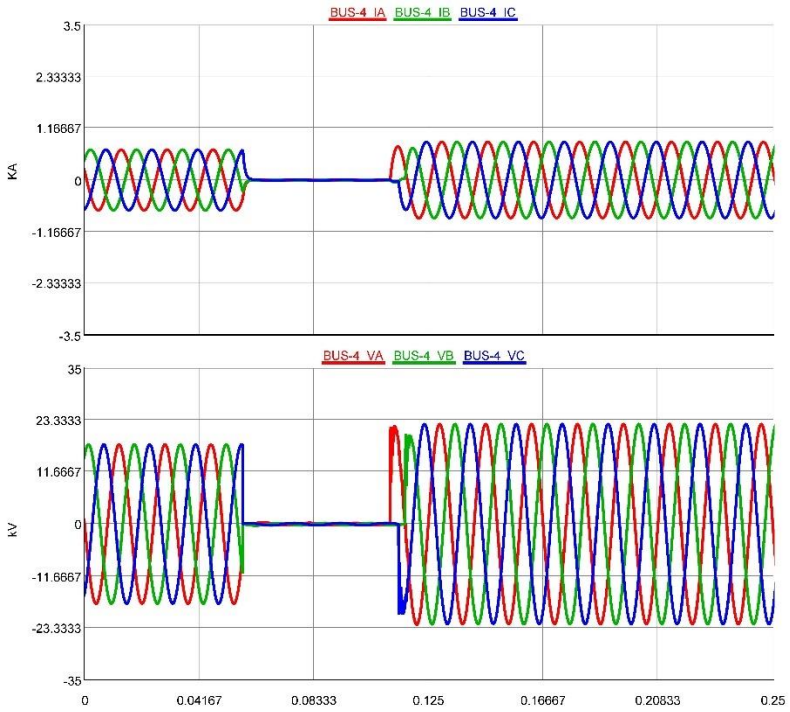

Figure 46. Bus 4 voltage and current waveforms for a three-phase fault on bus 5 in the 7-bus power system.

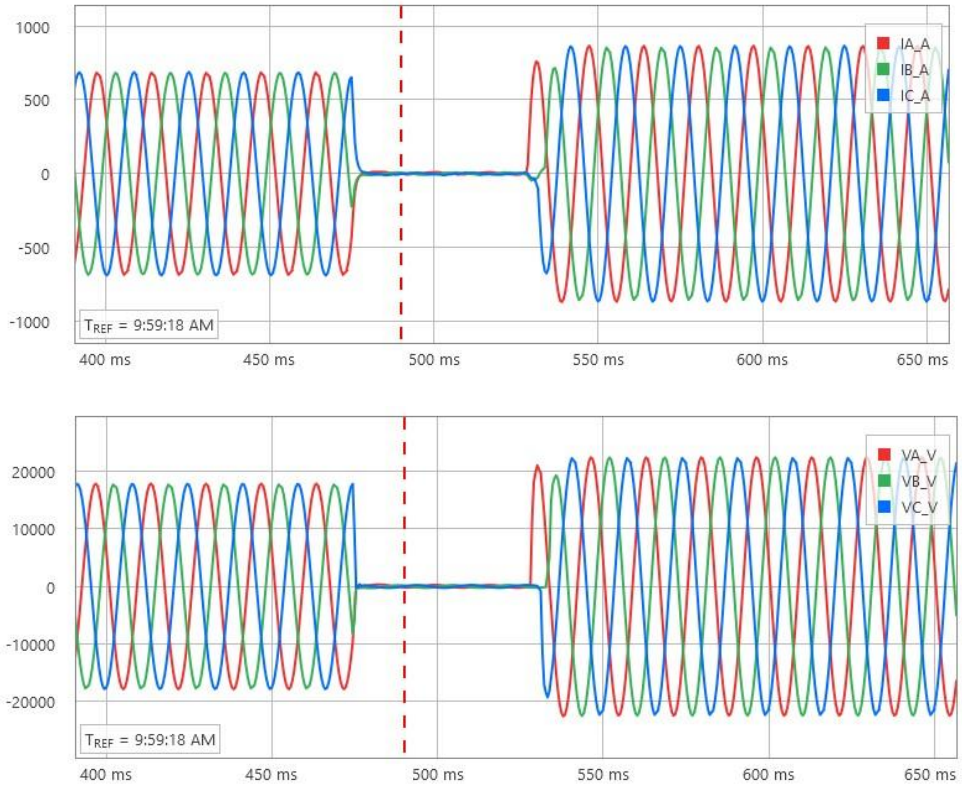

Figure 47. Bus 4 voltage and current waveforms recorded by the relay for a three-phase fault on bus 5 in the 7-bus power system.

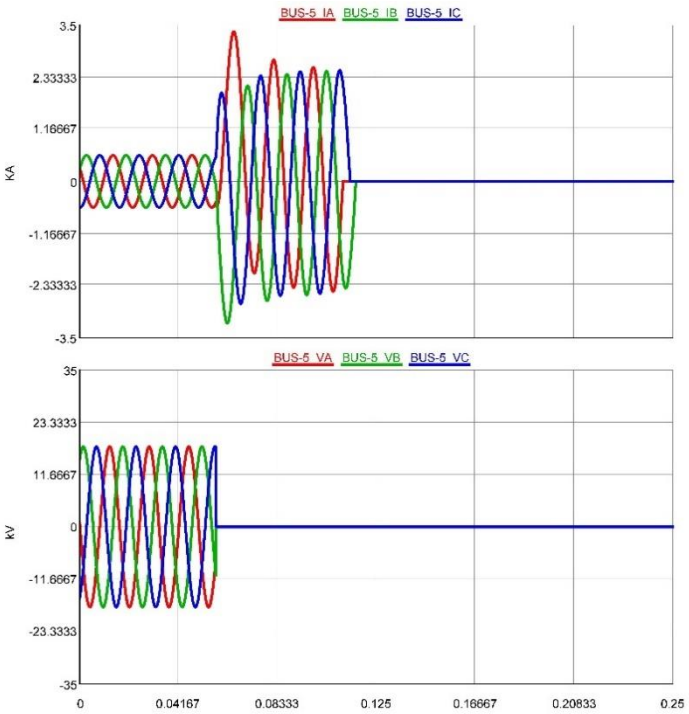

Figure 48. Bus 5 voltage and current waveforms for a three-phase fault on bus 5 in the 7-bus power system.

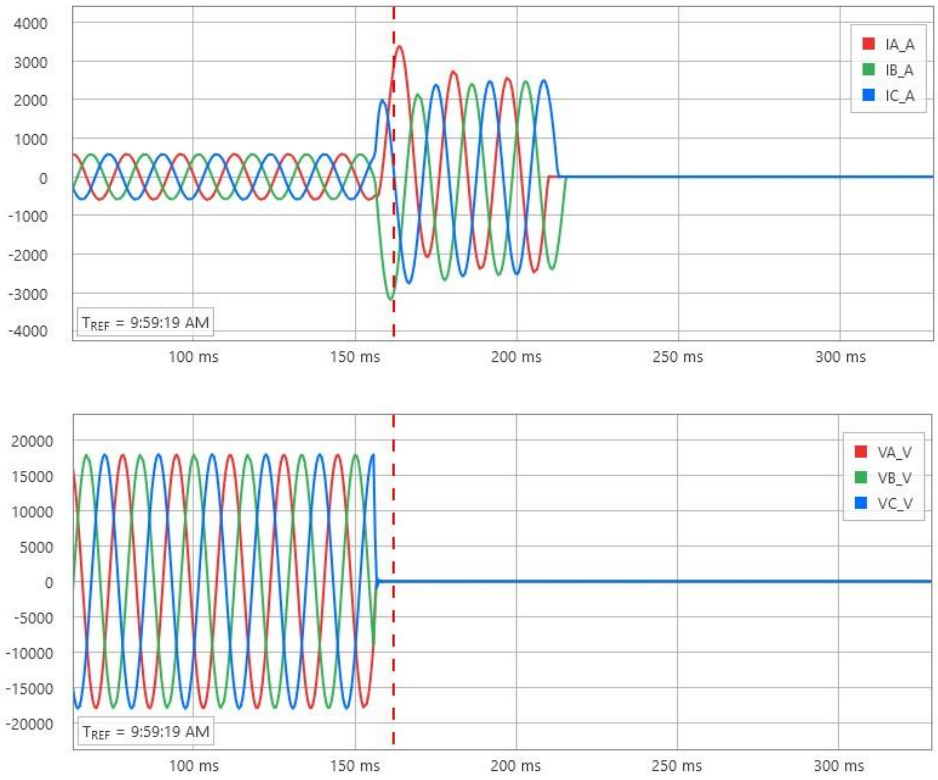

Figure 49. Bus 5 voltage and current waveforms recorded by the relay for a three-phase fault on bus 5 in the 7-bus power system.

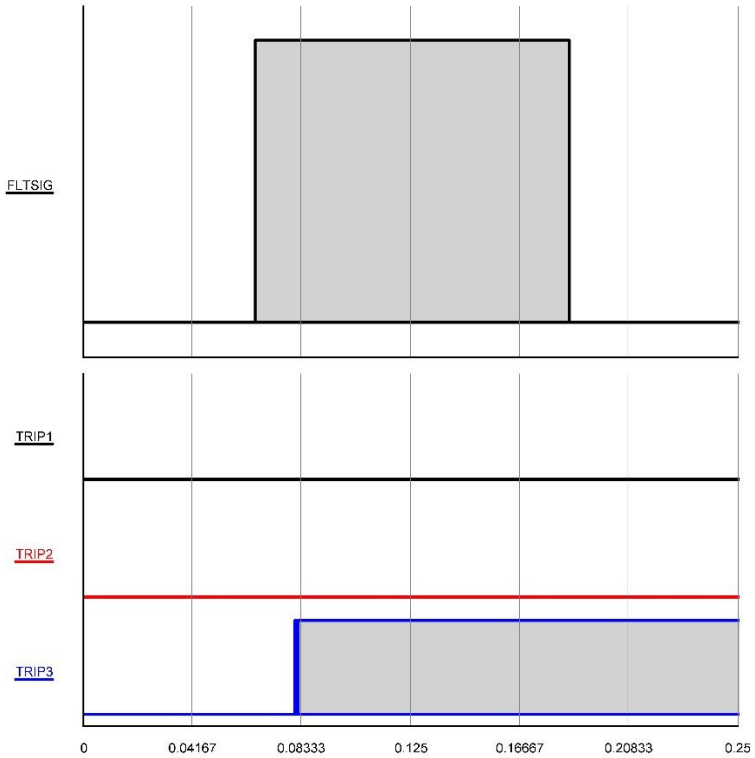

Figure 50. Fault and trip signals for a three-phase fault on bus 5 in the 7-bus power system.

3. ASSESSMENT OF SHUNT CAPACITORS FOR RENEWABLE ENERGY RESOURCES ON GRID STRENGTH

The high penetration of renewable energy resources, such as wind and solar, is integrated into the electric power grid through a power electronic interface. As a group, these types of resources are commonly referred to as inverter-based resources (IBRs). While IBRs offer fast and advanced control for energy efficiency, they are also challenging grid planning and operation. Particularly, IBRs provide expected real and reactive power based on inverters, which separate the power sources from the grid. As the grid becomes weak, the voltage reference becomes less stable, and control dynamics and tuning become increasingly influential on overall grid behavior [14].

Potential weak grid issues are analyzed and identified based on grid strength assessment. In the assessment, short circuit ratio (SCR) is a metric recommended by North American Electric Reliability Corporation to quantify the grid strength [14][15]. In the past, SCR was used to analyze the impact of the AC/DC system interactions on the AC-side grid strength involving power electronics interface [16][17]. More recently, SCR has been used to analyze the strength of the power grid for renewable energy integration [18]-[20]. The commonly used SCR calculation method ignores the interactions among IBRs and thus may give an inaccurate estimation of grid strength at points of interconnection (POIs) for IBRs [21]-[23]. To consider the effect of IBRs interactions on grid strength, several new methods have been developed such as the composite SCR (CSCR) developed by General Electric Energy Consulting [23], the weighted SCR (WSCR) developed by the Electric Reliability Council of Texas [21], and the site-dependent SCR (SDSCR) [22]. Although SDSCR can provide more accurate results of grid strength assessment than the other methods mentioned, it does not consider the impact of capacitor compensations at POIs on

grid strength since SDSCR is the extension of the concept of SCR that initially excludes such impact.

To address this issue, this chapter presents a new method for grid strength assessment by extending the concept of effective SCR (ESCR). ESCR considers this impact of capacitors for grid strength assessment at POIs [24], but it is not appropriate to use it for grid strength assessment in a power grid with multiple IBRs and capacitors at different POIs, since it does not consider 1) the interaction effect of IBRs at different sites on grid strength and 2) the interaction of capacitors at different sites on grid strength. To overcome these shortcomings, we first analyze how a capacitor affects grid strength from the perspective of static voltage stability in a power grid with a single IBR. Then, the analysis results are extended to a power grid with multiple IBRs and capacitors at different sites to propose an effective site-dependent SCR (ESDSCR) method for grid strength assessment. The new method can consider the impacts of the interactions between IBRs and between capacitors. The efficacy of this proposed method is demonstrated on the IEEE 39-bus system.

3.1. Impact of Capacitor Compensation on Grid Strength

3.1.1. Voltage Stability Analysis in a Power Grid with a Single IBR and Capacitor Compensation

For a power system with a single IBR, its voltage stability can be analyzed in an equivalent two-bus power system as shown in Fig. 51. In the equivalent system, the power equation can be represented as:

$$\frac{(V_i - V_s')}{Z_i'} = I_i = \left(\frac{S_i}{V_i}\right)^* \tag{1}$$

where Si is the complex power injected from IBR at bus i into the AC system; Vi is the voltages at bus i; V's is the equivalent source voltage at bus s; and Z'i is the equivalent Thevenin impedance

including shunt capacitive susceptance bc (or shunt capacitive reactance XC consistent with the one in (3)) at bus i. V's and Z'i can be further represented as:

$$V_s' = V_s \frac{Z_i'}{Z_i} \tag{2}$$

$$\frac{1}{Z_i'} = (\frac{1}{Z_i} - jb_c) = (\frac{1}{Z_i} - j\frac{1}{X_c}) \tag{3}$$

where Vs is the voltage at bus s; Zi is the Thevenin impedance at bus i.

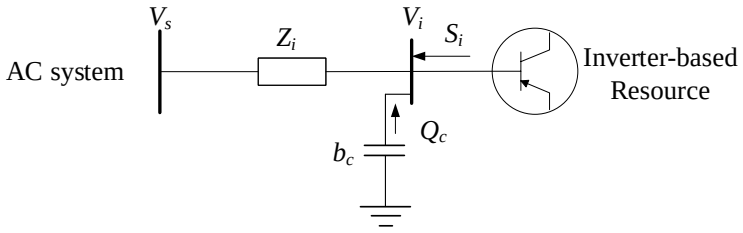

Figure 51. Equivalence of an AC power system with a single IBR and a shunt capacitor.

To analyze the voltage stability of the system shown in Fig. 51, (1) is rewritten as:

$$Z_i' S_i^* = |V_i|^2 - V_s' V_i^* \tag{4}$$

where symbol |·| indicates the magnitude of a variable.

Let $Z'_i S_i^* = a - jb$, where a and b are both real numbers. Based on (4), parameters a and b can be represented as:

$$a = |V_i|^2 - |V_s'||V_i|\cos\theta_{si} \tag{5}$$

$$b = |V_s'||V_i|\sin\theta_{si} \tag{6}$$

where $\theta'_{si} = \theta'_s - \theta_i$ is the angular difference between the voltages V'_s and V_i.

When the magnitude of the AC system voltage V'_s is constant, a and b are functions of V_i and θ_{si}. Thus, they can be represented as:

$$a = f_1(|V_i|, \theta_{si}) = |V_i|^2 - |V_s'||V_i|\cos\theta_{si}' \tag{7}$$

$$b = f_2(|V_i|, \theta_{si}) = |V_s'||V_i|\sin\theta_{si}' \tag{8}$$

The Jacobian matrix of $f = [f_1, f_2]^T$ can be represented as:

$$\boldsymbol{J} = \begin{bmatrix} \frac{\partial f_1}{\partial |V_i|} & \frac{\partial f_1}{\partial \theta_{si}} \\ \frac{\partial f_2}{\partial |V_i|} & \frac{\partial f_2}{\partial \theta_{si}} \end{bmatrix} = \begin{bmatrix} 2|V_i| - |V_s'|\cos\theta_{si}' & |V_s'||V_i|\sin\theta_{si}' \\ |V_s'|\sin\theta_{si}' & |V_s'||V_i|\cos\theta_{si}' \end{bmatrix} \tag{9}$$

Voltage instability occurs at bus *i* when the Jacobian matrix ***J*** in (9) is singular. Thus, the boundary condition for voltage stability is such that the determinant of the matrix ***J*** attains zero, i.e., $det(\boldsymbol{J}) = 0$. By solving this equation, the boundary condition for voltage stability at bus *i* can be represented as:

$$\frac{|V_i|\cos\theta_{si}'}{|V_s'|} = \mathrm{Re}\left[\frac{V_i}{V_s'}\right] = \frac{1}{2} \tag{10}$$

Thus, we have

$$\frac{V_i}{V_s'} = \frac{1}{2} + jc \tag{11}$$

where *c* is a real number.

By dividing $|V_i|^2$ at both sides of (4), (4) can be rewritten:

$$\frac{V_i}{V_s'} = \frac{1}{1 - \frac{Z_i S_i^*}{|V_i|^2}} \tag{12}$$

Based on (11) and (12), we can obtain

$$\frac{|S_i^*||Z_i|}{|V_i|^2} = \left|1 - \frac{1}{\frac{1}{2} + jc}\right| = 1 \tag{13}$$

Equation (13) can be rewritten as:

$$r_i = \frac{|V_i|^2}{|S_i^*||Z_i'|} = \frac{|S_{ac,i}'|}{|S_i^*|} = \frac{\left|\frac{|V_i|^2}{Z_i} - j\frac{|V_i|^2}{X_c}\right|}{|S_i^*|} = \frac{|S_{ac,i} - jQ_{c,i}|}{|S_i^*|} = 1 \tag{14}$$

where $|S'_{ac,i}|=|V_i|^2/|Z'_i|$ is the equivalent short-circuit capacity at bus i, which considers the impact of shunt capacitor at bus i; $|S^*_i|$ is the magnitude of conjugated complex power injected into bus i from the connected IBR; $|S_{ac,i}|=|V_i|^2/|Z_i|$ is the short-circuit capacity at bus i, which excludes the impact of shunt capacity; and $Q_{c,i}=|V_i|^2/X_C$ is the reactive compensation from shunt capacitor at bus i.

Equation (14) shows the voltage stability at bus i can be identified by comparing the complex power injected from the IBR at bus i (i.e., $|S^*_i|$) with its equivalent short-circuit capacity (i.e., $|S'_{ac,i}|$). The voltage is stable at bus i if the power injected from the IBR is larger or equal to equivalent short-circuit capacity. More importantly, (14) shows that when there is a shunt capacitor in the system, it is required to use equivalent short-circuit capacity rather than short-circuit capacity for voltage stability analysis. Different from short-circuit capacity, the equivalent short-circuit capacity includes the reactive compensation from the shunt capacitor. Thus, if short-circuit capacity is used rather than the equivalent one, the results of stability analysis may be over-optimistic.

3.1.2. Impact of Shunt Capacitor on Grid Strength

The stability condition in (14) can be used to analyze the impact of shunt capacitor on grid strength from the perspective of static voltage stability. In the system shown in Fig. 51, the grid strength at bus i can be quantified by ESCR, which can be defined as [24],

$$ESCR_i = \frac{|S_{ac,i} - jQ_{c,i}|}{P_{d,i}} \tag{15}$$

where $P_{d,i}$ is the real power injection of the IBR at POI i.

Compared with the stability condition in (14) with ESCR defined in (15), it is found that ESCR quantifies the strength of the AC grid relative to the real power of the IBR at a POI in terms of static voltage stability. Larger $ESCR_i$ indicates that the grid is stronger at POI *i* since the voltage at POI *i* is distant from its voltage stability limit. In general, the strength of the AC grid at a POI can be quantified using the following ESCR ranges: the grid is considered to be strong at a POI if its ESCR value is larger than 3; the grid is weak at a POI if its ESCR value is between 2 and 3; and the grid is very weak at a bus if its ESCR value is smaller than 2. From (11), it can be concluded that when the ESCR is equal to 1, voltage at POI *i* is in its collapse point; when the $ESCR_i$ is smaller than 1, the system voltage becomes unstable. Notice that ESCR considers the impact of the reactive compensation from shunt capacitor at POI on grid strength. If such impact is ignored, the results of grid strength assessment may be inaccurate.

3.2. Proposed Method for Grid Strength Assessment Considering Interaction Between Capacitors

In a power grid with multiple IBRs and capacitors, IBRs interconnected through the power network interact with each other, especially when they are electrically close. Moreover, the capacitors interconnected through the power network also interact with each other. Both two types of interactions can affect the grid strength at POIs. However, the effect of both of the two types of interactions on grid strength does not considered in the ESCR defined in (15). In this section, a new method for grid strength assessment will be proposed to consider the two types of interaction together by extending the study model of a single IBR and shunt capacitor to a power grid with multiple IBRs and shunt capacitors. First, the voltage stability in the power grid with multiple IBRs and shunt capacitors will be analyzed. Then, a method will be proposed for evaluating grid strength.

3.2.1. Voltage Stability Analysis in a Power Grid with Multiple IBRs and Capacitors

For a power grid with multiple IBRs and shunt capacitors as shown in Fig. 52, its network equation can be represented

$$\begin{bmatrix} \boldsymbol{V}_G \\ \boldsymbol{V}_R \end{bmatrix} = \begin{bmatrix} \boldsymbol{Z}_{GG} & \boldsymbol{Z}_{GR} \\ \boldsymbol{Z}_{RG} & \boldsymbol{Z}_{RR} \end{bmatrix} \begin{bmatrix} \boldsymbol{I}_G \\ \boldsymbol{I}_R + \boldsymbol{I}_{SC} \end{bmatrix} \tag{16}$$

where $\boldsymbol{I_G}$, $\boldsymbol{I_R}$, and $\boldsymbol{I_{SC}}$ are vectors of current injection into the buses connected with synchronous generators, with IBRs, and with shunt capacitors, respectively; $\boldsymbol{V_G}$ and $\boldsymbol{V_R}$ are vectors of voltages at the synchronous generator buses and at the IBR buses; and sub-matrices $\boldsymbol{Z_{GG}}$, $\boldsymbol{Z_{GR}}$, $\boldsymbol{Z_{RG}}$, and $\boldsymbol{Z_{RR}}$ are the corresponding blocks of the bus impedance matrix.

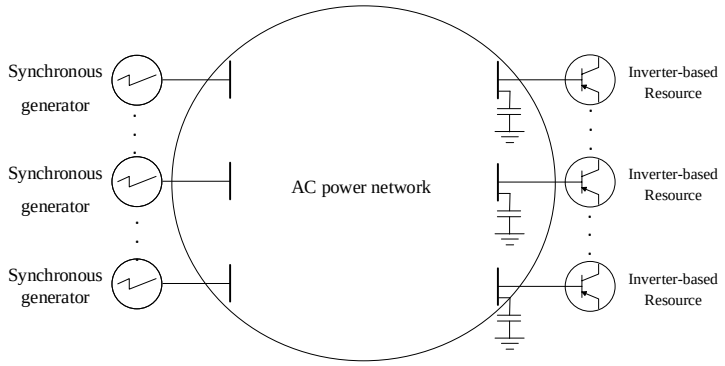

Figure 52. An AC power system with multiple IBRs and shunt capacitors.

Based on (13), the voltage stability boundary condition in the system can be derived. Specifically, the voltage at bus *i* connected to an IBR can be represented as:

$$V_{R,i} = \sum_{k \in \boldsymbol{G}} Z_{RG,ik} I_{G,k} + Z_{RR,ii} \sum_{j \in \boldsymbol{R}} \frac{Z_{RR,ij}}{Z_{RR,ii}} (I_{R,j} + I_{SC,j}) \tag{17}$$

where $V_{R,i}$ is the i^{th} element in the voltage vector $\boldsymbol{V_R}$; $I_{G,k}$ is the k^{th} element in the current vector $\boldsymbol{I_G}$; $I_{R,j}$ and $I_{SC,j}$ are the j^{th} element in the current vectors $\boldsymbol{I_R}$ and $\boldsymbol{I_{SC}}$, respectively; $Z_{RG,ik}$ is the $(i,k)^{\text{th}}$ element in the matrix $\boldsymbol{Z_{RG}}$; $Z_{RR,ij}$ is the $(i,j)^{\text{th}}$ element in the matrix $\boldsymbol{Z_{RR}}$; $\boldsymbol{G}$ is the set of all buses

connected with synchronous generators; and $\boldsymbol{R}$ is the set of all buses connected with IBRs and shunt capacitors.

Equation (14) can be rewritten as:

$$\frac{V_{R,i}-V'_{S,i}}{Z'_{RR,ii}} = I_{eq,i} = \left(\frac{S_{eq,i}}{V_{R,i}}\right)^* \tag{18}$$

where

$$V'_{S,i} = \frac{Z'_{RR,ii}}{Z_{RR,ii}} \sum_{k\in\boldsymbol{G}} Z_{RG,ik} I_{G,k} \tag{19}$$

$$\frac{1}{Z'_{RR,ii}} = \left[\frac{1}{Z_{RR,ii}} - jb_{c,eq,i}\right] \tag{20}$$

$$\begin{aligned} b_{c,eq,i} &= b_{c,i} + \sum_{j\in\boldsymbol{R},\, j\neq i} \frac{Z_{RR,ij}}{Z_{RR,ii}} \frac{V_{R,j}}{V_{R,i}} b_{c,j} \\ &= \frac{1}{X_{c,i}} + \sum_{j\in\boldsymbol{R},\, j\neq i} \frac{Z_{RR,ij}}{Z_{RR,ii}} \frac{V_{R,j}}{V_{R,i}} \left(\frac{1}{X_{c,j}}\right) \end{aligned} \tag{21}$$

$$I_{eq,i} = \sum_{j\in\boldsymbol{R}} \frac{Z_{RR,ij}}{Z_{RR,ii}} I_{R,j} = I_{R,i} + \sum_{j\in\boldsymbol{R},\, j\neq i} \frac{Z_{RR,ij}}{Z_{RR,ii}} I_{R,j} \tag{22}$$

$$\begin{aligned} S_{eq,i} &= V_{R,i} I^*_{eq,i} = V_{R,i}\left(I^*_{R,i} + \sum_{j\in\boldsymbol{R},\, j\neq i} \frac{Z^*_{RR,ij}}{Z^*_{RR,ii}} I^*_{R,j}\right) \\ &= \left(S_{R,i} + \sum_{j\in\boldsymbol{R},\, j\neq i} \frac{Z^*_{RR,ij}}{Z^*_{RR,ii}} \frac{V_{R,i}}{V_{R,j}} S_{R,j}\right) \end{aligned} \tag{23}$$

Equation (18) is similar to (1) in format. Equation (1) is the power flow equation of a two-bus power system with a single IBR and a shunt capacitor. Similarly, (18) can be considered as the power flow equation of the equivalent two-bus power system as shown in Fig. 53, which is the equivalent model of the power system in Fig. 52 referred at bus *i*. In the equivalent system of Fig. 53, $V'_{S,i}$, $Z'_{RR,ii}$, and $S_{eq,i}$ each represents the voltage source, equivalent Thevenin impedance, and the complex power injection at bus *i*. As shown in (20), the equivalent Thevenin impedance $Z'_{RR,ii}$

considers the impact of the shunt capacitor connected to bus *i* (i.e., $X_{c,i}$) and the impact of the other shunt capacitors connected to other buses (i.e., $X_{c,j}$). Also, as shown in (23), the equivalent power injection $S_{eq,i}$ includes the power injection from the IBR directly connected to bus *i* (i.e., $S_{R,i}$) and the power injection from the other IBRs (i.e., $S_{R,j}$). Thus, $Z'_{RR,ii}$ in (20) reflects the combined effect of the shunt capacitors at different sites in the system while $S_{eq,i}$ in (23) considers the combined effect of the power injections of the IBRs distributed at different sites in the system.

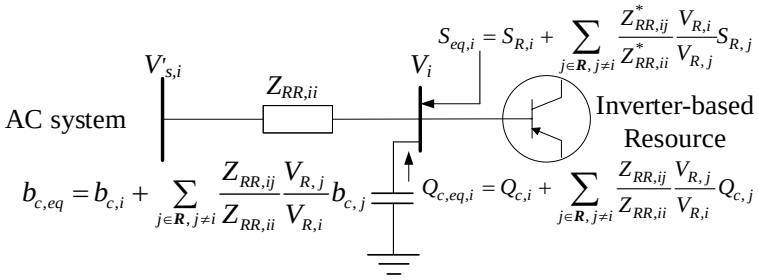

Figure 53. Equivalence of an AC power system with multiple IBRs and shunt capacitors at a POI.

By following the derivation as shown in (4)-(13), (18) can be used to similarly derive the boundary condition for voltage stability at bus *i* in the power system with multiple IBRs and shunt capacitors:

$$r'_i = \frac{|V_{R,i}|^2}{\left|S^*_{eq,i}\right|\left|Z'_{RR,ii}\right|} = \frac{\left|S_{ac,eq,i}\right|}{\left|S^*_{eq,i}\right|} = \frac{\left|S_{ac,i} - jQ_{c,eq,i}\right|}{\left|S^*_{eq,i}\right|} = 1 \tag{24}$$

where

$$Q_{c,eq,i} = Q_{c,i} + \sum_{j\in \mathbf{R}, j\neq i} \alpha_{ij} Q_{c,j}, \quad \alpha_{ij} = \frac{Z_{RR,ij}}{Z_{RR,ii}} \frac{V_{R,j}}{V_{R,i}} \tag{25}$$

$$S^*_{eq,i} = S^*_{R,i} + \sum_{j\in \mathbf{R}, j\neq i} \beta_{ij} S^*_{R,j}, \quad \beta_{ij} = \frac{Z_{RR,ij}}{Z_{RR,ii}} \left(\frac{V_{R,i}}{V_{R,j}}\right)^* \tag{26}$$

Similar to (14), (24) shows that the voltage stability at bus *i* can be identified by comparing the equivalent complex power injected from the IBR at bus *i* (i.e., $|S^*_{eq,i}|$) with its equivalent short-circuit capacity (i.e., $|S'_{ac,eq,i}|$). The voltage is stable at bus *i* if the equivalent complex power injected from the IBR is larger or equal to equivalent short-circuit capacity.

3.2.2. Proposed Method for Grid Strength Assessment

Based on (24), we define the effective site-dependent SCR (ESDSCR) to quantify the strength of the power grid with multiple IBRs and shunt capacitors from the perspective of static voltage stability. When the injected powers $S_{R,j}$ in (24) is replaced with the injected powers of IBRs, $P_{R,j}$, $j \in \boldsymbol{R}$, the ESDSCR is defined as:

$$ESDSCR_i = \frac{\left|S_{ac,i} - jQ_{c,eq,i}\right|}{\left|P_{R,eq,i}\right|} = \frac{\left|S_{ac,i} - jQ_{c,i} - \sum_{j\in\boldsymbol{R}, j\neq i} \alpha_{ij} jQ_{c,j}\right|}{\left|P_{R,i} + \sum_{j\in\boldsymbol{R}, j\neq i} \beta_{ij} P_{R,j}\right|} \tag{27}$$

The ESDSCR as defined by (27) is the generalized representation of the ESCR in (15). When only one shunt element is connected to one IBR in the power system in (27), $P_{R,j}$ and $Q_{c,j}$ (i.e. the reactive power compensation from the shunt elements) for other IBRs are equal to zero. In this case, the expression as defined in (27) can be reduced to the expression shown in (15).

The ESDSCR considers not only the interactions between IBRs but also the interactions between shunt capacitors in the system. In (27), ESDSCR at bus *i* takes into account the reactive compensation from the shunt capacitor directly connected to bus *i* (i.e., $Q_{c,i}$) and the reactive compensations from the other capacitors at different sites in the system (i.e., $Q_{c,j}$). Especially, the reactive compensations from other different sites, $Q_{c,j}$, is scaled by weight α_{ij} in (25), which shows the effect of the interaction between shunt capacitors at different sites on the grid strength at bus *i*. Also, ESDSCR at bus *i* includes the power injection from IBR directly connected to bus *i* (i.e., $P_{R,i}$) and the combined power injection from the IBRs connected to the other buses in the system

(i.e., $P_{R,j}$). The combined power injection, $P_{R,j}$ is scaled by weight β_{ij} in (26), which reflects the impact of the interaction between IBRs at different sites on the grid strength at bus *i*.

The ESDSCR retains the same physical interpretation as the ESCR as defined in (15). Both ESDSCR and ESCR characterize the grid strength from the perspective of static voltage stability. Thus, the ranges of ESCR for grid strength evaluation can also be applied to ESDSCR. That is, the AC grid is strong at a bus if its ESDSCR is larger than 3; the grid is weak at a bus if its ESDSCR is in the range between 2 and 3; and the grid is very weak at a bus when its ESDSCR value is smaller than 2. Furthermore, according to (24), when ESDSCR is equal to 1, voltage at bus *i* is in its collapse point; when ESDSCR is smaller than 1, voltage becomes unstable.

3.3. Study Results

In this section, the efficacy of the proposed ESDSCR for grid strength assessment is demonstrated on the modified IEEE 39-bus system, as shown in Fig. 54 [25], by comparison with ESCR and modified SDSCR. In the system, machine G1 at bus 39 is selected as the slack machine instead of the original slack machine G2 at bus 31; synchronous generators at buses 31 and 32 are replaced with two wind farms.

First, we determine the Pd,31 – Pd,32 stability boundary of IBRs at buses 31 and 32, as shown in Fig. 55. In this figure, the two curves indicate the stability boundaries when shunt capacitors at buses 31 and 32 are and are not considered. On each boundary curve, all pairs of power injection (Pd,31, Pd,32) correspond to the critical operating conditions: when the power system operates with any pair (Pd,31, Pd,32) outside the boundary, voltage instability will occur in the system; when the system operates with any pair (Pd,31, Pd,32) inside the boundary, system voltage is stable. The stability boundary is now validated using the P–V analysis. It can be observed from Fig. 55 that the stability boundary curve including shunt capacitors is higher than the one

excluding them. This implies that when including shunt capacitors at buses 31 and 32, the stability region increases and thus voltage stability is improved.

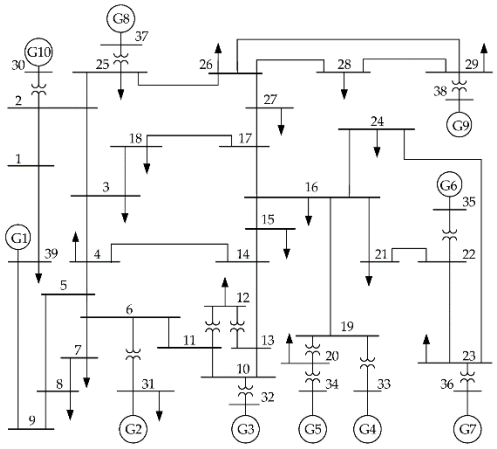

Figure 54. Single-line diagram of the IEEE 39-bus system.

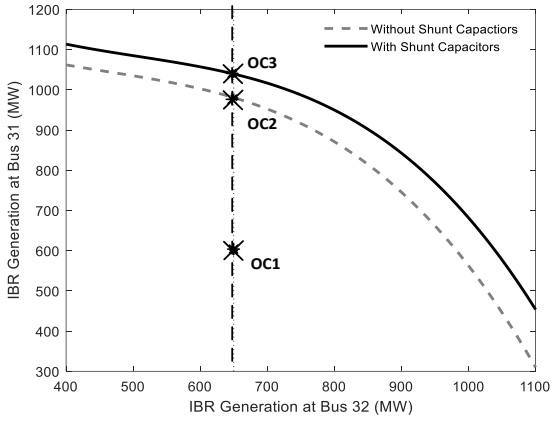

Figure 55. $P_{d,31} - P_{d,32}$ stability boundary of IBRs in the IEEE 39-bus system.

Based on the stability boundaries in Fig. 55, we then verify the efficiency of the proposed ESDSCR and compare it with the ESCR. According to the stability boundaries, a set of operating conditions (OCs) are selected. This set of OCs includes points OC1, OC2, and OC3 as shown in Fig. 55. Under this set of OCs, the voltage stability at buses 31 and 32 are evaluated. The evaluation results are reported in Table 1. Also, we evaluate the ESDSCR and ESCR at buses 31 and 32. These results are presented in Table 2.

Table 1. Voltage Magnitudes at Buses 31 and 32 under Various Operating Conditions.

Operating Condition	Power Injection (*MW*)		Bus Voltage (*p.u.*)	
	Bus 31	Bus 32	Bus 31	Bus 32
OC1	600	650	0.9484	0.9399
OC2	980	650	0.8421	0.8531
OC3	1060	650	0.7111	0.7725

Table 2. Comparison of ESCR and ESDSCR under Various Operating Conditions.

Operating Condition	Power Injection (*MW*)		ESCR		ESDSCR	
	Bus 31	Bus 32	Bus 31	Bus 32	Bus 31	Bus 32
OC1	600	650	3.8244	3.0347	2.5609	2.5043
OC2	980	650	1.7892	2.7202	1.5756	1.7409
OC3	1060	650	1.3021	2.3041	1.0219	1.3259

It can be observed from Table 1 and Table 2 that ESDSCR can effectively evaluate grid strength in terms of voltage stability, but ESCR tends to overestimate grid strength. As shown in Table 1, the voltage magnitudes at both buses 31 and 32 reduce as only Pd,31 is increased. This indicates that the power injection at bus 31 affects not only voltage stability at bus 31 but also the voltage stability at bus 32. Specifically, under OC1, the voltage magnitudes at buses 31 and 32 are |V31|=0.9484 p.u. and |V32|=0.9399 p.u., which are distant from typical voltage security requirement of 0.95 p.u.. It is expected that both ESCR and ESDSCR would identify the system to be weak at buses 31 and 32. In other words, the values of both ESCR and ESDSCR are expected to be smaller than 3 at these two buses. As shown in Table 2, the evaluation results of ESDSCR at buses 31 and 32 are |V31|=2.5609 and |V32|=2.5043, which are smaller than 3; however, the results of ESCR are 3.8244 and 3.0347, which are larger than 3 and indicate the grid is still strong at these two buses. These results show that ESCR has overestimated grid strength at both buses 31 and 32. Moreover, under OC2, the voltage magnitudes at buses 31 and 32 are |V31|=0.8421 p.u. and

|V32|=0.8531 p.u., which are further distant from the required security level of 0.95 p.u. It is expected that the system would be identified to be very weak at the two buses, so both ESCR and ESDSCR values should be smaller than 2. The expected results of ESDSCR are confirmed from data in Table 2, but Table 2 also shows that ESCR at bus 32 is much larger than 2. Thus, ESCR provides overestimated result again. The issue becomes more prominent when the voltage at bus 31 reaches its stability limit under OC3. It is expected that both ESCR and EDSDSCR at bus 31 should be close to 1. As shown in Table 2, the expected result of ESDSCR can be confirmed; however, the evaluation result of ESCR is 1.3021, which is much larger than 1 and indicates the voltage at bus 31 is still distant from its stability limit. Those observations show that ESDSCR can effectively evaluate the grid strength at buses 31 and 32 in terms of voltage stability, but ESCR tends to overestimate the grid strength at buses 31 and 32.

3.4. Summary

In this chapter, we proposed the new method for evaluating the strength of power grids with the high penetration of IBRs taking into account the impact on grid strength from both the interactions between capacitors in the grid and the interactions among IBRs at different sites. Validation and efficacy of the proposed method was shown with numerical simulation case studies on the IEEE 39-bus system. In the future research, we will further verify the proposed method in large-scale power grids under various operating conditions including contingencies.

4. IMPACT OF MOMENTARY CESSATION ON SUB-CYCLE DYNAMICS IN SOLAR PV SYSTEMS

The electric power grid is undergoing a rapid change predominantly driven by high penetration levels of renewable energy resources such as solar. These resources are interfaced with the power grid through power electronic inverters that use control algorithms to define their performance characteristics. As a group, these types of resources are commonly referred to as inverter-based resources (IBRs). Since solid-state switches in the inverters enable fast and programmable control, IBRs can use power electronic controls to change active and reactive current injection, and subsequently active and reactive power output. For these reasons, IBRs have the capability of responding to grid disturbances nearly instantaneously to support grid reliability [26][27].

The increasing penetration of inverter-based resources is also changing grid dynamics and challenging grid planning, operation, and protection. From 2016 to 2018, a series of similar events occurred in the Southern California region of the Western Electricity Coordinating Council footprint: transmission system faults triggered the unintended loss of solar generation over a large geographic area [28]-[30]. One of the major causes for the solar PV tripping in 2017 and 2018 is the sub-cycle overvoltage experienced by solar PV inverter when the transmission grid suffers voltage drop following faults [29][30]. Moreover, the sub-cycle dynamics become more complicated when solar PV inverters use momentary cessation operation mode [29]. This operation mode is one of the grid support functionalities required according to the IEEE 1547-2018 interconnection standard for distributed energy resources [31]. Momentary cessation is a type of inverter response to abnormal grid conditions. More specifically, when the inverter terminal voltage falls below (or exceeds) a certain level, the inverter ceases to output any current, but

attempts to maintain (or quickly regain) phase-locked loop (PLL) synchronization to allow for quick reinjection of current when the voltage recovers to a certain point.

A recent performance guideline for IBRs on the U.S. bulk power system published by the NERC calls for full-ride through without momentary cessation [32][33], though the NERC task force responsible for the guideline recognized that it may not be feasible to eliminate momentary cessation in some existing inverters. In contrast, the IEEE 1547-2018 requires momentary cessation for Category III distribution energy resources (DERs) and allows momentary cessation for Categories I and II DERs [31], so for distribution-connected inverters, momentary cessation is the expected behavior. In addition, the NERC reports in [29][30] highlight the sub-cycle dynamics are still not understood, especially when considering the impact of momentary cessation. This sub-cycle transient is difficult to model and predict during a short time [34].

In this chapter, we investigate the impact of momentary cessation on the sub-cycle dynamics using a RTDS simulator, which is developed by RTDS Technologies Inc to solve the power system equation fast enough to realistically represent conditions in actual power grids [35]. To this end, two solar PV systems with detailed inverter models considering inverter switching dynamics and momentary cessation function are first constructed for real-time electromagnetic simulations. Then, the impact of momentary cessation on sub-cycle dynamics is explored under three cases including the increasing number of solar PV inverters, weak grid operating conditions, and diversity in recovery time of solar PVs. The rest of this chapter is organized as follows. In Section 4.1, the modeling of solar PV systems is introduced. With this modeling, the investigation results of the impact of momentary cessation on the sub-cycle dynamics are presented in Section 4.2. Finally, conclusions are given in Section 4.3.

4.1. Modeling of Solar PV Test Systems

To investigate the impact of momentary cessation on sub-cycle dynamics, two solar PV systems with detailed inverter models considering inverter switching dynamics and momentary cessation function are modeled using the library components of RSCAD [36]. The first test system is a single inverter with a grid-connected PV system where a solar PV is connected to the grid through a grid-following inverter system. The second test system has three PV-inverter systems connected to the grid. Both these two solar PV test systems have detailed modeling of the inverter switching and the control schemes required for the grid connection. Also, both of two test systems can model the operation of inverter momentary cessation.

4.1.1. Solar PV Test System I

The grid-connected PV-inverter test system is modeled and simulated using RSCAD software, which is a real-time simulation environment of RTDS simulator [10]. Fig. 56 shows the single line diagram of the simulated system. The PV-inverter system consists of a PV array that generates 1.75 MW peak power, a dc link capacitor, and a DC/AC inverter with control functions. The PV-inverter system is integrated into the grid through a 6 MVA step-up transformer, and a PI section line connected to a 33 kV grid. The PV-inverter system is connected with a high pass filter at the point of common coupling (PCC).

The PV array is made up of modules connected in both series and parallel, and each module consists of 36 cells in series and 1 in parallel. Each PV array has temperature set to 25°*C* and insolation to 1000 W/m^2 as input. The detailed parameters of the PV array are presented in Table 3. The dc side voltage is 2 kV, and the dc voltage is converted to three-phase 0.48 kV ac voltage through the inverter. Fig. 57 shows the control scheme used in the inverter for the grid-connected PV test system. For the outer loop control, the reference value for the dc bus voltage control (V_{DC}^{*})

is generated through incremental conductance based maximum power point tracking (MPPT) algorithm and PLL based measurements from the grid (V_{PCC}) is used as input for ac bus voltage control. These outer loop voltage controls generate *d-axis* and *q*-axis reference currents for the inner current loop. The inner current loop outputs the modulation index which is later converted into *abc* form using *dq0* to *abc* conversion to input in the firing pulse generators. The generators provide gate signals to the inverter with a switching frequency of 1.8 kHz. The gains used for these control loops are also presented in Table 3. A high pass filter is connected to smoothen the waveforms at the output of the inverter. As shown in Fig. 58, inverter switching is also considered for the grid-connected PV-inverter test system.

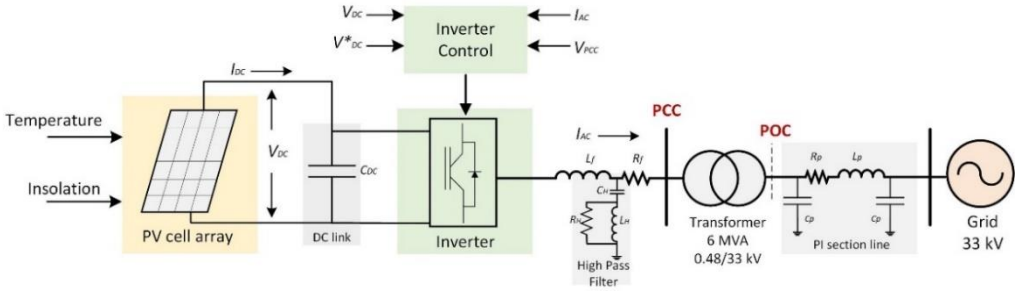

Figure 56. Grid-connected solar PV system with detailed model of inverter.

Table 3. Parameters for the Grid-connected Solar PV System.

Components	Parameters	Values
PV	Number of series cells	36
	Number of paralle strings	1
	Open circuit voltage (V_{oc})	21.7 V
	Short circuit current (I_{sc})	3.35 A
	Number of modules in series	115
	Number of modules in parallel	285
	Voltage at Pmax	17.4 V
	Current at Pmax	3.05 A
DC link capacitor	Capcitance (C_{dc})	0.01925 F
Inverter	Filter resistance	2.38 mΩ
	Filter inductance	200 μH
High pass filter	R_H	0.039 Ω
	L_H	7.874 μH
	C_H	2500 μF
DC bus voltage control	k_{pdc}	0.899
	k_{idc}	0.0585
Current control loop	k_{pi}	0.2
	k_{ii}	0.30675
PLL	k_{pPLL}	5
	k_{iPLL}	0.01
PI section line	R_p	5 Ω
	X_p	5 Ω
	X_{cp}	5 MΩ

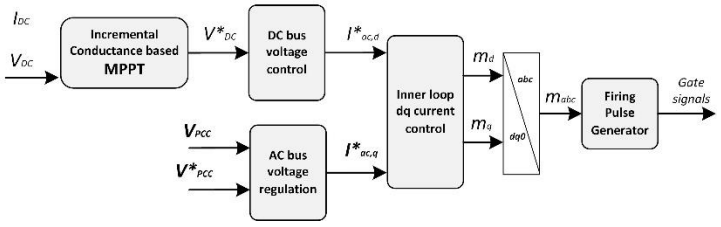

Figure 57. Block diagram for inverter control.

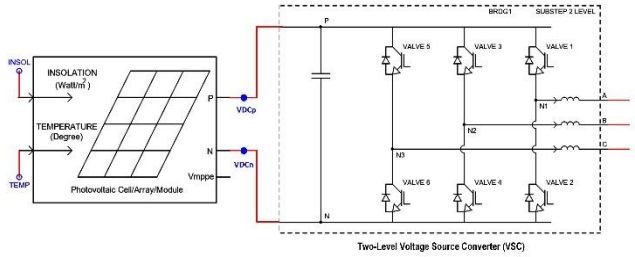

Figure 58. Detailed model of inverter showing IGBT switches.

4.1.2. Solar PV Test System II

Based on the test system I, we further construct the second solar PV test system with multiple solar PVs to investigate the impact of momentary cessation on sub-cycle dynamics when increasing the number of PV inverters. As shown in Fig. 59, the three solar PVs are connected at PCC through three inverters. In this test system, each of these three solar PVs and their inverters have the same PV system parameters and inverter control schemes and gain values as those used in the first test case. The three PV-inverter system is connected to the 33 kV grid via the transformer and PI section line.

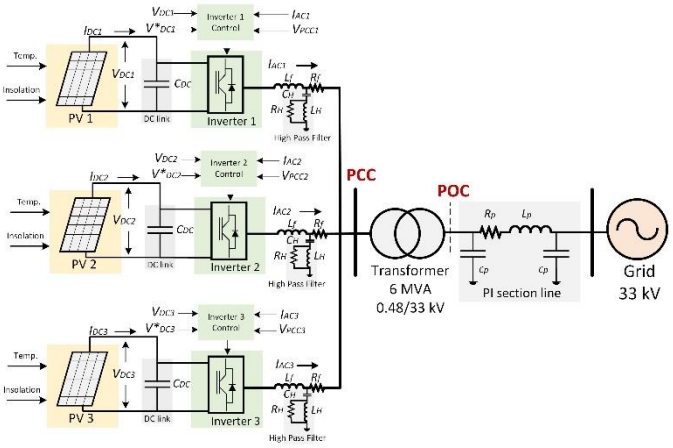

Figure 59. Three grid-connected solar PV inverter systems connected to the grid.

4.1.3. Momentary Cessation

When modeling the two solar PV test systems, we consider the momentary cessation function of PV inverter in response to the low-voltage dynamics. As illustrated in Fig. 60, when the inverter terminal voltage at PCC (V_{PCC}) falls below a certain level (V_{mc}), the inverter ceases to output any current. When the terminal voltage returns to its normal range, current injection resumes after a fixed delay time Δt_{sr}. Ramp rates on recovery may be limited by fixed setpoints in the inverter-level control as indicated over the time interval Δt_{rr} [37].

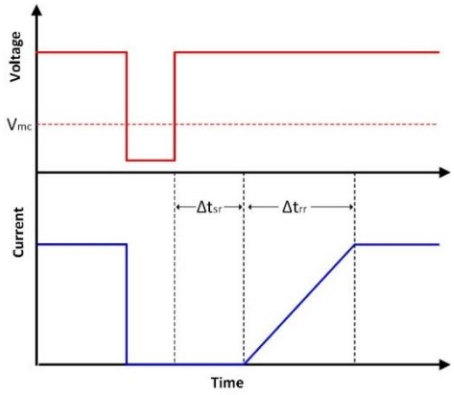

Figure 60. Characteristics of momentary cessation.

It should be noted that momentary cessation is different from inverter tripping. In momentary cessation, the inverters are still connected to the grid, and current injection is restored automatically via the inverter control logic. By contrast, a "tripped" inverter is electrically disconnected from the grid via a contactor or circuit breaker and requires either manual or automatic reset action to restore current injection.

4.2. Study Results

With the two test systems I and II constructed in Section 4.1, the impact of momentary cessation on sub-cycle dynamics is investigated using the RTDS simulator. The following three cases will be considered in our investigation.

4.2.1. Case 1: Increasing the Number of PV Inverters

In this case, both test systems I and II constructed in Section 4.1 are used to investigate the impact of momentary cessation on sub-cycle dynamics when increasing the number of PV inverters. In the two systems, the same fault is applied to the grid side to trigger the momentary cessation operation mode. The fault occurs in the system at t = 0.025s and is cleared after 2.5 cycles. The fault causes the voltage to drop to 0.83 p.u. at the grid bus and immediately triggers the momentary cessation to cease the current injection from the inverter. After the fault is cleared, 2 cycles are delayed (i.e., $\Delta tsr=0.033s$) to restart the current injection from all inverters. During the recovery process, the ramp rate is limited by the time interval $\Delta trr=0.008s$. Fig. 61 and Fig. 62 show the simulation results of per unit (P.U.) and three-phase voltages and currents at PCC in the two systems.

By comparing Fig. 61 with Fig. 62, it can be observed that increasing the number of PV inverters exacerbates the sub-cycle overvoltage and overcurrent. As shown in Fig. 61, when a single PV inverter is considered in the test system I, the peak value of the sub-cycle overvoltage is approximately 1.50 p.u. after ceasing the current injection from the inverter. There are no sub-cycle overvoltage and overcurrent during the recovery process after restarting the current injection from the inverter. However, when three PV inverters are considered in the test system II, Fig. 62 shows the peak value of the sub-cycle overvoltage is approximately increased to 1.91 p.u. after ceasing the current injection from the inverter. Moreover, there are sub-cycle overvoltage and overcurrent during the recovery process after restarting the current injection from the inverter. The peak values of the overvoltage and overcurrent are approximately 1.42 p.u. and 1. 27 p.u.

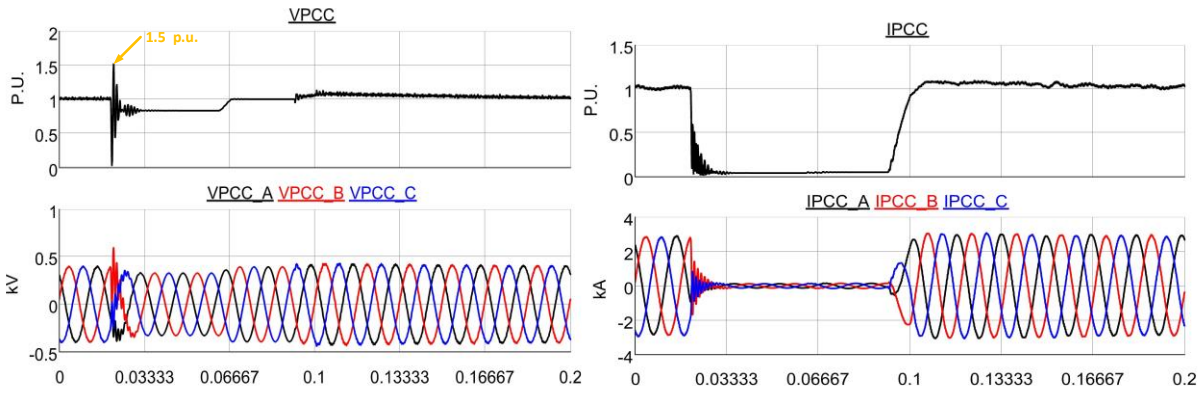

Figure 61. Per-unit and three-phase voltage and current at inverter terminal PCC in test system I after a grid fault is applied and momentary cessation is triggered in case 1.

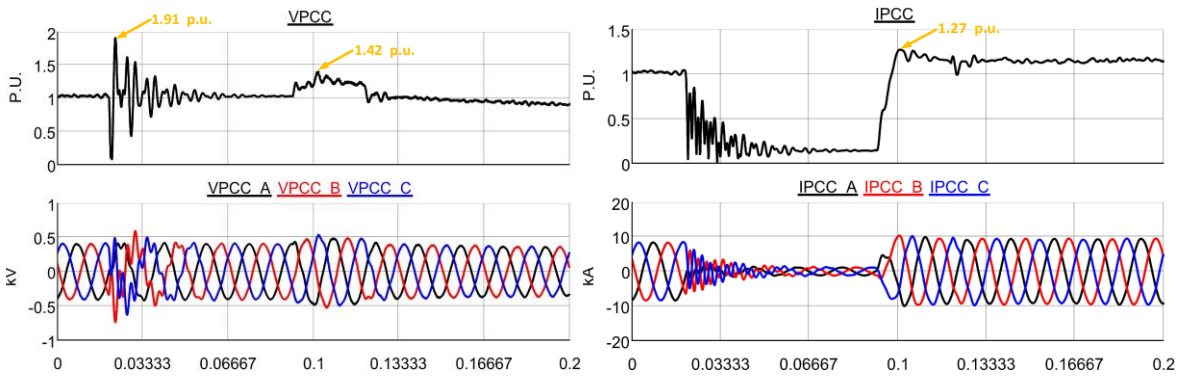

Figure 62. Per-unit and three-phase voltage and current at inverter terminal PCC in test system II after a grid fault is applied and momentary cessation is triggered in case 1.

4.2.2. Case 2: Changing Grid Operating Conditions

In this case, test system II is used to investigate the impact of momentary cessation on sub-cycle dynamics under varying grid operating conditions. Specifically, a weak grid operating condition is considered in the system by increasing the reactance of the line between POC and grid bus to two times larger than the original value. The same fault used in case 1 is applied to the grid side in the system to trigger the momentary cessation operation mode. The same delay time Δtsr and time interval Δtrr are used for setting the momentary cessation function for all inverters. Fig. 63 shows the simulation results of p.u. and three-phase voltages and currents at PCC in the system.

By comparing Fig. 63 with Fig. 62, it can be observed that the sub-cycle overvoltage and overcurrent become exacerbated when the grid becomes weak. As shown in Fig. 63, the peak value of the sub-cycle overvoltage is approximately increased by 2.22 p.u. from 1.91 p.u. (shown in Fig. 62) after ceasing the current injection from the inverter. Furthermore, during the recovery process after restarting the current injection from the inverter, Fig. 63 shows the sub-cycle overvoltage and overcurrent are increased to 1.61 p.u. and 1.35 p.u. from 1.42 p.u. and 1. 27 p.u. (shown in Fig. 62), respectively. Thus, an improved grid strength may reduce the severity of sub-cycle overvoltage and overcurrent induced by inverter momentary cessation.

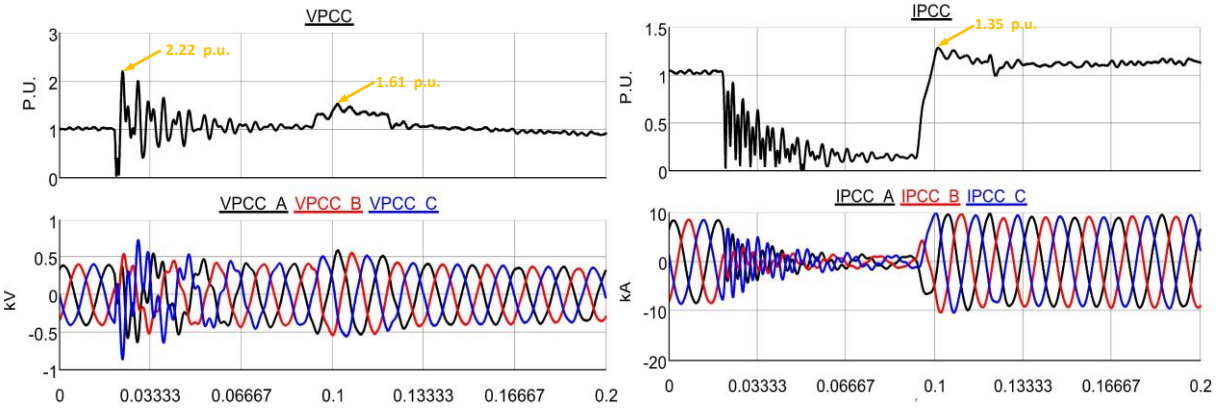

Figure 63. Per-unit and three-phase voltage and current at inverter terminal PCC in test system II under weak grid conditions after a grid fault is applied and momentary cessation is triggered in case 2.

4.2.3. Case 3: Increasing the Diversity in Recovery Time of PV Inverters during Restoration Process

In this case, we further investigate the impact of momentary cessation on sub-cycle dynamics when increasing the diversity of PV inverters during the recovery process after restarting the current injection from all inverters in test system II under the weak grid operating condition. In the system, the weak grid operating condition and the applied fault are the same as those used in case 2. To increase the diversity of PV inverters during the recovery process, three inverters in the system are assigned with different delay times ($\Delta tsr1=0.033s$, $\Delta tsr2=0.066s$, and $\Delta tsr3=0.099s$)

to restart their current injections during the recovery process. Fig. 64 shows the simulation results of p.u. and three-phase voltages and currents at PCC in the system.

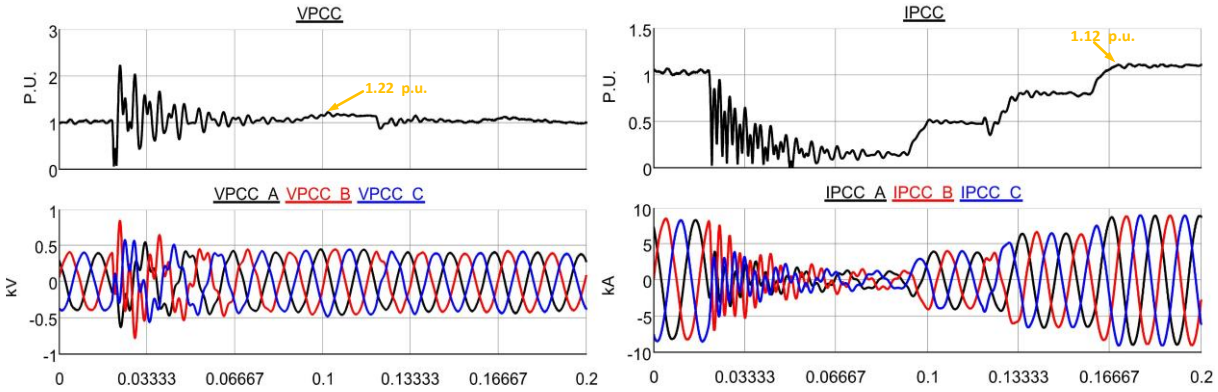

Figure 64. Per-unit and three-phase voltage and current at inverter terminal PCC in test system II under weak grid conditions after a grid fault is applied and momentary cessation is triggered in case 3.

By comparing Fig. 64 with Fig. 63, it can be observed that increasing the diversity of PV inverters can reduce the severity of the sub-cycle overvoltage and overcurrent during the recovery process. As shown in Fig. 64, the peak values of the sub-cycle overvoltage and overcurrent is approximately decreased to 1.22 p.u. and 1. 12 p.u. from 1.61 p.u. and 1.35 p.u. (shown in Fig. 63), respectively, after restarting the current injections from three inverters with different recovery times. Thus, the appropriate coordination of recovery times for PV inverters during the recovery process can improve sub-cycle dynamics stability.

4.3. Summary

In this chapter, we investigated the impact of momentary cessation on sub-cycle transient characteristics using RTDS-based real-time electromagnetic transient simulations with detailed inverter models that consider switching dynamics and momentary cessation operation mode. It is found that undesired sub-cycle overvoltage and overcurrent are induced by momentary cessation. Moreover, the sub-cycle overvoltage and overcurrent become significant when increasing the integration of solar PV inverters into the system. Furthermore, it is found that the grid operating

condition, which is normally considered as the initial or boundary condition of transient in the grid, needs to be further investigated, especially during the system recovery and inverter fault-ride through, where significant voltage sags or swells could be significant [38]. In addition, the overvoltage and overcurrent during the restoration stage of fault-rid through process can be improved when considering the impact of the diversified recovery times for PV inverters to restart current injection.

5. IMPACT OF SOLAR INVERTER DYNAMICS DURING GRID RESTORATION PERIOD ON PROTECTION SCHEMES BASED ON NEGATIVE-SEQUENCE COMPONENTS

The electric power grid is undergoing a rapid change driven by the high penetration of renewable resources such as solar and wind via power electronic inverters. While these inverter-based resources (IBRs) can use power electronic controls to respond to grid disturbances nearly instantaneously and thus support grid reliability, they are challenging grid protection [39][40]. IBRs feature distinct fault responses compared to conventional generators. The response of a synchronous generator to a fault in the power system is determined by the physics of the rotating machine, which is well understood by grid protection engineers. However, the fault response of an IBR is determined by how the inverter control system has been programmed to respond to its terminal conditions. The manner in which the fast-acting controls within the inverter respond to rapidly changing terminal conditions is an engineered feature but not well understood by grid protection engineers [41]. Such IBR fault characteristics fundamentally impact the current practices for applying and setting protective relays to maintain the reliable operation of the power grid dynamically dominated by synchronous generators. For example, solar inverters induce a low magnitude of fault current with insufficient levels of negative and zero sequence currents [42][43]. The negative-sequence fault current contribution of the wind generators can be very small depending on its type and control [44][45]. Thus, protection schemes based on negative sequence components can be affected and experience malfunctions due to the changes in fault characteristics [46][47]. It is crucial to understand how IBRs react to fault conditions, so that proper protection settings can be set to avoid a protection maloperation or a failure in grid operation.

Recently, the North American Electric Reliability Corporation (NERC) has reported a series of events of the unintended loss of solar generation following the grid faults in Southern California region of the Western Electricity Coordinating Council footprint [48]-[51]. These events highlight the importance of understanding the fault responses of solar PVs and their impact on protection schemes during the system restoration period after grid faults are cleared. In the literature, these events have been recently investigated by studying the impact of IBR fault responses on the grid operation using generic positive sequence dynamic stability simulations [52]-[62]. However, the existing works do not investigate the solar PV responses and their impacts on protection schemes when the grid is recovering after the disturbances are cleared. Moreover, these existing works usually use positive sequence stability models and simple inverter modeling for simulation analysis. Such models may not be used in electromagnetic transient simulations for modeling intricate details for different inverter controls and accurately evaluating the IBRs' response during abnormal events. For example, the inverter dynamics during the restoration period can be affected by blocking and de-blocking functions in response to the low-voltage dynamics during fault conditions [64][65].

In this chapter, we investigate the solar inverter dynamics with a focus on negative sequence quantities during the grid restoration period and their impact on protection schemes based on a real-time digital simulator (RTDS), which is developed by RTDS Technologies Inc. to solve the power system equation fast enough to realistically represent conditions in actual power grids [63]. To this end, we first construct the modeling of two solar PV test systems with detailed inverter models including inverter switching dynamics as well as inverter blocking and deblocking functions for the RTDS simulation. Then, we identify the key differences in negative-sequence quantities between solar farms and synchronous generators during the restoration period following

a grid disturbance. On this basis, we further analyze negative-sequence current characteristics of the solar inverter during the grid restoration period and discuss the negative impact of the negative-sequence current of solar inverters on the performance of typical protection schemes based on negative sequence quantities. The major contributions of this chapter include:

1. Identify the key differences in negative-sequence quantities between solar inverters and synchronous generators during the restoration period following a grid disturbance;
2. Investigate the negative-sequence current characteristics of solar inverters during the grid restoration period; and
3. Analyze the negative impact of the negative-sequence current of solar inverters during the restoration period on the performance of typical protection schemes using a hardware-in-loop simulation based on the RTDS.

The rest of this chapter is organized as follows. Section 5.1 presents the methodology for the chapter. Section 5.2 presents the solar PV test systems created for RTDS simulation. Section 5.3 identifies the key differences in negative-sequence quantities between solar inverters and synchronous generators during the grid restoration period. Section 5.4 analyzes the negative-sequence current characteristics of the solar inverters during the grid restoration period. Section 5.5 investigates the interaction between the negative-sequence current of solar inverters and protection schemes based on negative sequence components. This chapter is concluded in Section 5.6.

5.1. Methodology

The hardware-in-loop simulation platform is illustrated in Fig. 65, where the RTDS is linked to a physical relay from the Schweitzer Engineering Laboratories (SEL). The relay has a negative-sequence overcurrent element and can use built-in metering functions to analyze event

reports for rapid commissioning, testing, and post-fault diagnostics. The simulation model of a solar PV power system is created on a guest computer using the RSCAD software. Then, this software compiles and loads this model into the RTDS for real-time simulations. The digital output signals of the current and voltage simulated by the RTDS are converted into analog signals by the Giga-Transceiver Analog Output (GTAO) card and are then fed into the relay. The relay has a low-level interface, which allows them to directly receive the converted analog signals without the need for the voltage/current amplifier. The dry contacts of the relay are connected to the low-voltage panel of the RTDS to send the digital tripping signals from the relays to the RTDS via the input channels on its front lower voltage panel. As soon as the relay trips, it is detected by the digital input of the RTDS, which opens the breaker in the model being simulated in real time and sends the updated signals to the RTDS for real-time simulation. The updated simulation results can be monitored by RSCAD software.

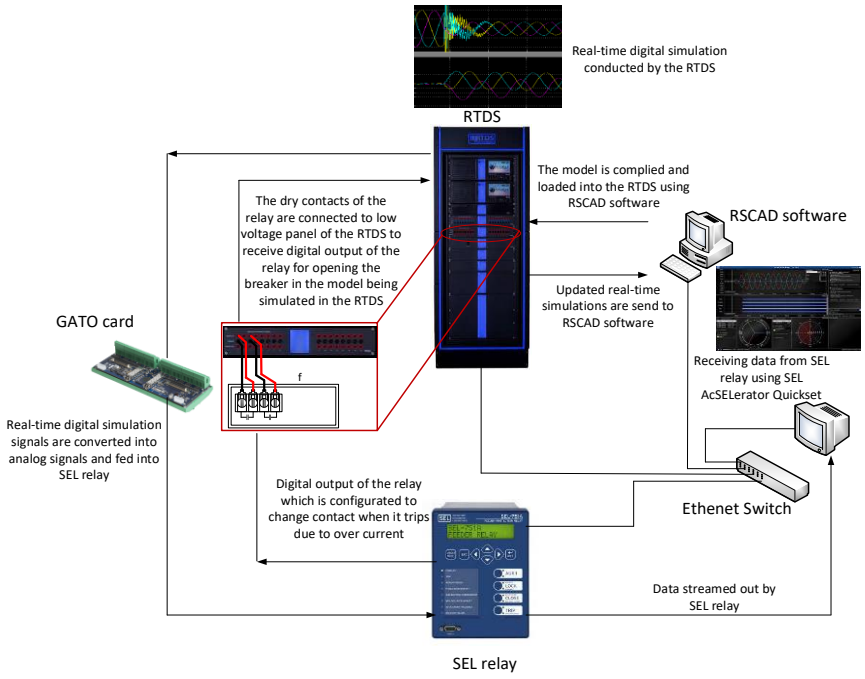

Figure 65. Illustration of the hardware-in-loop simulation platform used for testing the relay performance under solar generation.

5.2. Modeling of Solar PV Test Systems

To investigate the impact of solar inverter dynamics during the grid restoration period on protection schemes, we use the library components of RSCAD software [66] to construct two grid-connected solar PV systems with detailed inverter models considering inverter switching dynamics and complicated inverter control functions required for the grid connection. RSCAD is a real-time simulation environment used with the RTDS.

5.2.1. Solar PV Test System I

As illustrated in Fig. 66, the grid-connected solar PV system I includes the grid side and solar inverter side. At the grid side, the 35 kV point of connection (POC) is connected to the 200 MVA main power transformer interfacing with the grid through the transmission line and step-up substation. The system transformer steps down the transmission voltage (i.e. 500 kV) to a medium voltage level (i.e., 35 kV). The transmission line also features a 225 MVAR shunt reactor acting as a reactive compensation device. The substation consists of two 1200 MVA main power transformers. The reactive compensation device and parameters for the transmission line and transformers are modeled to simulate a realistic environment that matches a system seen in the real-world to provide convincing and credible results. The grid is modeled as a standard voltage source with an impedance to account for a synchronous generator. Table 4 presents the component parameters for the grid side in this solar PV test system.

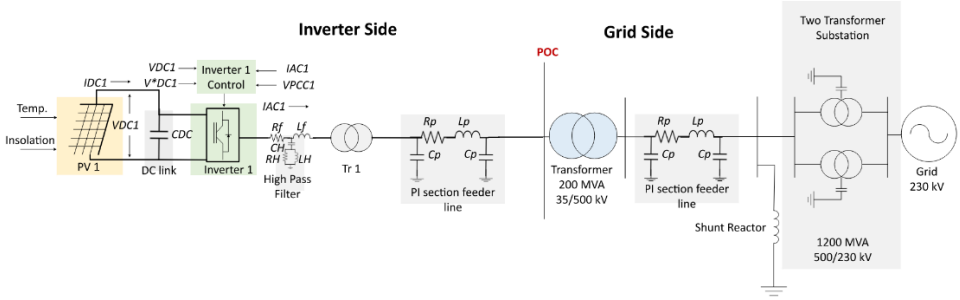

Figure 66. Solar PV test system I.

Table 4. Parameters for the Grid-connected Solar PV System.

Components	Parameters	Values
Step-down Substation	High Voltage	500 kV
	Low Voltage	35 kV
	Transformer Rating	200 MVA
	Shunt reactor rating	498 MVAR
Transmission Line	Resistance	3.80 Ω
	Inductance	0.202 H
	Capacitance	2.92 Mf
	Line Length	226 km
	Tertiary Cap Bank Capacitance	138 μF
Step-up Substation	High Voltage	500 kV
	Low Voltage	230 kV
	Tertiary Voltage	48 kV
	Transformer Rating	1200 MVA
	Series Resistance	0.84 Ω
	Parallel Resistance	120.14 Ω
Generation	Parallel Inductance	0.0322 H
	Voltage (L-L, RMS)	230 kV
	Real Power	1600 MW
	Reactive Power	73 MVAR

At inverter side, a single solar PV inverter is connected to the transmission POC bus through a 3 MVA step-up transformer (Tr 1 shown in Fig. 66) and a PI-section feeder line. This transformer has a scaling function that scales the current as it steps up the voltage to increase the power output of the solar farm from 1.75 MW to 70 MW. As illustrated in Fig. 67, the solar PV consists of a PV array that generates 1.75 MW peak power, a DC-link capacitor to stabilize the voltage, and a DC/AC inverter with control functions. Fig. 67 also shows the solar PV inverter, which is modeled by a two-level voltage source converter (VSC) and a DC-link capacitor. Each of the six switches in the VSC connects one of the three phases to one of the DC terminals. The switches in each leg are switched alternatively using the sinusoidal pulse width modulation technique, where the sinusoidal reference signal is compared with a fixed frequency triangular

waveform to create this switching pattern. The detailed inverter model also houses an AC reactor used to filter any undesired harmonics in the system. A snubber circuit is modeled inside of the inverter model, which limits the switching voltage amplitude and its rise rate and reduces power dissipation from the inverter. The snubber circuit consists of a series capacitor and a series resistor connected with a thyristor in parallel. On the AC side terminals of the inverter, there is a high-pass RC filter capable of filtering out transients from both the grid and the inverter AC side terminals. The parameters for the solar PV array and the inverter are shown in Table 5.

As shown in Fig. 68, the solar PV inverter has generic control schemes as well as blocking and de-blocking functions. For the outer loop control, the reference value for the DC bus voltage control (V^*_{DC}) is generated through incremental conductance-based maximum power point tracking (MPPT) algorithm, and phase-locked loop (PLL) based measurements from the grid is used as input for the AC bus voltage control. These outer loop voltage controls generate *d*-axis and *q*-axis reference currents for the inner current loop. The inner current loop outputs the modulation index, which is later converted into *abc* form using *dq0* to *abc* conversion to input into the firing pulse generators. The generators provide gate signals to the inverter with a switching frequency of 2 kHz. In addition, the detailed inverter model includes blocking and de-blocking functions in response to the low-voltage dynamics during fault conditions. Inverter blocking is the function that the inverter is connected to the grid but ceases to output any current when the inverter terminal voltage at the point of common coupling falls below a certain level; inverter de-blocking is the function that inverter reinjects current after a reset delay time when the terminal voltage returns to a nominal value. The fixed time delay is set so that when the current starts to reinject into the system, the system should mostly be back to stability [67].

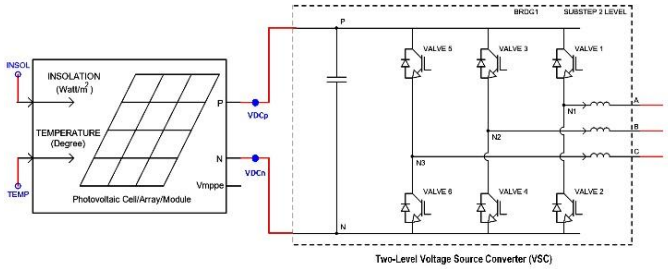

Figure 67. Solar PV array with inverter IGBT switches.

Table 5. Solar Farm Parameters.

Components	Parameters	Values
PV	Number of series cells	36
	Number of paralle strings	1
	Open circuit voltage	21.7 V
	Short circuit current	3.35 A
	Number of modules in series	115
	Number of modules in parallel	285
	Voltage at Pmax	17.4 V
	Current at Pmax	3.05 A
DC link capacitor	Capacitance	0.01925 F
Inverter	Snubber series capacitance	5 μF
	Subber series resistance	800 Ω
	AC reactor resistance	1 μΩ
	AC reactor inductance	80 μH
High pass filter	Resistance	0.039 Ω
	Capacitance	7.874 μF

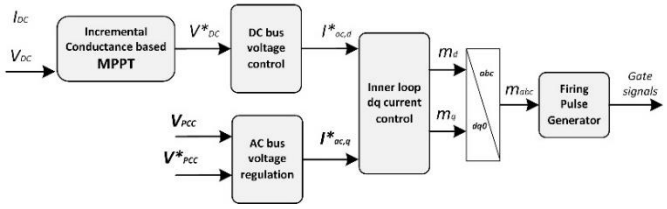

Figure 68. Inverter control system.

5.2.2. Solar PV Test System II

Based on the solar PV test system I, the solar PV system II is further created to investigate the impact of solar inverter dynamics during the grid restoration period on protection schemes

when increasing the number of solar PV inverters. As shown in Fig. 69, the solar PV test system II has three solar PV inverters connected to the grid. In this solar PV system, each of these three solar PVs and their inverters have the same PV system parameters and inverter control system and gain values as those used in the solar PV system I. Each solar facility has its own step-up transformer as well as its own PI section feeder line to characterize the feeder cables and transformers in a real-world solar farm. The feeder cables are then connected together at the low side of the step-up substation, which feeds solar power into the grid via the 35 kV point of connection (POC) connected to the 200 MVA main power transformer, the transmission line, and step-up substation. These 200 MVA main power transformer, the transmission line, and step-up substation have the same parameters as those used in the solar PV test system I. It is worth noting that the maximum power output of the solar generation facility is now three times larger than that in the solar PV system I.

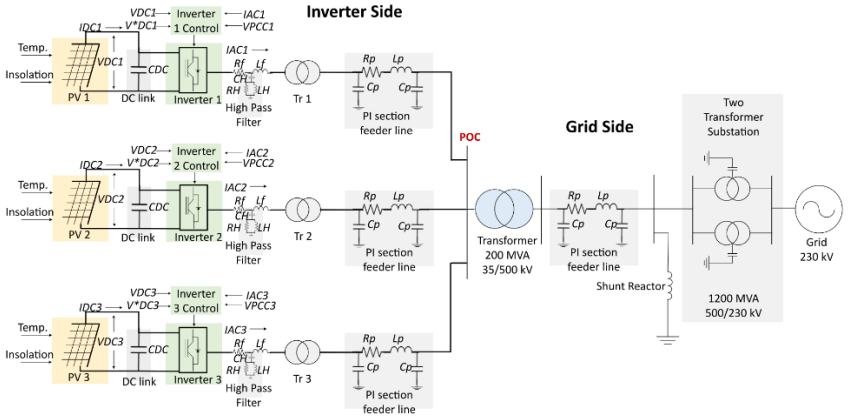

Figure 69. Solar PV test system II.

5.3. Negative-sequence Current of Solar Inverters versus Synchronous Generators during Grid Restoration Period

To illustrate the difference in the negative-sequence current characteristics between solar inverters and synchronous generators during the restoration period following a grid disturbance,

let us consider the solar PV test system I as shown in Fig. 66. In this test system, a balanced three-phase fault is applied to the grid side at t = 6.12s and then cleared after 3 cycles. This fault causes the voltage to drop to 0.5 p.u. at the grid bus and immediately triggers the solar PV inverter blocking function to cease the current injection from the inverter. After the fault is cleared, 2 cycles are delayed to restart the current injection from the solar inverter. Fig. 70 shows the magnitude of the negative-sequence voltage and current magnitudes measured at POC bus in the time domain. To show the negative-sequence current characteristics of synchronous generators under the same fault, we replace the solar inverter in the test system I with a synchronous generator. Fig. 71 shows the magnitude of the negative-sequence voltage and current magnitudes measured at POC bus in the time domain. The data of negative-sequence voltage and current are fundamental frequency values, which are resistant to harmonic content, and are used for relay operation. Fig. 72 and Fig. 73 show the angular differences between the negative-sequence current and voltage for the solar inverter and the synchronous generator.

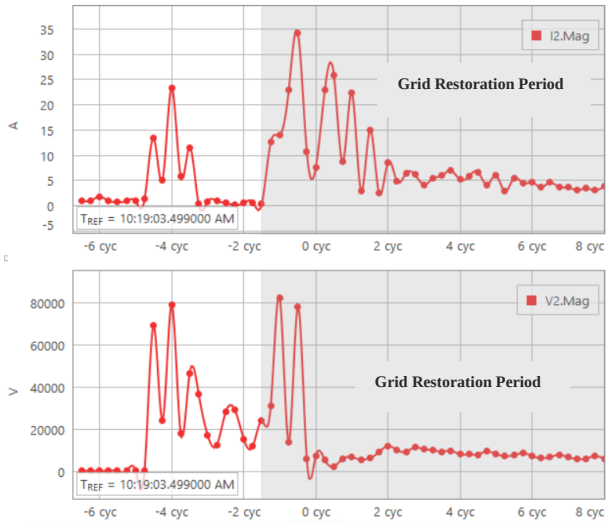

Figure 70. Negative-sequence current and voltage magnitudes measured at POC bus in the solar PV system I following a three-phase fault.

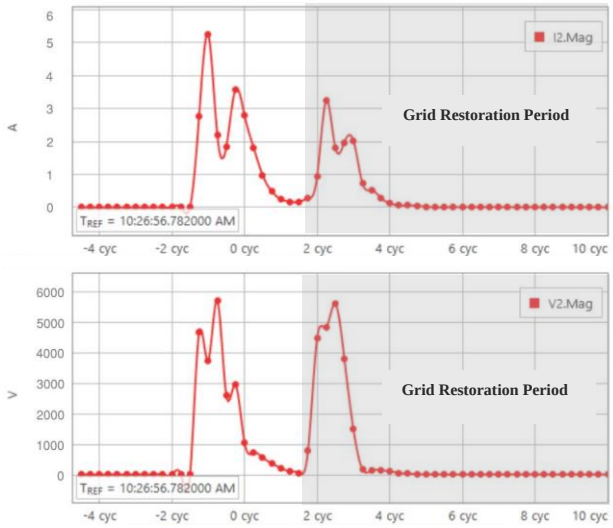

Figure 71. Negative-sequence current and voltage magnitudes measured at POC bus in the solar PV system I following a three-phase fault when the solar inverter is replaced with a synchronous generator.

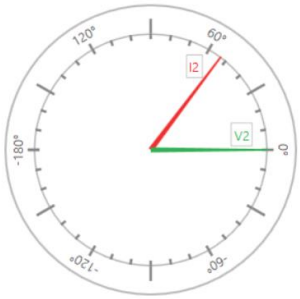

Figure 72. Angular difference between the negative-sequence current and voltage for the solar inverter.

Figure 73. Angular difference between the negative-sequence current and voltage for the synchronous generator.

Comparison of Fig. 70 and Fig. 71, as well as looking at Fig. 72 and Fig. 73, reveals key differences between the negative-sequence current characteristics of the solar inverter and synchronous generator during the grid restoration period:

1. Unlike the conventional synchronous generator, the solar inverter has a relatively high magnitude of negative sequence current during the grid restoration period after the fault is cleared. More specifically, during the grid restoration period, the peak value of the negative-sequence current magnitude from the solar inverter is approximately 35 amps and maintained for about 3.5 cycles; on the other hand, the peak value of the negative-sequence current magnitude from the synchronous generator is just close to 3 amps.
2. The difference between the phase angle of negative-sequence voltage and current phasors from the solar inverter is -53 degrees with the voltage lagging the current. This means the solar inverter acted as a source during the grid restoration period to inject negative-sequence current into the grid. By contrast, the synchronous generator has a phase angle difference between the negative sequence voltage and current of 105 degrees with the voltage leading the current, which means the synchronous generator behaves as a load during the grid restoration period to absorb the negative-sequence current from the grid.

It should be noted that the three-phase fault at the grid bus causes a very high negative-sequence current from the solar inverter during the grid restoration period after the fault is cleared. This is different than what was anticipated since a three-phase fault is a balanced fault type and would not be expected to produce negative-sequence currents or unbalanced currents. Moreover, the high negative-sequence current is induced after the fault is cleared. The negative-sequence current is of particular importance for negative-sequence-based protection elements. Traditionally, these protection schemes have been designed assuming that negative-sequence quantities are

present at significant levels during unbalanced fault conditions. We will discuss the impact of the negative-sequence current of solar inverters on the negative-sequence-based protection schemes in Section 5.5.

5.4. Characteristic Analysis of Negative-sequence Current Injected from Solar Inverters during Grid Restoration Period

The previous section discusses the key differences in the negative-sequence current characteristics between solar inverters and synchronous generators during the restoration period following a grid disturbance. In this section, we will further investigate the characteristics of the negative-sequence current of solar inverters using the RTDS simulator with the two solar PV test systems described in Section 5.2.

5.4.1. Impact of Solar Inverter Number

To investigate the impact of solar inverter number on the negative-sequence current of solar inverters, solar PV test systems II constructed in Section 5.2 is used for RTDS simulation. The same three-phase fault used in Section 5.3 is applied to the grid side in this test system. Fig. 74 shows the negative-sequence current measured at POC bus in the solar PV system II following a three-phase fault.

By comparing Fig. 70 with Fig. 74, it can be observed that the magnitude of the negative-sequence current during the restoration period is increased with the number of solar PV inverters. As shown in Fig. 70, the peak value of the negative-sequence magnitude during the restoration period is 35 amps, but Fig. 74 shows that the peak value of the negative-sequence current magnitude reaches 100 amps, which is almost 3 times higher than 35 amps as shown in Fig. 70. The interaction between additional inverters and the power network in the solar PV test system II

causes the increasing peak value of the negative-sequence current magnitude during the restoration period following a grid disturbance.

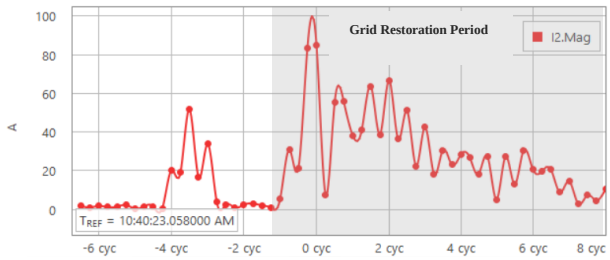

Figure 74. Negative-sequence current magnitude measured at POC bus in the solar PV system II following a three-phase fault.

5.4.2. Impact of Grid Strength

To understand the impact of grid strength on negative-sequence current of solar inverters during the restoration period, we consider a weak grid operating condition in the solar PV test system II by increasing the impedance of the transmission line between POC and grid bus to three times larger than the original value. In the solar PV test system II under the weak grid condition, the same three-phase fault used in Section 5.3 is applied to the grid side. Fig. 75 shows negative-sequence current measured at POC bus in the solar PV system II under the weak grid condition following a three-phase fault.

By comparing Fig. 74 with Fig. 75, it can be observed that when the grid becomes weak, the peak value of the negative-sequence current magnitude increases during the grid recovery period after reinjecting the current from the solar inverters. As shown in Fig. 74, the peak value of the negative-sequence current magnitude stays at 100 amps, while in Fig. 75 the negative-sequence current magnitude is peaked at 140 amps. The comparison results imply that an improved grid strength may reduce the severity of the negative-sequence current during the recovery period.

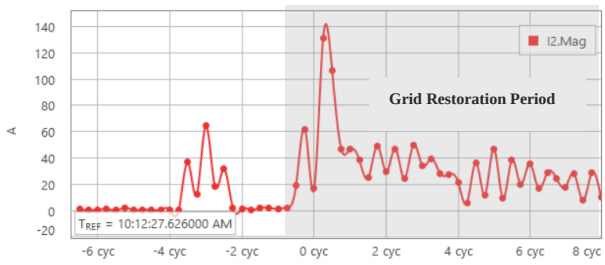

Figure 75. Negative-sequence current magnitude measured at POC bus in the solar PV system II under weak grid conditions following a three-phase fault.

5.4.3. Impact of Fault Types

Finally, we investigate how different types of faults at the grid side affect the negative-sequence current of solar inverters during the grid restoration period in solar PV test system II under weak grid conditions. To this end, we compare the negative-sequence current induced by the three-phase fault at the grid side (as shown in Fig. 75) with those induced by different unbalanced faults, including the single line-to-ground fault, the double line-to-ground fault, and the line-to-line fault. Similar to the implementation of the three-phase fault at the grid side in previous subsections, each of these unbalanced faults is applied to the grid side at t= 6.12s and is cleared after 3 cycles. Also, each of these unbalanced faults will trigger the inverter blocking function to cease the current injection from the inverter; after the fault is cleared, 2 cycles are delayed to restart the current injection from all inverters. Fig. 76–Fig. 78 show negative-sequence current measured at POC bus in the solar PV system II under weak grid condition following different types of unbalanced faults.

By comparing Fig. 75 with Fig. 76–Fig. 78, it can be observed that the single line-to-ground fault causes the most severe negative-sequence current during the grid restoration period than the other types of faults. As shown in Fig. 76, the single line-to-ground fault causes the negative-sequence current magnitude during the grid restoration period to peak around 180 amps, which is higher than 140 amps induced by the three-phase fault as shown in Fig. 75, 170 amps induced by

the double line-to-ground fault shown in Fig. 77, or 160 amps induced by the line-to-line fault as shown in Fig. 78.

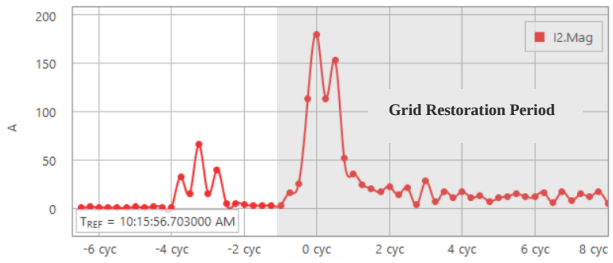

Figure 76. Negative-sequence current magnitude measured at POC bus in the solar PV system II under weak grid conditions following a single line-to-ground fault.

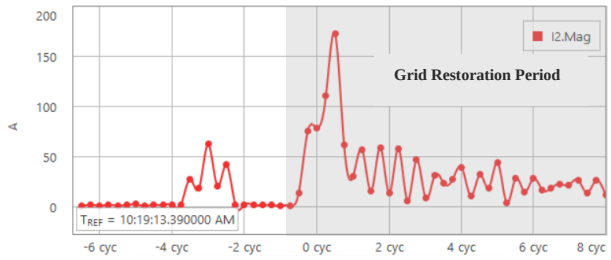

Figure 77. Negative-sequence current magnitude measured at POC bus in the solar PV system II under weak grid conditions following a double line-to-ground fault.

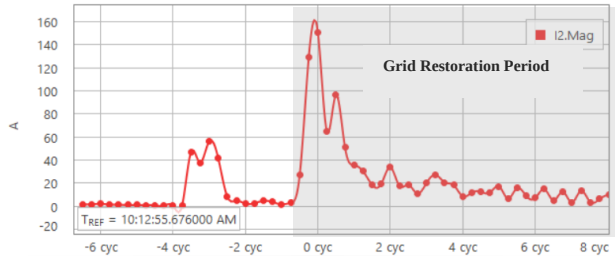

Figure 78. Negative-sequence current magnitude measured at POC bus in the solar PV system II under weak grid conditions following a line-to-line fault.

5.5. Impact of Negative-sequence Current from Solar Inverters during Grid Restoration Period on Negative-sequence Quantities Based Protection Schemes

Section 5.4 has shown the negative-sequence current contribution from solar inverters during the restoration period following grid disturbances. This negative-sequence current is dependent on different operating conditions such as the number of inverters in service, grid

strength, and fault types. This section will discuss how the negative-sequence current negatively affect the performance of the protective relaying functions that are based on negative-sequence quantities, including instantaneous negative-sequence overcurrent (50Q) [68] and directional negative-sequence overcurrent (67Q) [69]. Also, this section will demonstrate such relay maloperations using a hardware-in-loop simulation platform.

5.5.1. Maloperation of Instantaneous Negative-sequence Overcurrent (50Q)

The 50Q element operates when the magnitude of the negative-sequence current exceeds a pre-specified threshold. This threshold is commonly referred to as the pickup setting and specified by the protection engineer based on protection studies. The successful operation of 50Q element relies on the assumption of negative-sequence current being present in substantial levels during a non-symmetrical fault. When the source behind the 50Q element is a synchronous generator, the magnitude of the negative-sequence current is typically large enough to exceed the pickup setting of 50Q element. Therefore, these elements should assert. Nevertheless, due to the high magnitude of the negative-sequence current injection from solar inverters during the grid restoration period, the negative-sequence current may be also larger than the 50Q pickup threshold, and the element may mistakenly operate during the grid restoration period, eve after the grid disturbance is cleared.

To illustrate this maloperation, let us consider the response of the 50Q element of the SEL relay on POC bus to different types of faults applied to the grid side in the solar PV test system II, as described in Section 5.2. The faults include the three-phase fault, the single line-to-ground fault, the double line-to-ground fault, and the line-to-line fault. Each of these faults is applied to the grid side at t= 6.12s and is cleared after 3 cycles in this test system. Each of these faults will trigger the inverter blocking function to cease the current injection from the inverter;

after the fault is cleared, 2 cycles are delayed to restart the current injection from all inverters. Table A1 in Appendix A presents the settings of 50Q. The negative-sequence pick-up current I_{2pkp} has been set at 80 amps, which is roughly 40% of the nominal current. This is a worst case setting since the industry typically recommends 4-40% of the rated current. The element picks up when it sees a negative-sequence fault current with an amplitude more than the pickup setting of 80 amps.

Fig. 79 – Fig. 82 show the amplitude of the negative-sequence fault current measured by the SEL relay and the 50Q trip signals measured at POC bus in the solar PV system II under weak grid conditions following the different types of faults. As shown in the figures, the measured negative-sequence fault current is 135 amps under the three-phase fault, 165 amps under the single line-to-ground fault, 110 amps under the double line-to-ground fault, and 155 amps under the line-to-line fault, respectively. Under each type of fault, the amplitude of the negative-sequence current injected from the solar inverters during the grid restoration period is larger than the negative-sequence pickup current I_{2pkp}, and 50Q element picks up successfully. This example suggests that solar inverters adversely impact the operation of the 50Q element during the grid restoration period, after the fault is cleared at the grid side. Given that 50Q element are commonly used in conjunction with other protective elements such as in a fault detector scheme supervising directional negative-sequence elements [68], time overcurrent relays, and distance relays which use negative-sequence current for remote backup protection [70]. Maloperation of these elements may pose a risk to the reliability of the power system.

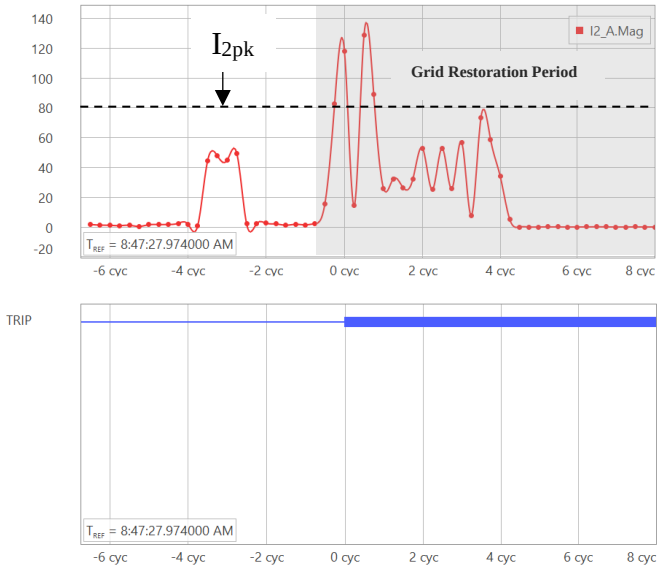

Figure 79. Negative-sequence current magnitude and relay trip signal for 50Q element measured at POC bus in the solar PV test system II under weak grid conditions following a three-phase fault.

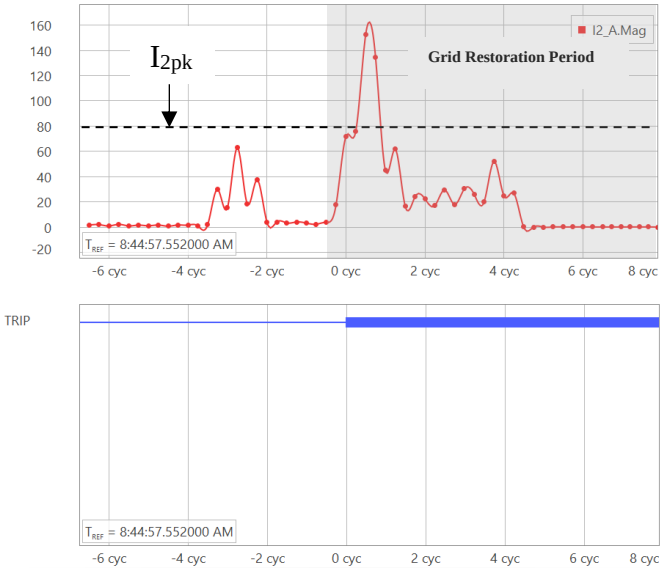

Figure 80. Negative-sequence current magnitude and relay trip signal for 50Q element measured at POC bus in the solar PV test system II under weak grid conditions following a single line-to-ground fault.

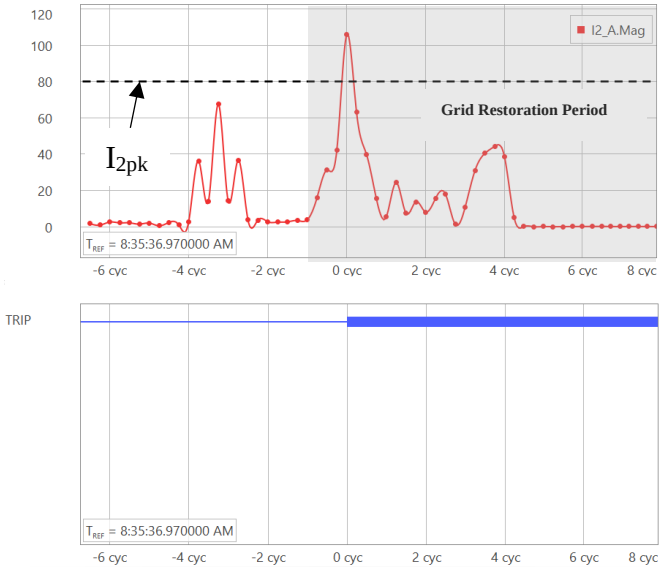

Figure 81. Negative-sequence current magnitude and relay trip signal for 50Q element measured at POC bus in the solar PV test system II under weak grid conditions following a double line-to-ground fault.

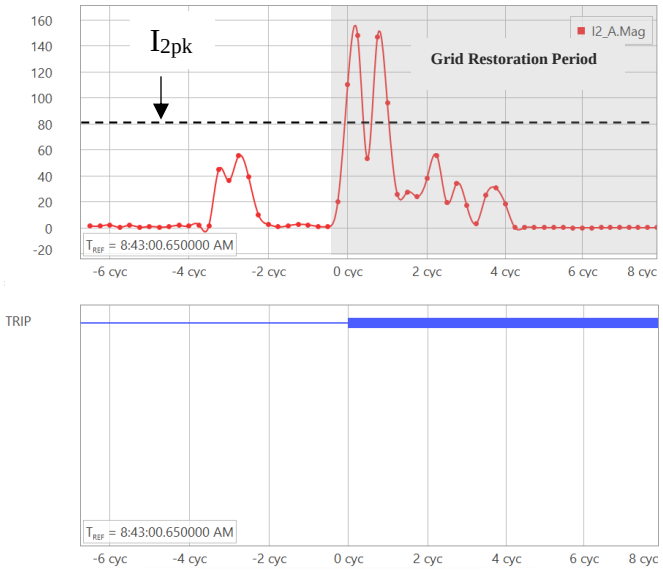

Figure 82. Negative-sequence current magnitude and relay trip signal for 50Q element measured at POC bus in the solar PV test system II under weak grid conditions following a line-to-line fault.

5.5.2. Maloperation of Directional Negative-sequence Overcurrent (67Q)

The 67Q element determines the direction of a fault (forward or reverse to the relay) by measuring the phase angle difference between the negative-sequence voltage and current phasors. Fig. 83 shows a typical implementation and operating principle of the 67Q element [46]. The concept is that a forward or reverse fault causes a phase angle difference of -90°/90° between the negative-sequence voltage and current phasors. This assumption is based on the highly inductive nature of the negative-sequence network in a synchronous generator dominated grid. The 67Q element classifies a fault as forward if the measured phase angle of negative-sequence current lags the polarizing negative-sequence voltage between 0 and 180 degrees. The 67Q element classifies a fault as reverse otherwise. This assumption potentially causes the maloperation of the 67Q element under solar inverters during the grid restoration period.

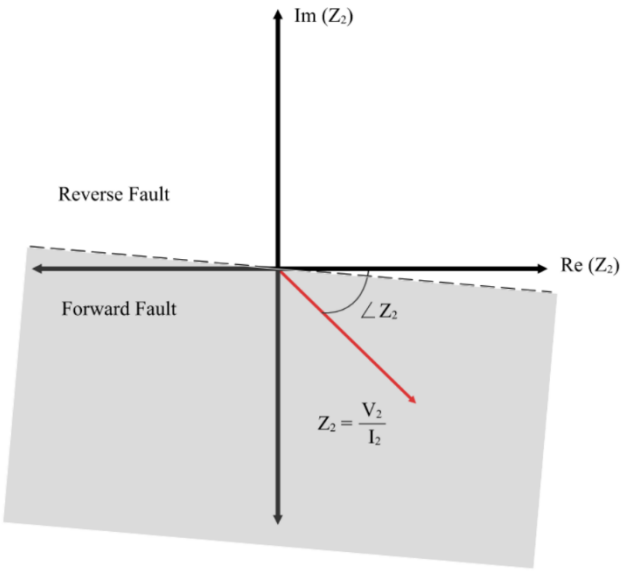

Figure 83. Basic operating principle of 67Q element.

To show this maloperation, let us consider the response of the 67Q element of the relay on POC bus to different types of faults applied to the grid side in the solar PV test system II, as

described in Section 5.2. Similar to the previous case, the faults include the three-phase fault, the single line-to-ground fault, the double line-to-ground fault, and the line-to-line fault; each of these faults is applied to the grid side at t=6.12s and is cleared after 3 cycles in the test system. The faults can be considered to be in the reverse direction since they are coming from the grid. Each of these faults will trigger the inverter blocking function to cease the current injection from the inverter; after the fault is cleared, 2 cycles are delayed to restart the current injection from all inverters. The 67Q element supervises both the phase and the negative-sequence overcurrent elements. There are five settings required to fully implement the negative-sequence impedance directional element. The first two settings are Z_{2F} and Z_{2R}, which are the forward and reverse negative-sequence impedance settings, and they determine the direction of the fault. The next two settings are the forward and reverse fault detectors, which are 50QF and 50QR, and they determine whether a fault has occurred. The final setting is a2, which is the positive-sequence restraint factor, and it supervises the directional element so that it trips only in instances of a fault. Table A1 in Appendix A presents the settings of 67Q.

Fig. 84 – Fig. 87 shows the oscillography data and the response of 67Q element for the different types of faults. The phase angle has been measured at 100 ms into the fault, I_2 and V_2 stand for the amplitudes of the negative-sequence current and voltage, and Z_{2F} and Z_{2R} represent the forward and reverse direction signals, respectively. As shown in Fig. 84, under the three-phase fault, the relay sees a phase angle difference of approximately 19 degrees with V_2 leading I_2, the equivalent negative-sequence impedance vector falls within the forward zone of the impedance plane, and the relay mistakenly issues Z_{2F} declaring forward direction during the restoration period after the fault at the grid side is cleared. The operation is also successful under the other three types of faults as shown in Fig. 85 – Fig. 87, where the apparent V_2 lags I_2 by about -35 degree for the

single line-to-ground fault, the apparent V_2 leads I_2 by about 44 degree for the double line-to-ground fault, and the apparent V_2 lags I_2 by about -20 degree for the line-to-line fault. Under each type of these faults, the element mistakenly declares fault direction and operates this relay.

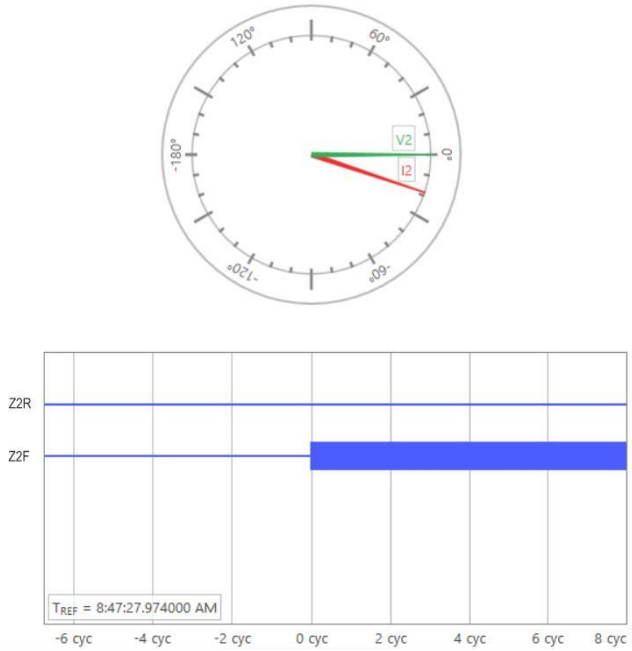

Figure 84. Negative-sequence current and voltage phasors and relay trip signal for 67Q element measured at POC bus in the solar PV system II under weak grid conditions following a three-phase fault.

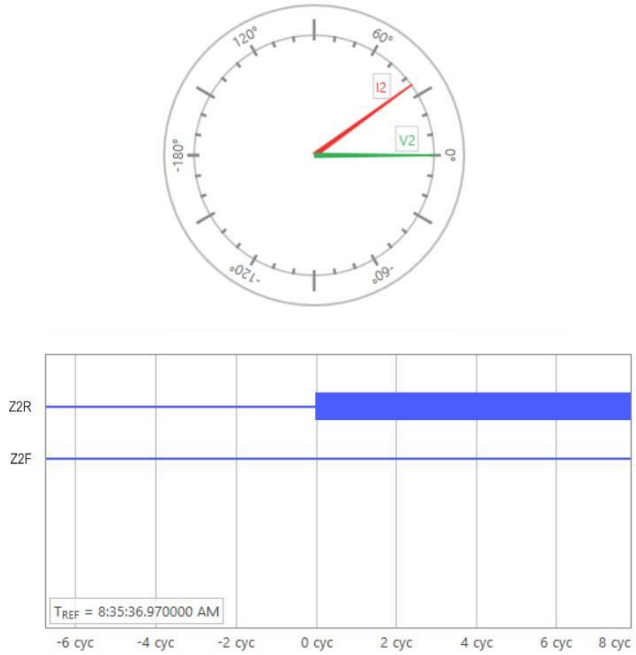

Figure 85. Negative-sequence current and voltage phasors and relay trip signal for 67Q element measured at POC bus in the solar PV system II under weak grid conditions following a single line-to-ground fault.

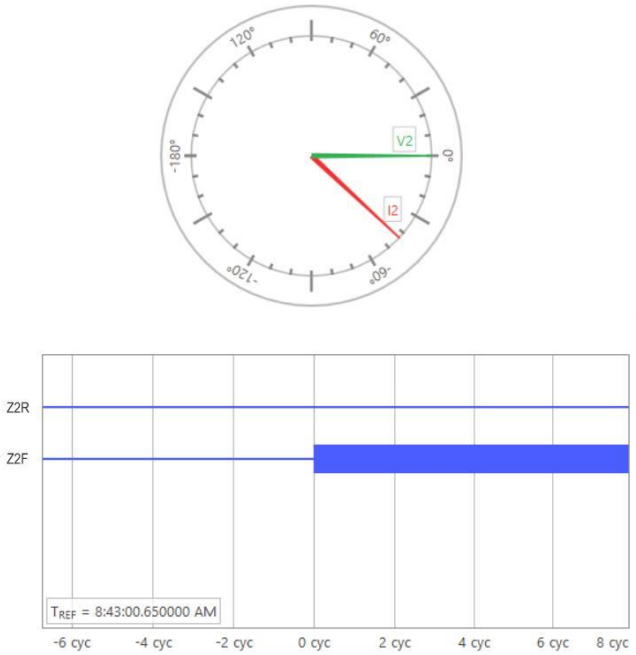

Figure 86. Negative-sequence current and voltage phasors and relay trip signal for 67Q element measured at POC bus in the solar PV system II under weak grid conditions following a double line-to-ground fault.

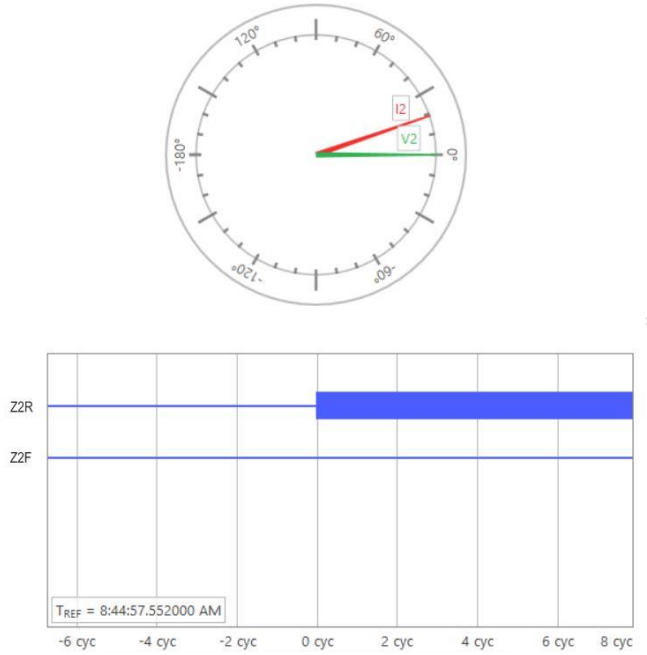

Figure 87. Negative-sequence current and voltage phasors and relay trip signal for 67Q element measured at POC bus in the solar PV system II under weak grid conditions following a line-to-line fault.

5.6. Summary

The chapter investigated the solar inverter dynamics with a focus on the negative-sequence current during the grid restoration period and their impact on protection schemes by using RTDS-based electromagnetic transient simulations with detailed inverter models that consider switching dynamics and inverter blocking and deblocking modes. It is found that solar inverters can act as negative-sequence sources after the inverter is deblocked to reinject energy into the power grid during the restoration period following a grid disturbance. The amplitude of the negative-sequence current can be affected by different operating conditions such as the number of inverters in service, grid strength, and grid fault types. Such negative-sequence responses can negatively impact on the performance of protection schemes based on negative-sequence components and potentially cause relay maloperations in the power grid during the restoration period. Thus, the grid protection will become less secure and reliable. A thorough review of negative sequence-based protection

schemes may be important for the relays with exposure to IBRs to account for their impact during the grid restoration period and ensure dependable and secure protection in the presence of IBRs.

6. CONCLUSIONS AND FUTURE WORK

Here, the conclusions for the dissertation will be drawn. First, we proposed the new method for evaluating the strength of power grids with the high penetration of IBRs taking into account the impact on grid strength from both the interactions between capacitors in the grid and the interactions among IBRs at different sites. This new method for evaluating grid strength will give grid operators an accurate estimate of how stable a specific point in the network is. Validation and efficacy of the proposed method was shown with numerical simulation case studies on the IEEE 39-bus system. It was shown that the ESDSCR accurately estimates grid strength in the presence of multiple renewable energy resources and multiple shunt capacitor banks when compared to the commonly used ESCR. The ESDSCR also doubles as a general form of the ESCR since if there is only one IBR and one shunt capacitor bank being studied, the ESDSCR has the same form as the ESCR.

Next, we investigated the impact of momentary cessation on sub-cycle transient characteristics using RTDS-based real-time electromagnetic transient simulations with detailed inverter models that consider switching dynamics and momentary cessation operation mode. It is found that undesired sub-cycle overvoltage and overcurrent are induced by momentary cessation. Moreover, the sub-cycle overvoltage and overcurrent become significant when increasing the integration of solar PV inverters into the system. Furthermore, it is found that the grid operating condition, which is normally considered as the initial or boundary condition of transient in the grid, needs to be further investigated, especially during the system recovery and inverter fault-ride through, where significant voltage sags or swells could be significant [13]. In addition, the overvoltage and overcurrent during the restoration stage of fault-ride through process can be

improved when considering the impact of the diversified recovery times for PV inverters to restart current injection.

Finally, we investigated the solar inverter dynamics with a focus on the negative-sequence current during the grid restoration period and their impact on protection schemes, such as overcurrent elements and directional elements, by using RTDS-based electromagnetic transient simulations with detailed inverter models that consider switching dynamics and inverter blocking and deblocking modes. It is found that solar inverters can act as negative-sequence sources after the inverter is deblocked to reinject energy into the power grid during the restoration period following a fault in the transmission network or generation. The amplitude of the negative-sequence current can be affected by different operating conditions such as the number of inverters in service, grid strength, and different fault types, including unbalanced and balanced fault types. Such negative-sequence responses can negatively impact on the performance of protection schemes based on negative-sequence components and potentially cause relay maloperations in the power grid during the restoration period. More specifically, the negative-sequence current during the grid restoration period surpassed the threshold set in the relay, therefore operating the relay. Also, the high negative-sequence current operated the directional element during the grid restoration period. Thus, the grid protection will become less secure and reliable.

For further research, the ESDSCR can be further explored using a larger power system network, such as using the IEEE 118-bus system or even using a real-world system that consists of 10,000 or more buses. With the real-world system, there are multiple inverter-based resources and multiple shunt capacitor banks that could be studied to further validate the strength assessment metric. Another possible avenue to explore is to study the effects of energy storage sites to see

how they affect system strength since battery storage is a prominent research topic and becoming more prevalent in a modern power grid.

Momentary cessation and solar PV inverter fault response can be used to study the impact of series compensation, since series compensation is known to have adverse effects on a power system network. The interaction between the controls of the inverter and the series compensation devices could potentially cause overvoltages and overcurrents, especially when the series compensation devices are close to the inverter-based resources. Another route for future research is to do a full hardware-in-loop design with a solar panel and an inverter to see how a real inverter system will interact with the power system network. These ideas for future research can be extended to study relay protection as well using other forms of relay protection such as fault type identification, impedance-based protection, differential protection, and others.

REFERENCES

[1] U. K. Nath and R. Sen, "A Comparative Review on Renewable Energy Application, Difficulties and Future Prospect," *2021 Innovations in Energy Management and Renewable Resources(52042)*, 2021, pp. 1-5, doi: 10.1109/IEMRE52042.2021.9386520.

[2] D. Rojas, M. Rivera and P. Wheeler, "Basic principles of solar energy," *2021 IEEE CHILEAN Conference on Electrical, Electronics Engineering, Information and Communication Technologies (CHILECON)*, 2021, pp. 1-6, doi: 10.1109/CHILECON54041.2021.9703066.

[3] S. U. Mahmud and Nahid-Al-Masood, "Performance Comparison between Synchronous Condenser and Static VAR Compensator to Improve System Strength in a Wind Dominated Power Grid," *2020 11th International Conference on Electrical and Computer Engineering (ICECE)*, 2020, pp. 411-414, doi: 10.1109/ICECE51571.2020.9393153.

[4] O. El Fadhel Loubaba Bekri and M. K. Fellah, "Placement of wind farms for enhancing voltage stability based on continuation power flow technique," *2015 3rd International Renewable and Sustainable Energy Conference (IRSEC)*, 2015, pp. 1-6, doi: 10.1109/IRSEC.2015.7455028.

[5] H. Yuan, X. Qin, W. Li, L. Su, G. Shen and H. Xin, "Small Signal Stability Analysis of Grid-Following Inverter-Based Resources in Weak Grids With SVGs Based on Grid Strength Assessment," *2021 IEEE 1st International Power Electronics and Application Symposium (PEAS)*, 2021, pp. 1-6, doi: 10.1109/PEAS53589.2021.9628724.

[6] Rajiv K. Varma, "MODELING AND CONTROL OF THREE-PHASE SMART PV INVERTERS," in *Smart Solar PV Inverters with Advanced Grid Support Functionalities* , IEEE, 2022, pp.73-106, doi: 10.1002/9781119214236.ch3.

[7] S. P. Hoffman, "NERC interconnected operations services policy developments related to frequency control," *IEEE Power Engineering Society. 1999 Winter Meeting (Cat. No.99CH36233)*, 1999, pp. 580-583 vol.1, doi: 10.1109/PESW.1999.747519.

[8] T. Hiyama, W. Zhang and S. Wakasugi, "Eigenvalue Based Wide Area Dynamic Stability Control of Electric Power Systems," *2007 International Conference on Intelligent Systems Applications to Power Systems*, 2007, pp. 1-6, doi: 10.1109/ISAP.2007.4441649.

[9] C. Li and R. Reinmuller, "Fault Responses of Inverter-based Renewable Generation: On Fault Ride-Through and Momentary Cessation," *2018 IEEE Power & Energy Society General Meeting (PESGM)*, 2018, pp. 1-5, doi: 10.1109/PESGM.2018.8585978.

[10] H. Vallecha and Shivam, "Power flow management and voltage control using solar and wind farm inverters in multi line system," *2015 Annual IEEE India Conference (INDICON)*, 2015, pp. 1-5, doi: 10.1109/INDICON.2015.7443511.

[11] T. Ye, L. Jin and R. Xue, "Influence of Grid-connection Photovoltaic on Power Quality and Relay Protection of Distribution Network," *2019 IEEE 8th International Conference on Advanced Power System Automation and Protection (APAP)*, 2019, pp. 940-944, doi: 10.1109/APAP47170.2019.9224711.

[12] B. Mahamedi and J. E. Fletcher, "The Equivalent Models of Grid-Forming Inverters in the Sequence Domain for the Steady-State Analysis of Power Systems," in *IEEE Transactions on Power Systems*, vol. 35, no. 4, pp. 2876-2887, July 2020, doi: 10.1109/TPWRS.2020.2968114.

[13] A. Saran, A. K. Srivastava and N. N. Schulz, "Modeling and simulation of shipboard power system protection schemes using coordination of overcurrent relay," *2009 IEEE Electric Ship Technologies Symposium*, 2009, pp. 282-289, doi: 10.1109/ESTS.2009.4906527.

[14] NERC Integrating inverter-based resources into low short circuit strength systems. December 2017. Available: https://www.nerc.com/comm/PC_Reliability_Guidelines_DL/Item_4a._Integrating%20_Inverter-Based_Resources_into_Low_Short_Circuit_Strength_Systems_-_2017-11-08-FINAL.pdf

[15] NERC essential reliability services task force: measures framework report. November 2015. Available: http://www.nerc.com/comm/Other/essntlrlbltysrvcstskfrcDL/ERSTF%20Framework%20Report%20-%20Final.pdf

[16] IEEE guide for planning dc links terminating at ac locations having low short-circuit capacities, IEEE Standard 1204-1997, 1997.

[17] Cigré Brochure 370. “Integration of large scale wind generation using hvdc and power electronics". WG-B4.39. ISBN: 978-2-85873-057-5., 2009.

[18] Y. Zhou, D. D. Nguyen, P. C. Kjaer and S. Saylors, “Connecting wind power plant with weak grid – challenges and solutions”, *IEEE Power and Energy Society General Meeting*, July 2013, pp. 1-5.

[19] Nicholas W. Miller, Bruno Leonardi, Robert D’Aquila, and Kara Clark. Western wind and solar integration study phase 3a: low levels of synchronous generation. National Renewable Energy Laboratory. Available: https://www.nrel.gov/docs/fy16osti/64822.pdf.

[20] Y. Zhu, and D Brown, “Prepare to meet the challenges in regional transmission planning and development,” *IEEE Power and Energy Society General Meeting*, July 2015, pp. 1-5

[21] Y. Zhang, S. H. Huang, J. Schmall, J. Conto, J. Billo and E. Rehman, “Evaluating system strength for large-scale wind plant integration”, *IEEE Power and Energy Society General Meeting*, July 2014, pp. 1-5.

[22] (2014, Oct). Minnesota renewable energy integration and transmission study final report. GE Energy Consulting. Available: http://www.minnelectrans.com/documents/mrits-report.pdf.

[23] D. Wu, G. Li, M. Javadi, A. Malyscheff, Member, M. Hong, and J. Jiang, “Assessing impact of renewable energy integration on system strength using site-dependent short circuit ratio,” *IEEE Transaction on Sustainable Energy*, vol. 9, no. 3, pp. 1072-1080, 2018.

[24] “On Voltage and power stability in ac/dc systems,” CIGRÉ WG14.05 Guide, Final Draft, Aug. 2002.

[25] M. A Pai, *Energy function analysis for power system stability*. New York, NY: Springer, 1989.

[26] Standard for Inverters, Converters, Controllers and Interconnection System Equipment for Use with Distributed Energy Resources, UL 1741-SA, June 2016.

[27] Generator Frequency and Voltage Protective Relay Settings, NERC PRC-024-2, NERC, Atlanta, GA, May 2015.

[28] North American Electric Reliability Corporation, “1,200 MW Fault Induced Solar Photovoltaic Resource Interruption Disturbance Report: Southern California 8/16/2016 Event,” NERC, Atlanta, GA, June 2017.

[29] North American Electric Reliability Corporation, “900 MW Fault Induced Solar Photovoltaic Resource Interruption Disturbance Report: Southern California Event: October 9, 2017 Joint NERC and WECC Staff Report,” NERC, Atlanta, GA, Feb. 2018.

[30] North American Electric Reliability Corporation, “April and May 2018 Fault Induced Solar Photovoltaic Resource Interruption Disturbances Report: Southern California Events: April 20, 2018 and May 11, 2018, Joint NERC and WECC Staff Report,” NERC, Atlanta, GA, Jan. 2019.

[31] “IEEE 1547-2018: IEEE Standard for Interconnection and Interoperability of Distributed Energy Resources with Associated Electric Power Systems Interfaces.” IEEE, Apr. 2018.

[32] “Inverter-Based Resource Disturbance Analysis – Key Findings and Recommendations,” North American Electric Reliability Corporation, Informational Webinar, Feb. 2018.

[33] North American Electric Reliability Corporation, “Reliability Guideline: BPS-Connected Inverter-Based Resource Performance,” NERC, Atlanta, GA, Sep. 2018.

[34] H. Shin, B. Lee, and K. Iba, “Power system regional dependency of distributed energy resources: Utilizing the momentary cessation capability,” IFAC-PapersOnLine, vol. 52, no. 4, pp. 1–5, 2019.

[35] RTDS Technologies Inc. https://www.rtds.com.

[36] "RSCAD - Power System Simulation Software" in RTDS Technologies Inc., 2018.

[37] R. Guttromson, M. Behnke “Momentary Cessation: Improving Dynamic Performance and Modeling of Utility-Scale Inverter Based Resources During Grid Disturbances,” Sandia National Laboratories, Albuquerque, New Mexico, Jan. 2020.

[38] H. G. Sarmiento, E. Estrada, “A Voltage Sag Study in An Industry with Adjustable-Speed Drives", IEEE Industry Applications Magazine, vol.1, no.1, pp.16-19, 1996.

[39] IEEE PES Industry Technical Support Task Force, “Impact of inverter based generation on bulk power system dynamics and short-circuit performance,” Institute of Electrical and Electronics Engineers, Piscataway, NJ, USA, IEEE PES Tech. Rep. Number: PES-TR68, 2018.

[40] Standard for Inverters, Converters, Controllers and Interconnection System Equipment for Use with Distributed Energy Resources, UL 1741-SA, June 2016.

[41] M. Behnke et al., “Impact of inverter-based resource negative-sequence current injection on transmission system protection,” Sandia National Laboratories, Albuquerque, NW, USA, Jan. 2020.

[42] IEEE PES Industry Technical Support Task Force, “Impact of inverter based generation on bulk power system dynamics and short-circuit performance,” Institute of Electrical and Electronics Engineers, Piscataway, NJ, USA, IEEE PES Tech. Rep. Number: PES-TR68, 2018.

[43] G. Kou, L. Chen, P. VanSant, F. Velez-Cedeno, and Y. Liu, “Fault characteristics of distributed solar generation,” IEEE Trans. Power Del., vol. 35, no. 2, pp. 1062–1064, Apr. 2020.

[44] I. Erlich, T. Neumann, F. Shewarega, P. Schegner, and J. Meyer, “Wind turbine negative sequence current control and its effect on power system protection,” in Proc. IEEE Power Energy Soc. Gen. Meeting, Jul. 2013, pp. 1–5.

[45] Impact of Renewables on System Protection: Wind/PV Short-Circuit Phasor Model Library and Guidelines for System Protection Studies. Palo Alto, CA: EPRI, 2016.

[46] A.Haddadi, I.Kocar, and E. Farantatos, “Impact of inverter-based resources on protection schemes based on negative sequence components,” Electric Power Research Institute,

Palo Alto, CA, USA, Jul. 2019. [Online] Available: https://www.epri.com/research/products/000000003002016197

[47] M. Behnke et al., “Impact of inverter-based resource negative-sequence current injection on transmission system protection,” Sandia National Laboratories, Albuquerque, NW, USA, Jan. 2020. [Online] Available: https://www.osti.gov/servlets/purl/1595917

[48] 1200 MW Fault Induced Solar Photovoltaic Resource Interruption Disturbance Report; North American Electric Reliability Corpo-ration: Atlanta, GA, USA, 2016. 2.

[49] 900 MW Fault Induced Solar Photovoltaic Resource Interruption Disturbance Report; North American Electric Reliability Corpora-tion: Atlanta, GA, USA, 2018.

[50] April and May 2018 Fault Induced Solar Photovoltaic Resource Interruption Disturbances Report: Southern California Events: 20 April 2018 and 11 May 2018; North American Electric Reliability Corporation: Atlanta, GA, USA, 2019.

[51] San Fernando Disturbance Southern California Event: 7 July 2020 Joint NERC and WECC Staff Report; Atlanta, GA, USA, 2020.

[52] Kang, S.; Shin, H.; Jang, G.; Lee, B. Impact Analysis of Recovery Ramp Rate After Momentary Cessation in Inverter-based Distributed Generators on Power System Transient Stability. IET Gener. Transm. Distrib. 2020, 15, 24–33.

[53] Pierre, B.J.; Elkhatib, M.E.; Hoke, A. Photovoltaic Inverter Momentary Cessation: Recovery Process is Key. In Proceedings of the 2019 IEEE 46th Photovoltaic Specialists Conference (PVSC), Chicago, IL, USA, 16–21 June 2019.

[54] Choi, N.; Park, B.; Cho, H.; Lee, B. Impact of Momentary Cessation Voltage Level in Inverter-Based Resources on Increasing the Short Circuit Current. Sustainability 2019, 11, 1153.

[55] Zhu, S.; Piper, D.; Ramasubramanian, D.; Quint, R.; Isaacs, A.; Bauer, R. Modeling Inverter-Based Resources in Stability Studies. In 2018 IEEE Power & Energy Society General Meeting (PESGM); Portland, OR, USA, 2018.

[56] Shin, H.; Jung, J.; Lee, B. Determining the Capacity Limit of Inverter-Based Distributed Generators in High-Generation Areas Considering Transient and Frequency Stability. IEEE Access 2020, 8, 34071–34079.

[57] Mather, B.; Ding, F. Distribution-connected PV's response to voltage sags at transmission-scale. In Proceedings of the 2016 IEEE 43rd Photovoltaic Specialists Conference (PVSC), Portland, OR, USA, 5–10 June 2016; pp. 2030–2035.

[58] Mather, B.; Aworo, O.; Bravo, R.; Piper, P.E.D. Laboratory Testing of a Utility-Scale PV Inverter's Operational Response to Grid Disturbances. In Proceedings of the 2018 IEEE Power & Energy Society General Meeting (PESGM), Portland, OR, USA, 5–10 August 2018; pp. 1–5.

[59] Kenyon, R.W.; Mather, B.; Hodge, B.-M. Coupled Transmission and Distribution Simulations to Assess Distributed Genera-tion Response to Power System Faults. Electr. Power Syst. Res. 2020, 189, 106746.

[60] Shin, H.; Jung, J.; Oh, S.; Hur, K.; Iba, K.; Lee, B. Evaluating the Influence of Momentary Cessation Mode in Inverter-Based Distributed Generators on Power System Transient Stability. IEEE Trans. Power Syst. 2020, 35, 1618–1626.

[61] Li, C.; Reinmuller, R. Fault Responses of Inverter-based Renewable Generation: On Fault Ride-Through and Momentary Ces-sation. In 2018 IEEE Power & Energy Society General Meeting (PESGM); Portland, OR, USA, 2018.

[62] Pierre, B.J.; Elkhatib, M.E.; Hoke, A. PV Inverter Fault Response Including Momentary Cessation, Frequency-Watt, and Vir-tual Inertia. In 2018 IEEE 7th World Conference on Photovoltaic Energy Conversion (WCPEC) (A Joint Conference of 45th IEEE PVSC, 28th PVSEC & 34th EU PVSEC); Waikoloa, HI, USA, 2018.

[63] RTDS Technologies Inc. https://www.rtds.com

[64] North American Electric Reliability Corporation, “900 MW Fault Induced Solar Photovoltaic Resource Interruption Disturbance Report: Southern California Event: October 9, 2017 Joint NERC and WECC Staff Report,” NERC, Atlanta, GA, Feb. 2018.

[65] North American Electric Reliability Corporation, “April and May 2018 Fault Induced Solar Photovoltaic Resource Interruption Disturbances Report: Southern California Events: April 20, 2018 and May 11, 2018, Joint NERC and WECC Staff Report,” NERC, Atlanta, GA, Jan. 2019.

[66] "RSCAD - Power System Simulation Software" in RTDS Technologies Inc., 2018.

[67] A. A. Elserougi, A. M. Massoud, A. S. Abdel-Khalik and S. Ahmed, "Bidirectional Buck-Boost Inverter-Based HVDC Transmission System With AC-Side Contribution Blocking Capability During DC-Side Faults," in IEEE Transactions on Power Delivery, vol. 29, no. 3, pp. 1249-1261, June 2014, doi: 10.1109/TPWRD.2014.2308274.

[68] F. Calero, Rebirth of Negative-Sequence Quantities in Protective Relaying With Microprocessor-Based Relays. Pitampura, Delhi: Schweitzer Eng. Labs. Inc., 2003.

[69] J. Horak, “Directional overcurrent relaying (67) concepts,” in Proc. 59th Annu. Conf. Protective Relay Engineers, College Station, TX, 2006, pp. 164–176.

[70] Y. Ohura, T. Matsuda, M. Suzuki, F. Andow, Y. Kurosawa, and A. Takeuchi, “A digital distance relay using negative sequence current,” IEEE Trans. Power Del., vol. 5, no. 1, pp. 79–84, Jan. 1990.

APPENDIX A. RELAY SETTINGS

Table A1 presents the settings used for both the 50Q relay element and the 67Q relay element for Chapter 5.

Table A1. Relay Settings.

ANSI Element	Setting	Value
50Q	50Q1P – Instantaneous Negative-sequence pickup current I_{2pkp}	80 A
	Z2F – Forward negative-sequence impedance threshold	38 Ω
	Z2R – Reverse negative-sequence impedance threshold	38.1 Ω
67Q	50QF – Forward negative-sequence current threshold	0.5 A
	50QR – Reverse negative-sequence current threshold	0.25 A
	a2 – Positive-sequence current restraint factor	0.07

APPENDIX B. LIST OF PUBLICATIONS

1. A. Ekic, A. Fischer, A. Eisenbeisz, G. Lind, A. M. Aldaoudeyeh, and D. Wu, "*Impact Analysis of Power Network Structure on Grid Strength*", IEEE NAPS 2018, URL: https://ieeexplore.ieee.org/document/8600573

2. A. Ekic, B. Strombeck, D. Wu, and J. Guomin, "*Assessment of Grid Strength Considering Interactions between Inverter-based Resources and Shunt Capacitors*", IEEE PES GM 2020, URL: https://ieeexplore.ieee.org/document/9281633

3. L. Chen, A. Ekic, and D. Wu, "*Multi-Objective Grid Planning for Renewable Energy Integration*", IEEE PES GM 2020, URL: https://ieeexplore.ieee.org/document/9282052

4. A. Ekic, M. Maharjan, B. Strombeck, and D. Wu, "*Impact of Inverter Modeling on Sub-cycle Dynamics in Grid-Connected Solar PV Systems*", IEEE PVSC 2021, URL: https://ieeexplore.ieee.org/document/9519062

5. A. Ekic, M. Maharjan, B. Strombeck, and D. Wu, "*Impact of Momentary Cessation on Sub-cycle Dynamics in Grid-Connected Solar PV Systems*", IEEE ISGT 2021, URL: https://ieeexplore.ieee.org/document/9372156

6. A. Ekic, B. Walberg, M. Maharjan, B. Strombeck, J. Guomin, and D. Wu, "*Impact of Grid Strength on Sub-cycle Dynamics in Solar PV Systems*", IEEE PES GM 2021, URL: https://ieeexplore.ieee.org/document/9638248

7. M. Maharjan, A. Ekic, B. Strombeck, and D. Wu, "*An RTDS-Based Testbed for Investigating the Impacts of Transmission-Level Disturbances on Solar PV Operation*", MDPI Energies Journal 2021, URL: https://www.mdpi.com/1996-1073/14/13/3867

8. A. Ekic, D. Wu, and J. N. Jiang, "*Impact of Solar Inverter Dynamics during Grid Restoration Period on Protection Schemes Based on Negative-Sequence Components*", MDPI Energies Journal 2022, URL: https://www.mdpi.com/1996-1073/15/12/4360

9. A. Ekic, M. Maharjan, D. Wu, M. Boese, and R. S. Kandezy, "*Impact of Inverter Dynamics during System Restoration Period on Protection Schemes in Grid-Connected Solar PV Systems*", IEEE PES GM 2022

10. A. Ekic, D. Wu, and Y. Huang, "*A Review on Cascading Failure Analysis for Integrated Power and Gas Systems*", IEEE ENERGYCON 2022

11. Y. Zhou, G. Wang, A. Ekic, W. Huang, C. Wu, D. Zhang, D. Wu, and H. Xin, "*Small-signal Stability Analysis of Power Systems under Uncertain Renewable Generation*", IEEE PES GM 2022